Selective, Cofactor-mediated Catalytic Oxidation of Alkanethiols in a Self-Assembled Cage Host

Bryce da Camara, Philip C. Dietz, Kevin R. Chalek, Leonard J. Mueller and Richard J. Hooley

Department of Chemistry, University of California, Riverside, CA 92521.

E-mail: richard.hooley@ucr.edu

Electronic Supplementary Information

Table of Contents

I. General Information

Cages **1**,[1a] **2**[1b] and **3**[1c] were synthesized according to literature procedures.[1] See those publications for full characterization. ^{1}H, and ^{13}C spectra were recorded on Bruker Avance NEO 400 MHz or Bruker Avance 600 MHz NMR spectrometer. The spectrometers were automatically tuned and matched to the correct operating frequencies. Proton (^{1}H) and carbon (^{13}C) chemical shifts are reported in parts per million (δ) with respect to tetramethylsilane (TMS, δ=0), and referenced internally with respect to the protio solvent impurity for CD_3CN (^{1}H: 1.94 ppm, ^{13}C: 118.3 ppm). Deuterated NMR solvents were obtained from Cambridge Isotope Laboratories, Inc., Andover, MA, and used without further purification. Spectra were digitally processed (phase and baseline corrections, integration, peak analysis) using Bruker Topspin 1.3 and MestreNova. All other materials were obtained from Combiblocks (San Diego, CA), Aldrich Chemical Company (St. Louis, MO), or Fisher Scientific (Fairlawn, NJ), and were used as received. Solvents were dried through a commercial solvent purification system (Pure Process Technologies, Inc.). UV/Vis spectroscopy was performed on a Cary 60 Photospectrometer using the Varian Scans program to collect data. GC analysis was performed on a Hewlett-Packard (now Agilent) 5890 GC, fitted with a J&W DB-5 column, 30 m x 0.32 mm Id, the instrument has a flame ionization detector (FID), and the injector and detector temperature was 250 °C and was run in split mode. Mass spectrometric samples were infused into an Orbitrap Velos Pro mass spectrometer with the standard HESI source at a flow rate of 3 μL/min. The spray voltage was 3 kV, capillary temperature was set to 170 °C and an S-lens RF level of 45 % was applied. Full FTMS were acquired with a resolution of r = 30,000, and ambient ions were used as internal lock mass calibrants. CID spectra were collected in ZoomScan mode where the isolation window = 5 m/z, normalized collision energy (nCE) = 30 and activation time = 30 ms. MS data was analyzed using Thermo XCalibur. Predicted isotope patterns were prepared using ChemCalc.

General procedure for oxidation reactions. Initially a 400 μL solution of thiol (1 mol.-eq., 7.3 μmol, 0.18 M solution in CD_3CN) and 1,4-dioxane as the internal standard (0.5 mol.-eq., 3.65 μmol, of 0.09 M solution in CD_3CN) was added to an NMR tube followed by 5 mol % cage **1** (0.36 μmol, 2 mg). The NMR tube was capped and quickly shaken to dissolve all solids. An initial ^{1}H NMR spectrum of the reaction mixture was obtained to verify the stoichiometry of the sample. The sample was then heated at 50 °C in a sand bath or left to sit in a test at room temperature while the reaction progress monitored over time. The percent conversion values were obtained via integration of the product and substrate peaks against the internal standard.

General procedure for control experiments. <u>$Fe(NTf_2)_2$ doping studies</u>**:** A volume of 300 μL of a solution containing thiol (1 mol.-eq., 7.3 μmol, 0.024 M solution in CD_3CN) and 1,4-dioxane as the

internal standard (0.5 mol.-eq., 3.65 μmol, of 0.012 M solution in CD_3CN) was added to an NMR tube. The concentration of iron in the reaction solution was adjusted via the addition of aliquots from a $Fe(NTf_2)_2$ stock solution (0.1-0.5 mol.-eq., 0.7-3.7 μmol, of 0.14 mM solution in CD_3CN). 5 mol % **1** (0.36 μmol, 2 mg) was then added before finally adding CD_3CN so that the final reaction volume was 400 μL. The NMR tube was then capped and shaken to ensure proper solvation of **1**. An initial ^1H NMR spectrum of the reaction mixture was obtained to verify the stoichiometry of the sample. The sample was then heated at 50 °C in a sand bath and the reaction progress monitored over time. Supramolecular cage and assembly studies: Initially a 400 μL solution of thiol (1 mol.-eq., 7.3 μmol, 0.18 M solution in CD_3CN) and 1,4-dioxane as the internal standard (0.5 mol.-eq., 3.65 μmol, of 0.09 M solution in CD_3CN) was added to an NMR tube followed by the addition of 5 mol % cage **1** (0.36 μmol, 2 mg), **2** (0.36 μmol, 1.8 mg), or **3** (0.72 μmol, 1.8 mg). The NMR tube was then capped and shaken to ensure proper solvation of supramolecular cages or assembly. An initial ^1H NMR spectrum of the reaction mixture was obtained to verify the stoichiometry of the sample. The sample was then heated at 80 °C in a sand bath and the reaction progress monitored over time.

General procedure for size selective studies and gas chromatography analysis. Initially 2 400 μL solutions of thiol A and B (1 mol.-eq., 7.3 μmol, 0.018 M solution in CD_3CN) and 1,4-dioxane as the internal standard (0.5 mol.-eq., 3.65 μmol, of 0.009 M solution in CD_3CN) were added to **separate** NMR tubes. An initial ^1H NMR spectrum of the reaction mixture was obtained to verify the stoichiometry of the sample. Following the NMR samples were combined into a new NMR tube followed by the addition of 5 mol % cage **1** (0.72 μmol, 4 mg). The NMR tube was capped and quickly shaken to dissolve all solids. Another ^1H NMR spectrum of the reaction mixture was obtained to ensure all reaction components were present. The sample was then left to sit in a test tube at room temperature while the reaction progress was monitored over time. Once ~20% conversion had been achieved after 7 days the contents were flushed through a silica plug with ~ 2 mL of ether, in addition to 450 μL solution of dodecane (0.6 mol.-eq., 4.05 μmol, 9 mM solution in diethyl ether) as an internal standard for GC analysis. The GC was then programmed with an initial temperature of 70 °C with a ramp rate of 10 °C per minute to 120 °C followed by a ramp rate of 20 °C per minute to 280 °C. The run was held at 280 °C until all reaction components had appeared on the chromatogram. The percent conversion values were obtained via integration of the product and substrate peaks against the internal standard on the GC chromatogram.

II. NMR Data for Oxidation Reactions

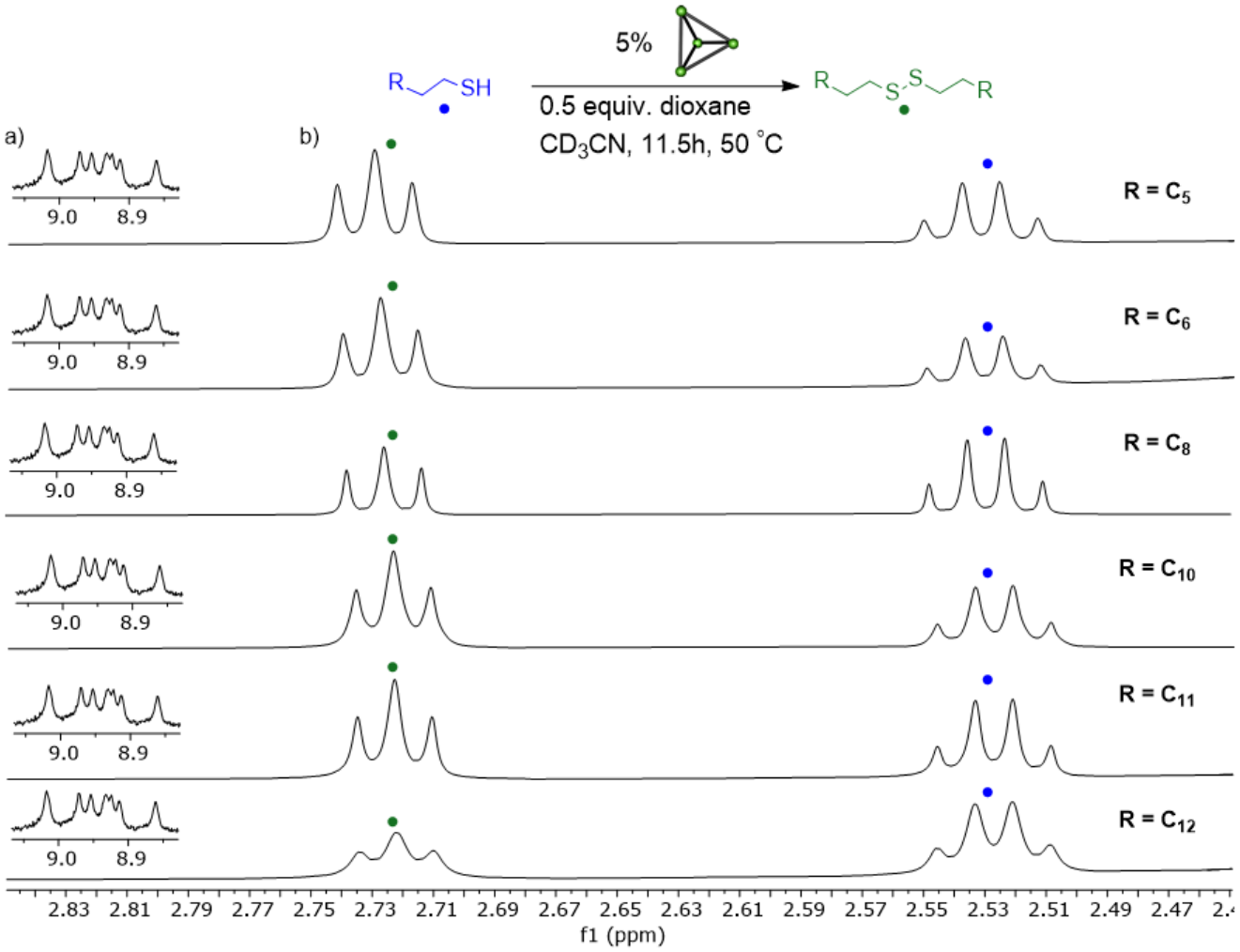

Figure S-1. ^{1}H NMR spectra of the oxidative dimerization of various thiols with varying length in the presence of 5 mol % cage **1** showing: a) cage stability for the oxidation reaction (9.1-8.8 ppm) b) product formation (2.85-2.45 ppm). [**C$_x$-SH**] = 18.2 mM, [**1**] = 0.9 mM, in CD_3CN. Reactions were performed at 50 °C in 400 µL CD_3CN and monitored over time (600 MHz, 298K, CD_3CN).

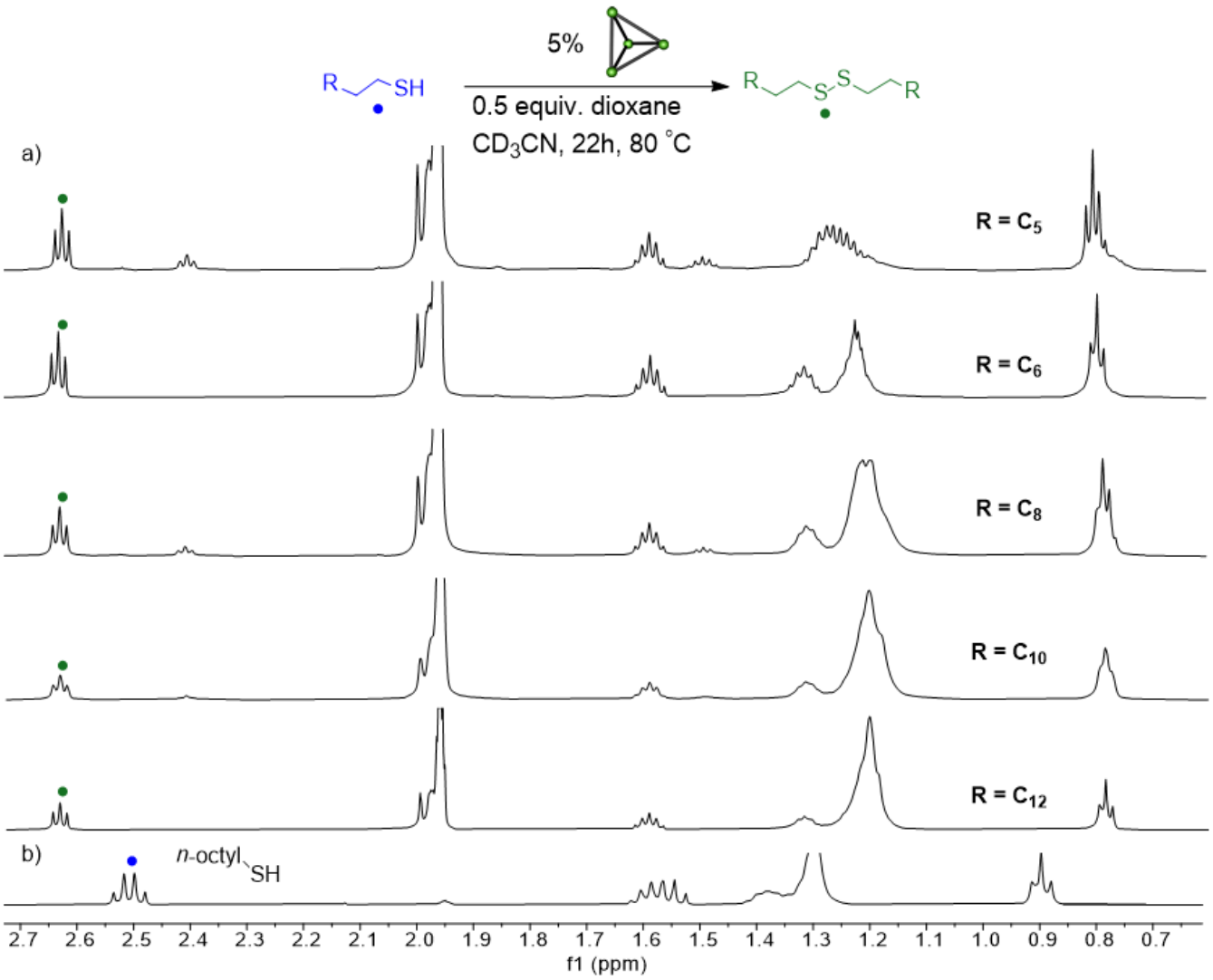

Figure S-2. ^{1}H NMR spectra of the oxidative dimerization of various thiols with varying length in the presence of 5 mol % cage **1** showing: a) product formation (2.80-0.6 ppm), b) **C_8-SH** for comparison (2.80-0.6 ppm). [**C_x-SH**] = 18.2 mM, [**1**] = 0.9 mM, in CD_3CN. Reactions were performed at 80 °C in 400 µL CD_3CN and monitored over time (600 MHz, 298K, CD_3CN).

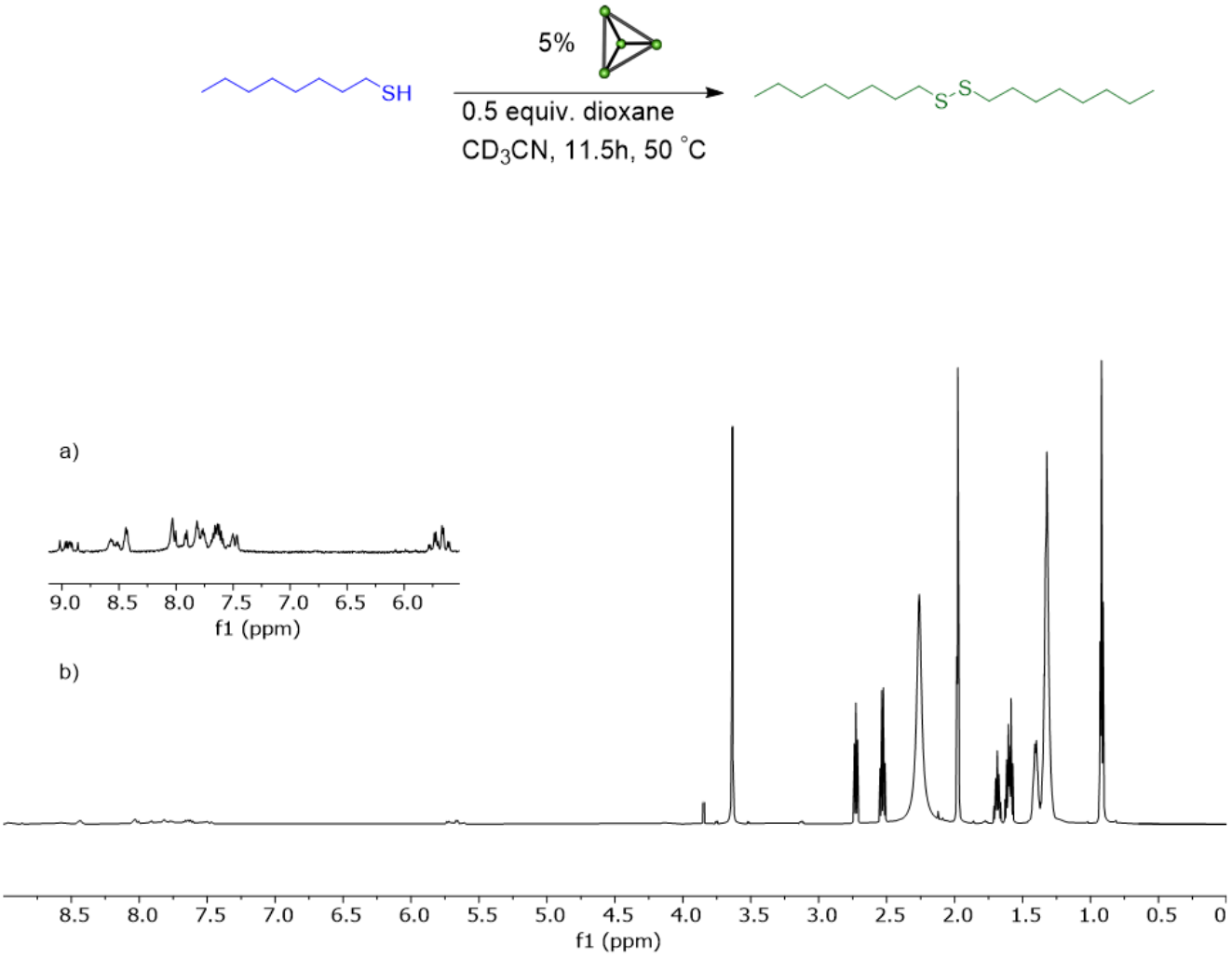

Figure S-3. ^{1}H NMR spectrum of the oxidative dimerization of **C_8-SH** in the presence of 5 mol % cage **1** showing: a) presence and stability of cage (9.1-5.5 ppm) b) presence of reactant and product (9.0-0.0 ppm). [**C_8-SH**] = 18.2 mM, [**1**] = 0.9 mM, in CD_3CN. Reaction was performed at 50 °C in 400 µL CD_3CN and monitored over time (600 MHz, 298K, CD_3CN).

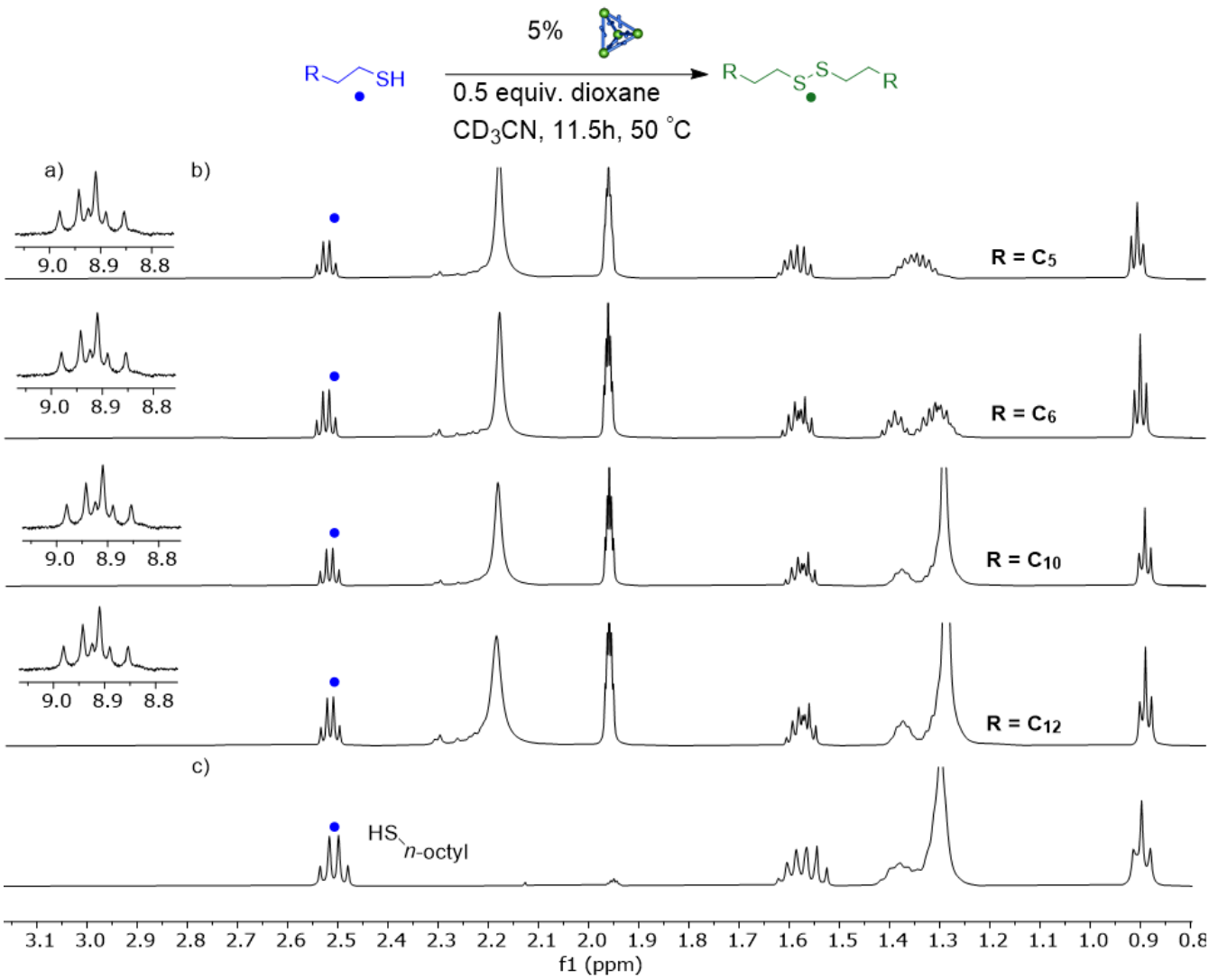

Figure S-4. ^{1}H NMR spectra of the various thiols with varying length in the presence of 5 mol % cage **2** showing: a) presence and stability of cage (9.1-8.7 ppm) b) lack of product formation (2.80-0.6 ppm), c) **C_8-SH** for comparison. [**C_x-SH**] = 18.2 mM, [**2**] = 0.9 mM, in CD_3CN. Reactions were performed at 50 °C in 400 µL CD_3CN and monitored over time (600 MHz, 298K, CD_3CN).

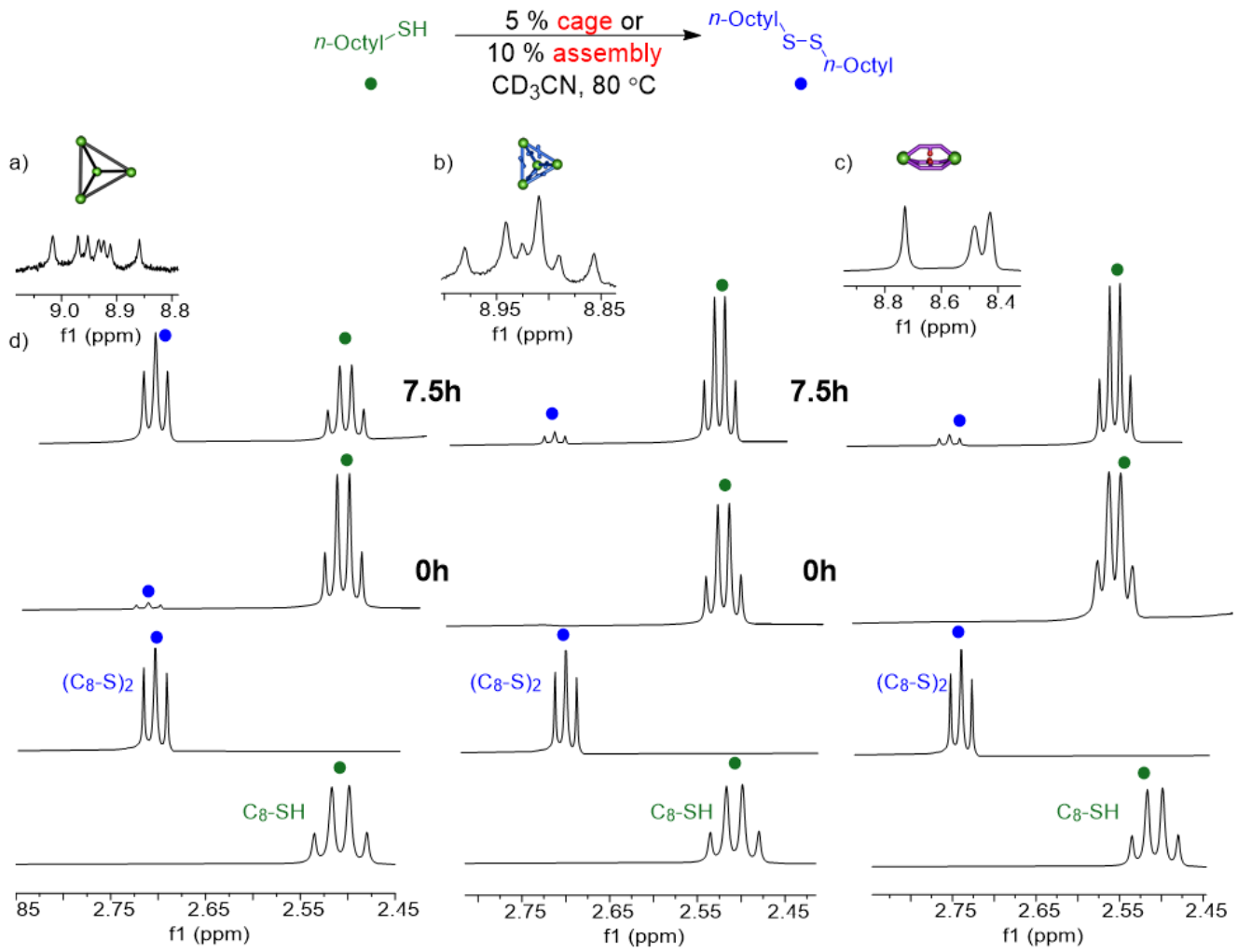

Figure S-5. ^{1}H NMR spectra of the oxidative dimerization of **C_8-SH** in the presence of 5 mol % cage **1,** 5 mol % cage **2**, and 10 mol % assembly **3** showing: a), b), c) cage and assembly stability for the oxidation reaction (9.1-8.7 ppm) d) difference in relative rate of product formation for **1**, **2**, and **3** (2.85-2.45 ppm). [**C_8-SH**] = 18.2 mM, [**1**] = 0.9 mM, [**2**] = 0.9 mM, and [**3**] = 1.8 mM in CD_3CN. Reactions were performed at 80 °C in 400 µL CD_3CN and monitored over time (600 MHz, 298K, CD_3CN).

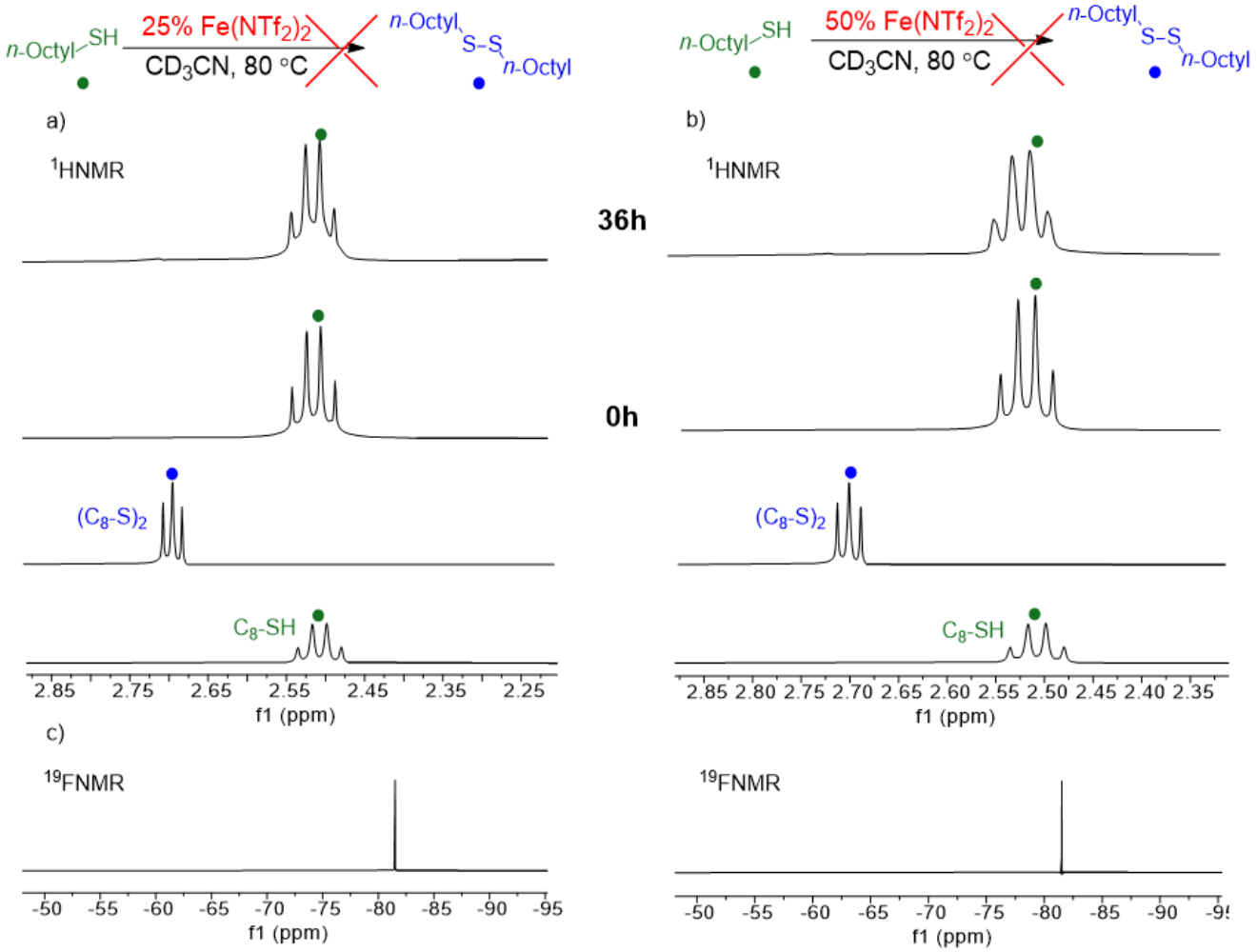

Figure *S-6*. ^{1}H NMR spectra of **C_8-SH** in the presence of 25 and 50 mol % $Fe(NTf_2)_2$ showing: a), b) lack of product formation using 2 different concentrations of $Fe(NTf_2)_2$ (2.85-2.20 ppm), c) ^{19}F spectra confirmation that iron species are in solution (-55 – -95 ppm) in CD_3CN. [$Fe(NTf_2)_2$] = 4.6 mM and 9.1 mM, and [**C_8-SH**] = 18.2 mM. Reactions were performed at 80 °C in 400 µL CD_3CN and monitored over time (600 MHz, 298K, CD_3CN).

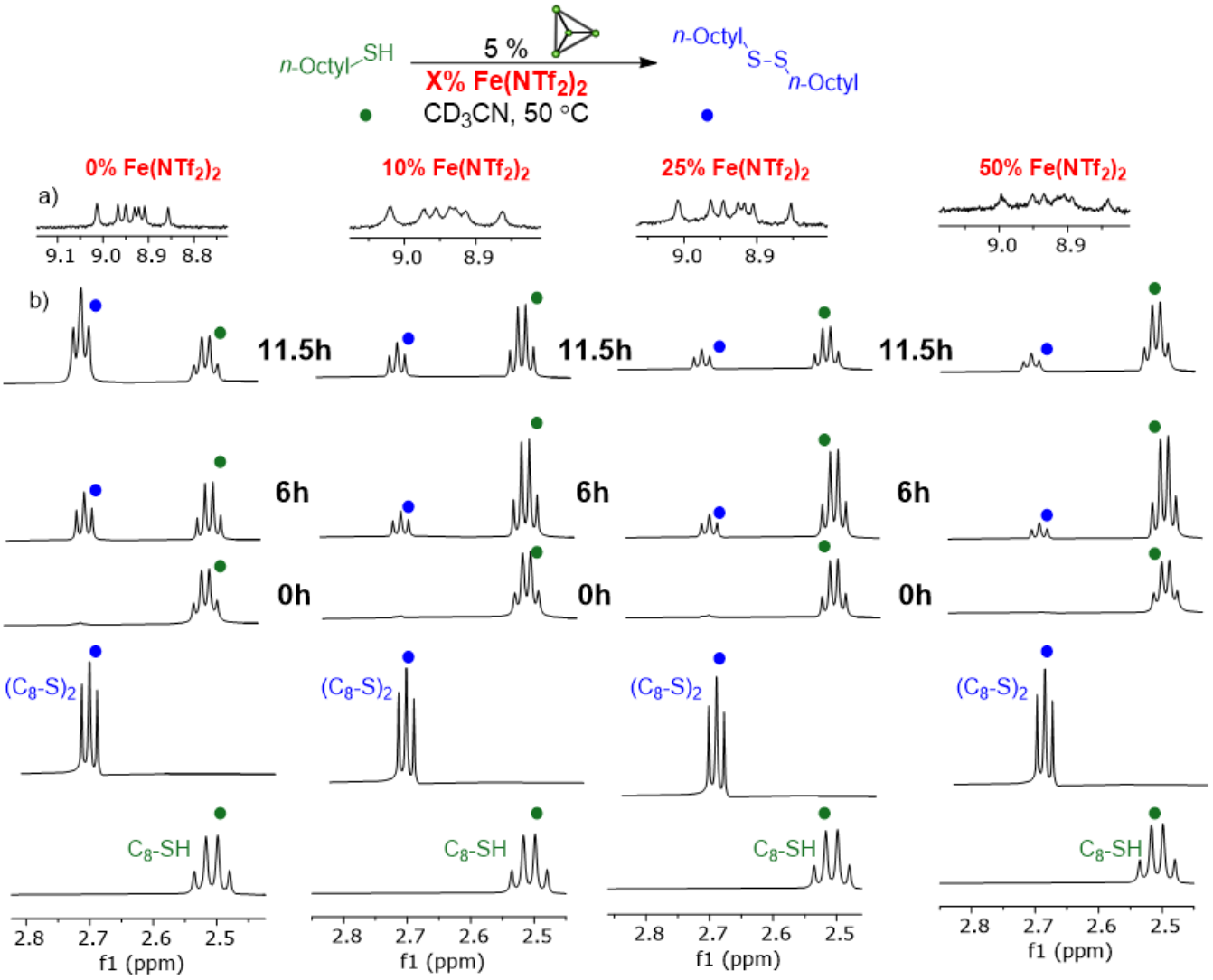

Figure S-7. ^{1}H NMR spectra of the oxidation of **C$_8$-SH** with varying concentrations of $Fe(NTf_2)_2$ showing: a) cage stability at varying concentrations of $Fe(NTf_2)_2$, b) relative rate of product formation using varying concentrations of $Fe(NTf_2)_2$ (2.85-2.45 ppm). [**C$_8$-SH**] = 18.2 mM, [**1**] = 0.9 mM, [$Fe(NTf_2)_2$] = 0, 1.8, 4.6, 9.1 mM. Reactions were performed at 80 °C in 400 µL CD_3CN and monitored over time (600 MHz, 298K, CD_3CN).

III. GC Data for Size Selective Studies

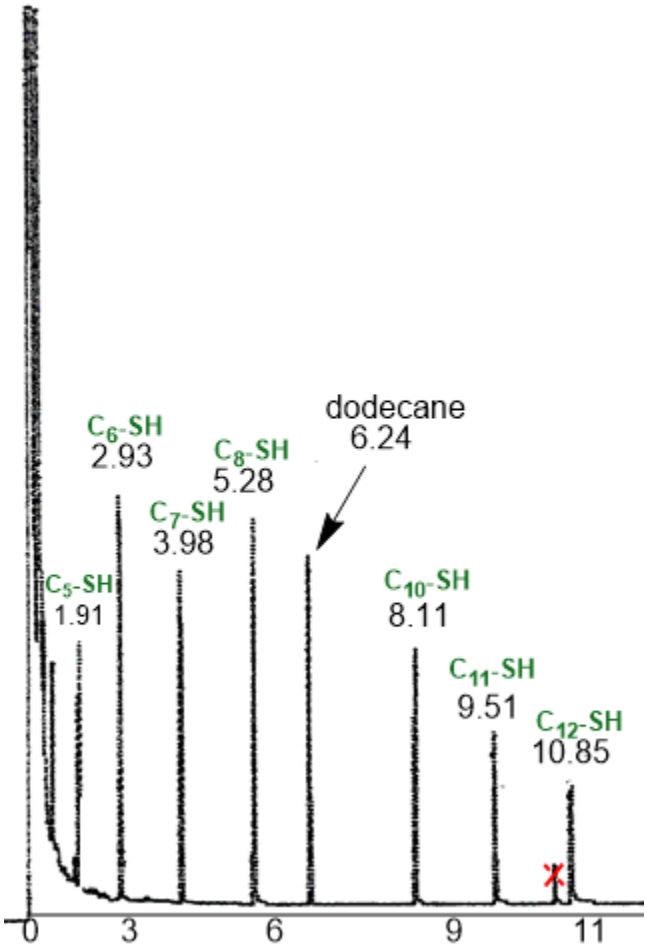

Figure S-8. GC calibration displaying relative retention times of alkane thiols with varying lengths and dodecane.

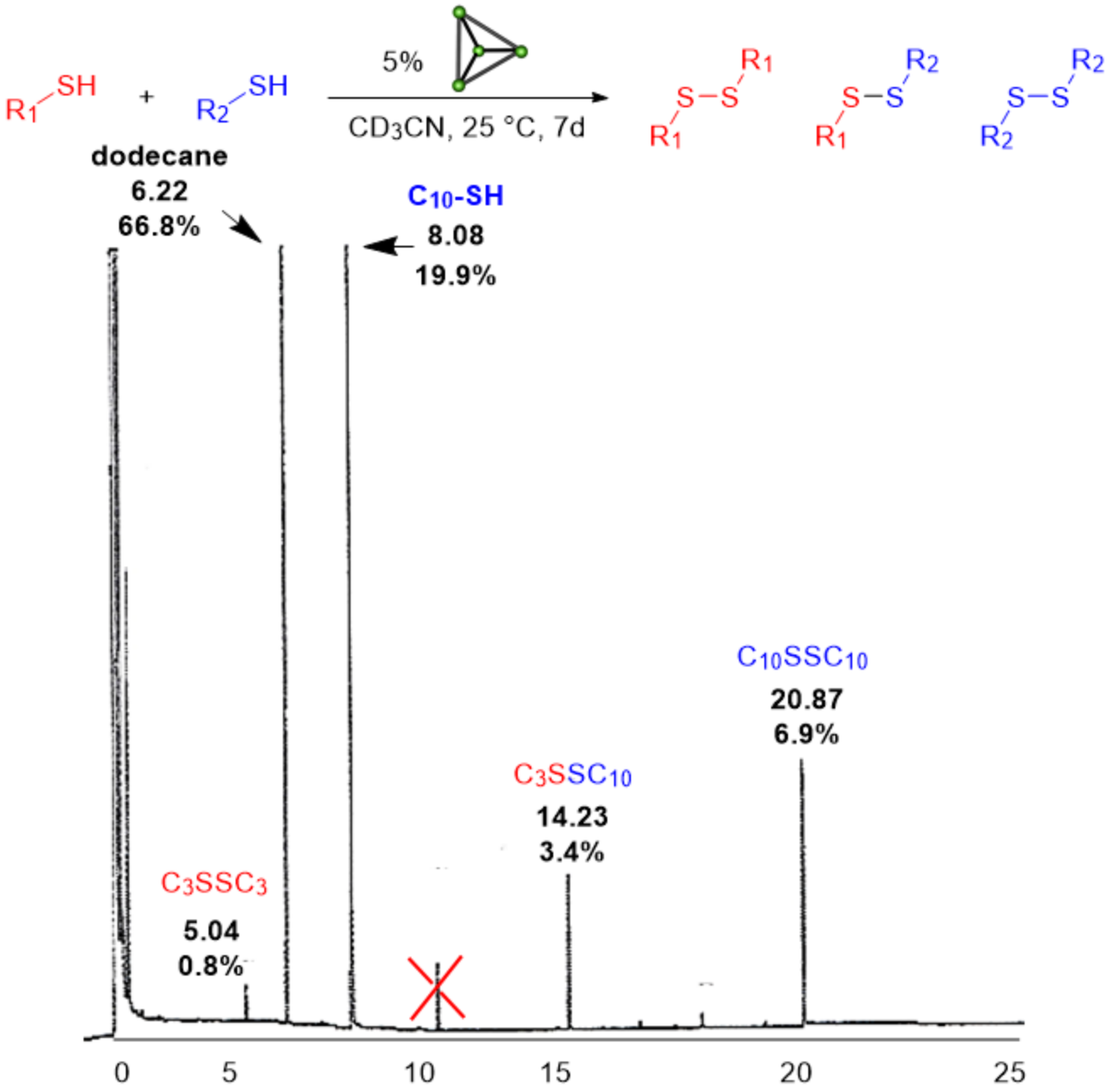

Figure S-9. GC chromatogram trace of size selective alkane thiol oxidation of an equimolar mixture of **C_3-SH** and **C_{10}-SH** using dodecane as an internal standard. [**C_x-SH**] = 18.2 mM, [**1**] = 0.9 mM. Reaction was performed at 25 °C in 800 µL CD_3CN monitored over time (600 MHz, 298 K, CD_3CN). GC sample contained reaction solution flushed through a silica plug with diethyl ether, in addition to a 450 µL aliquot of 9 mM solution of dodecane in diethyl ether.

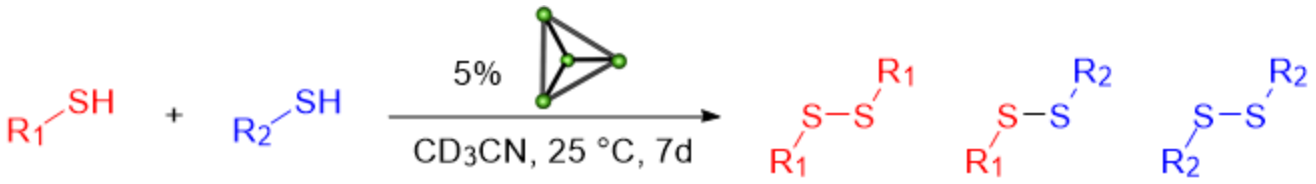

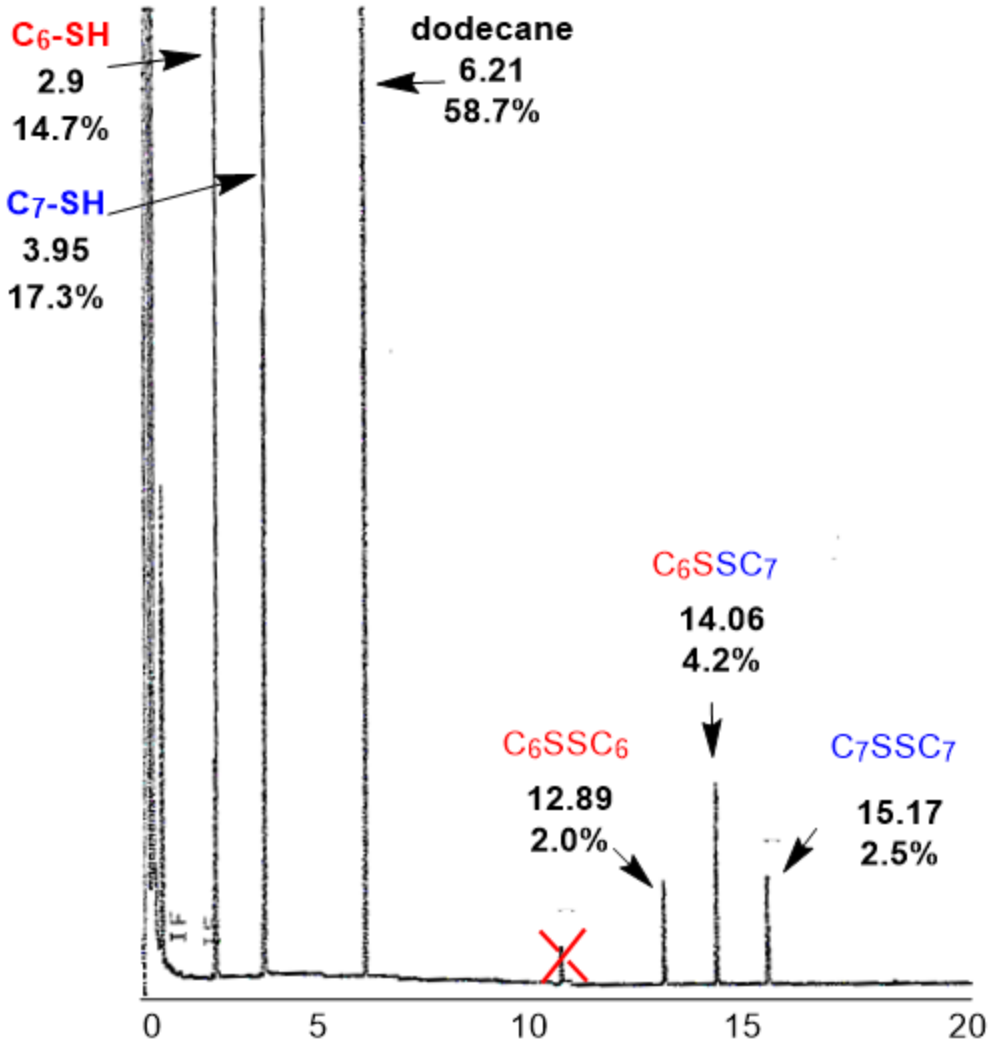

Figure S-10. GC chromatogram trace of size selective alkane thiol oxidation of an equimolar mixture of **C$_6$-SH** and **C$_7$-SH** using dodecane as an internal standard. [**C$_x$-SH**] = 18.2 mM, [**1**] = 0.9 mM. Reaction was performed at 25 °C in 800 µL CD_3CN monitored over time (600 MHz, 298 K, CD_3CN). GC sample contained reaction solution flushed through a silica plug with diethyl ether, in addition to a 450 µL aliquot of 9 mM solution of dodecane in diethyl ether.

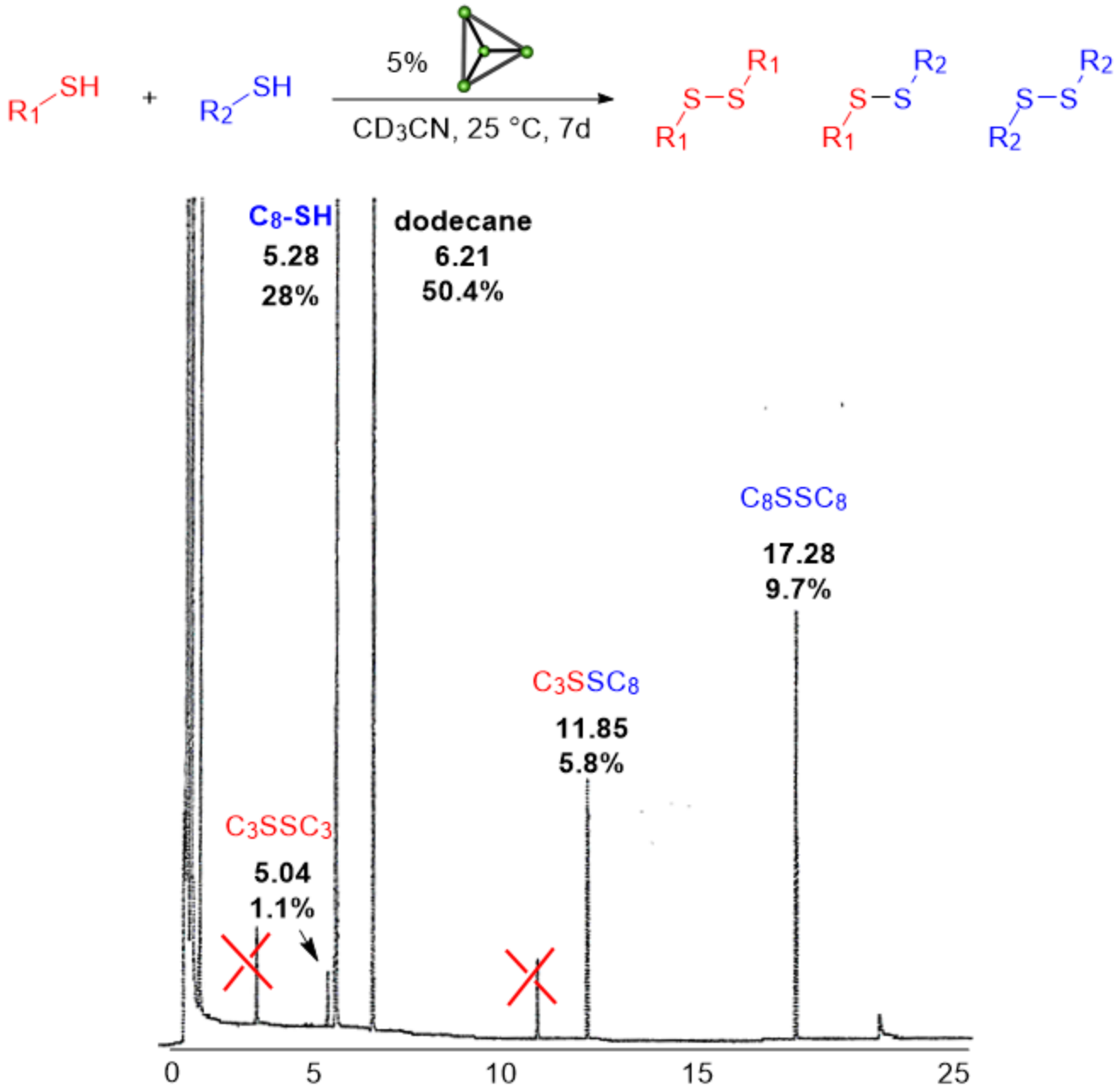

Figure S-11. GC chromatogram trace of size selective alkane thiol oxidation of an equimolar mixture of **C3-SH** and **C8-SH** using dodecane as an internal standard. [**Cx-SH**] = 18.2 mM, [**1**] = 0.9 mM. Reaction was performed at 25 °C in 800 µL CD_3CN monitored over time (600 MHz, 298 K, CD_3CN). GC sample contained reaction solution flushed through a silica plug with diethyl ether in addition to a 450 µL aliquot of 9 mM solution of dodecane in diethyl ether.

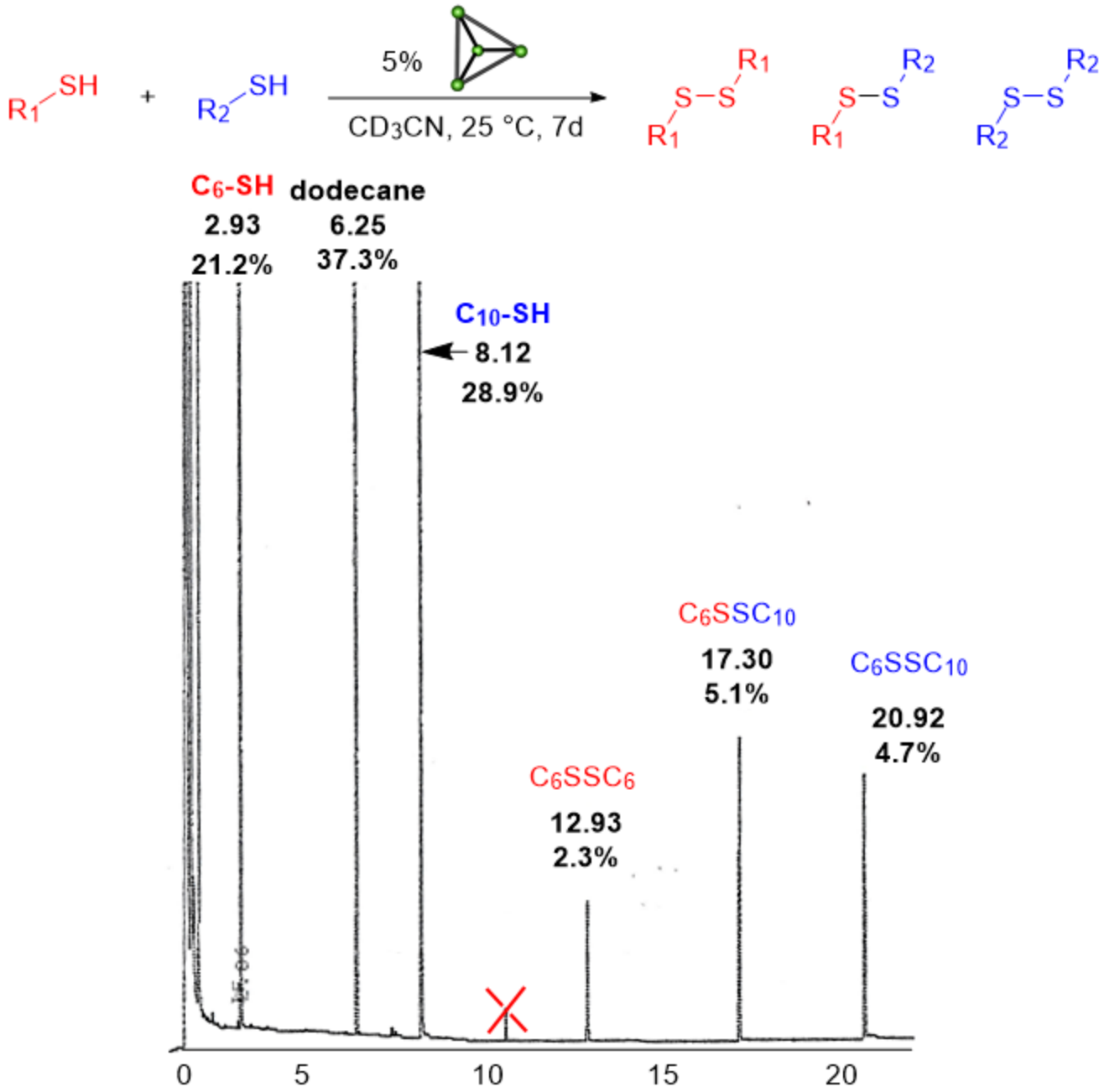

Figure S-12. GC chromatogram trace of size selective alkane thiol oxidation of an equimolar mixture of **C_6-SH** and **C_{10}-SH** using dodecane as an internal standard. [**C_x-SH**] = 18.2 mM, [**1**] = 0.9 mM. Reaction was performed at 25 °C in 800 µL CD_3CN monitored over time (600 MHz, 298 K, CD_3CN). GC sample contained reaction solution flushed through a silica plug with diethyl ether in addition to a 450 µL aliquot of 9 mM solution of dodecane in diethyl ether.

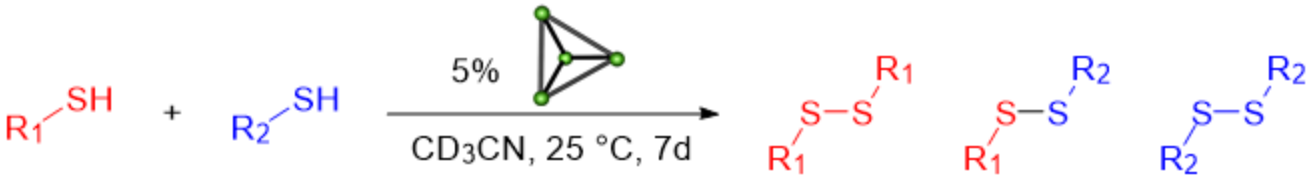

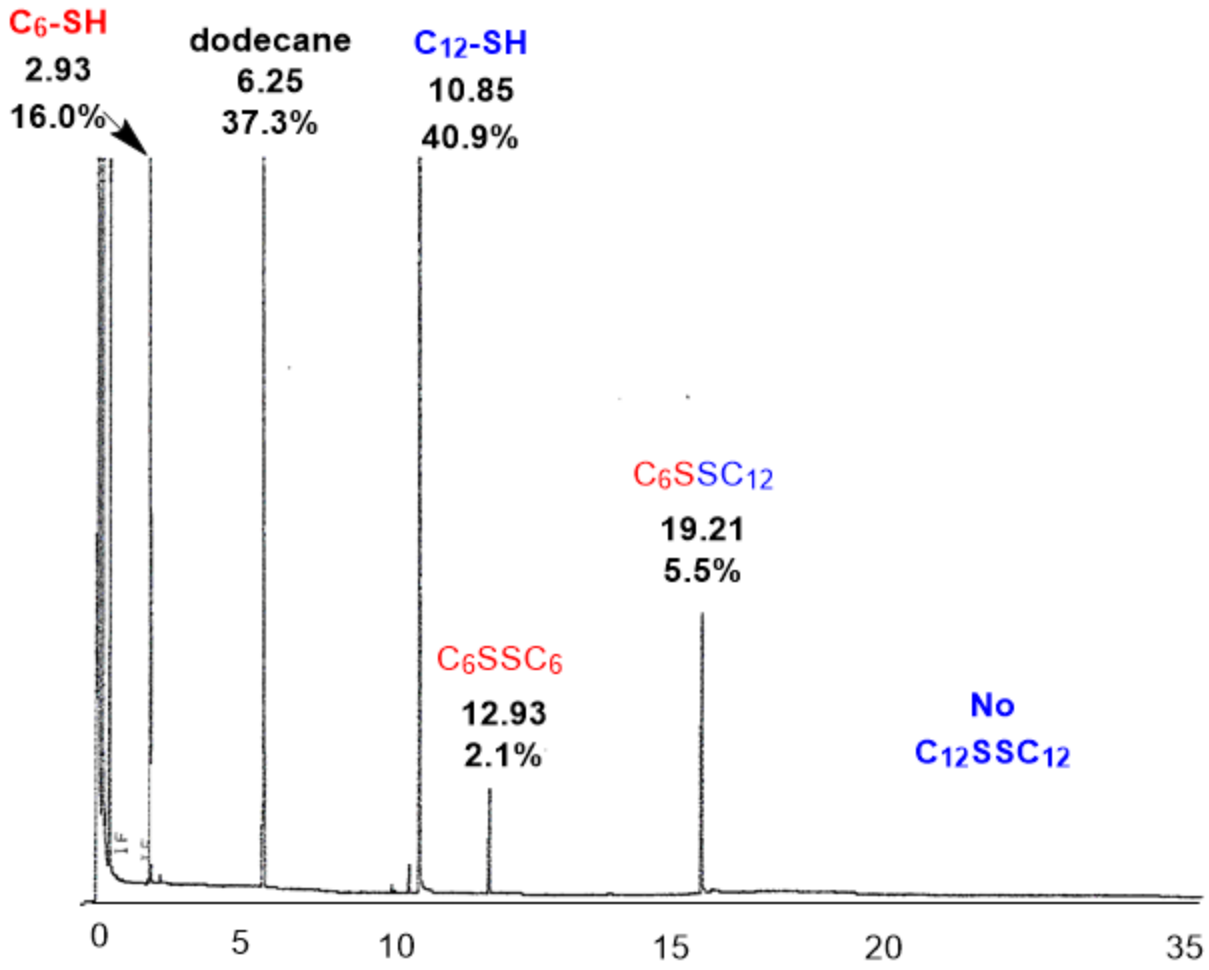

Figure S-13. GC chromatogram trace of size selective alkane thiol oxidation of an equimolar mixture of **C_6-SH** and **C_{12}-SH** using dodecane as an internal standard. [**C_x-SH**] = 18.2 mM, [**1**] = 0.9 mM. Reaction was performed at 25 °C in 800 µL CD_3CN monitored over time (600 MHz, 298 K, CD_3CN). GC sample contained reaction solution flushed through a silica plug with diethyl ether in addition to a 450 µL aliquot of 9 mM solution of dodecane in diethyl ether.

IV. Binding Studies

General procedure for binding affinity calculations. A 1.5 μM solution of cage **1** was prepared in spectroscopic grade CH_3CN via dilutions from a 0.3 mM stock solution, and added to a UV-Vis cuvette. To this solution was then added 0.1-5 μL aliquots from a 4.5 mM solution of the corresponding guest molecule, equating to one molar equivalent guest to cage. These additions were continued until there was no observable change in the absorption spectrum. Binding affinities were calculated via linear regression analysis using the Nelder-Mead method from the change in absorbance at two points (330nm and 370nm for **1**, 278/335 nm for **2**), the data was fit to either a 1:1 or 1:2 binding model and the variance used to determine best fit using a non-linear least-squares (maximum likelihood) approach written within the Mathematica programming environment.

Binding constants for 1:1 and 1:2 host-guest complex models were determined by UV/Vis titration experiments and binding constants extracted following the general approach outlined by Thordarson,[2] modified as described below. In brief, UV/Vis absorptions at 300 and 370 nm (for **1**, 278/335 nm for **2**), were monitored as a function of added guest and simultaneously fit using a non-linear least-squares (maximum likelihood) approach written within the Mathematica programming environment.[3] For the 1:1 equilibrium model, the binding constant (K_a) and molar absorptivities (at both wavelengths) for the pure host (H) and host-guest (HG) complex were determined. For the 1:2 equilibrium model, both the first (K_1) and second (K_2) binding constants were determined, along with molar absorptivities for the host, host-guest (HG), and host-dual-guest (HG_2) complexes. The precise equilibria and corresponding equations are detailed below. Error bars for each of the fit parameters were determined by a numerical calculation of the covariance matrix and are reported above as ± standard error.[4] The error analysis assumes normally distributed, random error that is independent of data point; in such a case, the sum of the squared-residuals follows the chi-squared distribution for N-k degrees of freedom, where N is the number of measured data points and k the number of fit parameters (5 and 8 for the 1:1 and 1:2 models, respectively). The significance of the 1:2 model was judged based on the inverse ratio of the squared residuals compared to the 1:1 model. Again, if the errors are normally distributed, this ratio follows the F-distribution for N-5 (numerator) and N-8 (denominator) degrees of freedom.[5] To be considered statistically "better," the 1:2 model must improve the residuals beyond what normal statistical fluctuations would be expected to sample with the observed noise and finite number of measured points. This is quantified via the p-value, which gives the probability that the observed improvement in residuals for the 1:2 complex model can be explained as statistical "luck." A small value indicates that the model truly is better – that is, that more of

the underlying data trends are reproduced so that the residuals are actually smaller. To be considered significant in this context, we take p-values below 0.001.

Equilibrium Models:[2]

The 1:1 host-guest binding

$$H + G \underset{}{\overset{K_a}{\rightleftharpoons}} HG$$

has an association constant

$$K_a = \frac{[HG]}{[H][G]}$$

from which the concentration of the host, guest, and complex can be related back to initial (or total added) concentrations, H_0 and G_0, of each

$$[H] = \frac{1}{2}\left(H_0 - G_0 - \frac{1}{K_a} \right) + \frac{1}{2}\sqrt{\left(G_0 - H_0 - \frac{1}{K_a} \right)^2 + 4\frac{G_0}{K_a}}$$

$$[G] = \frac{1}{2}\left(G_0 - H_0 - \frac{1}{K_a} \right) + \frac{1}{2}\sqrt{\left(G_0 - H_0 - \frac{1}{K_a} \right)^2 + 4\frac{G_0}{K_a}}$$

$$[HG] = \frac{1}{2}\left(G_0 + H_0 + \frac{1}{K_a} \right) - \frac{1}{2}\sqrt{\left(G_0 - H_0 - \frac{1}{K_a} \right)^2 + 4\frac{G_0}{K_a}}$$

The absorbance at a given wavelength λ can then be written as

$$\begin{aligned} A^{\lambda} &= \varepsilon_H^{\lambda}[H] + \varepsilon_{HG}^{\lambda}[HG] \\ &= \varepsilon_H^{\lambda}\left\{ \frac{1}{2}\left(H_0 - G_0 - \frac{1}{K_a} \right) + \frac{1}{2}\sqrt{\left(G_0 - H_0 - \frac{1}{K_a} \right)^2 + 4\frac{G_0}{K_a}} \right\} + \\ &\quad \varepsilon_{HG}^{\lambda}\left\{ \frac{1}{2}\left(G_0 + H_0 + \frac{1}{K_a} \right) - \frac{1}{2}\sqrt{\left(G_0 - H_0 - \frac{1}{K_a} \right)^2 + 4\frac{G_0}{K_a}} \right\} \end{aligned}$$

where it assumed that the guest on its own does not absorb. This is the expression that is used to simultaneously fit the experimental absorption data at 300 and 370 nm, A^{300} and A^{370}, as a function of added guest, G_o, to determine K_a and $\varepsilon_H^{300}, \varepsilon_{HG}^{300}, \varepsilon_H^{370}$, and ε_{HG}^{370}.

The 1:2 host-guest binding is assumed to be a non-cooperative, sequential two-step process

$$H + G \overset{K_1}{\rightleftharpoons} HG$$
$$HG + G \overset{K_2}{\rightleftharpoons} HG_2$$

which is characterized by two binding constants

$$K_1 = \frac{[HG]}{[H][G]}$$
$$K_2 = \frac{[HG_2]}{[HG][G]}$$

We analyze this for the case in which the approximation $[G] \approx G_0$ is valid, which corresponds to the limit in which $K_1[H] << 1$ or when G_0 is in large excess. This condition can be relaxed, but appears valid in our situation. With these caveats,

$$[H] = \frac{H_0}{1 + K_1 G_0 + K_1 K_2 G_0^2}$$

$$[G] \approx G_0$$

$$[HG] = \frac{K_1 H_0 G_0}{1 + K_1 G_0 + K_1 K_2 G_0^2}$$

$$[HG_2] = \frac{K_1 K_2 H_0 G_0^2}{1 + K_1 G_0 + K_1 K_2 G_0^2}$$

and the absorbance can be written

$$A^\lambda = \varepsilon_H^\lambda [H] + \varepsilon_{HG}^\lambda [HG] + \varepsilon_{HG_2}^\lambda [HG_2]$$
$$= \varepsilon_H^\lambda \frac{H_0}{1 + K_1 G_0 + K_1 K_2 G_0^2} + \varepsilon_{HG}^\lambda \frac{K_1 H_0 G_0}{1 + K_1 G_0 + K_1 K_2 G_0^2} + \varepsilon_{HG_2}^\lambda \frac{K_1 K_2 H_0 G_0^2}{1 + K_1 G_0 + K_1 K_2 G_0^2}.$$

This expression is used to simultaneously fit the experimental absorption data at 300 and 370 nm, A^{300} and A^{370}, as a function of added guest, G_o, to determine K_1, K_2, $\varepsilon_H^{300}, \varepsilon_{HG}^{300}, \varepsilon_{HG_2}^{300}$, $\varepsilon_H^{370}, \varepsilon_{HG}^{370}$, and $\varepsilon_{HG_2}^{370}$.

a. UV-Vis Absorbance Titrations and Fitting Curves

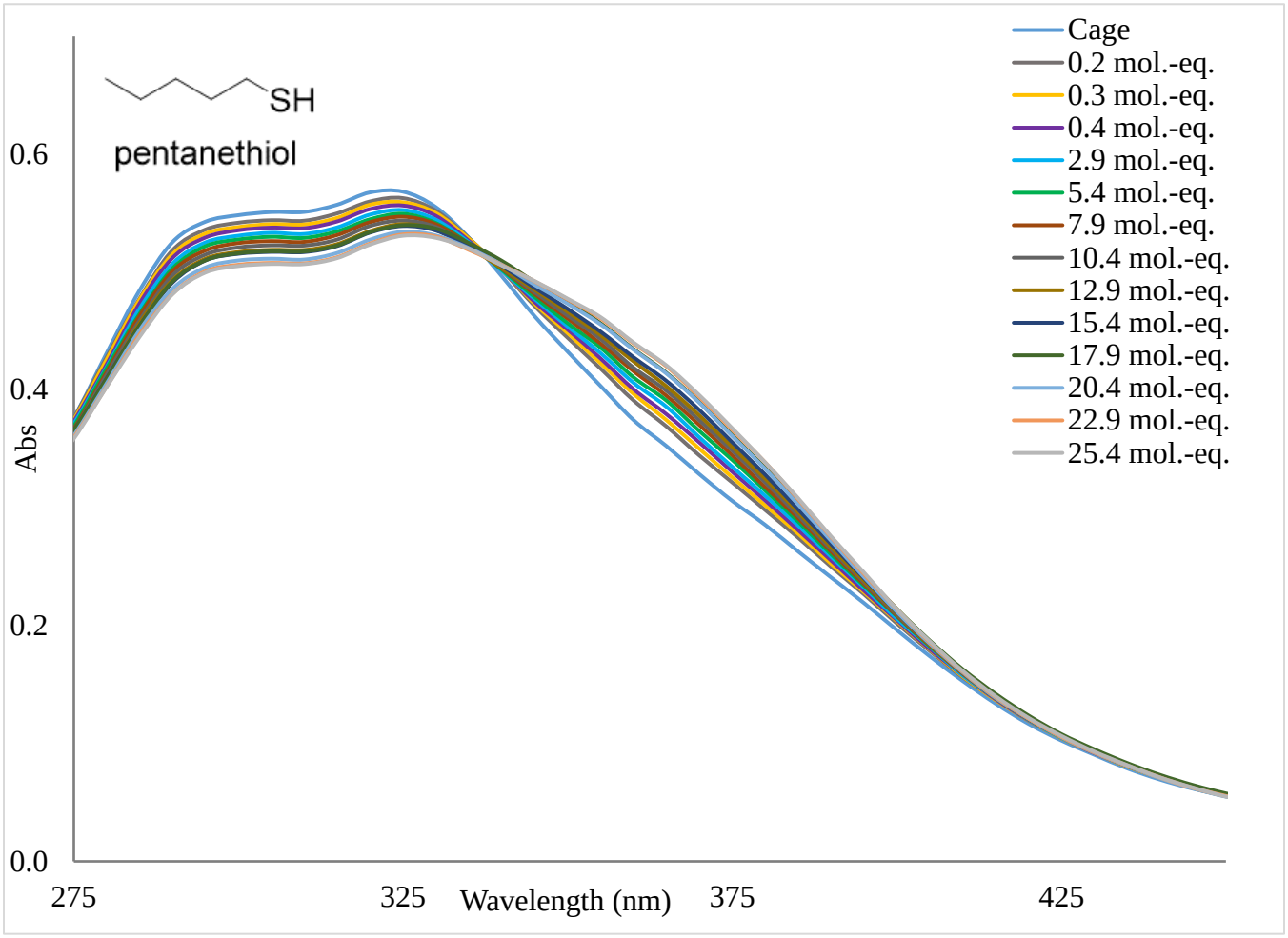

Figure S-14. UV-Vis absorption spectrum of the titration of **C_5-SH** into a 3 µM solution of cage **1** in CH_3CN. **C_5-SH** was added in 0.2-3 µL aliquots from a 9 mM stock solution in CH_3CN.

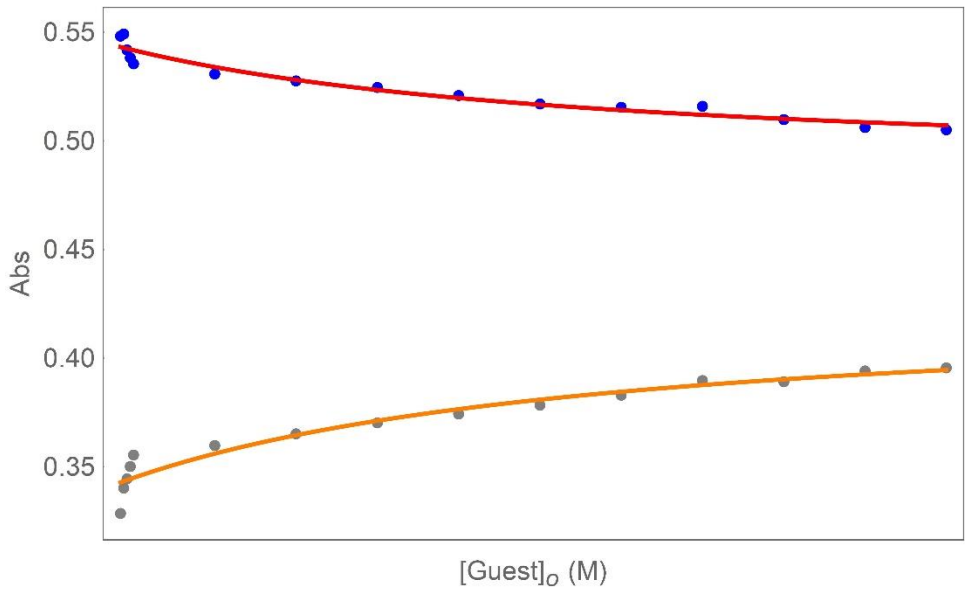

Residuals 330 nm

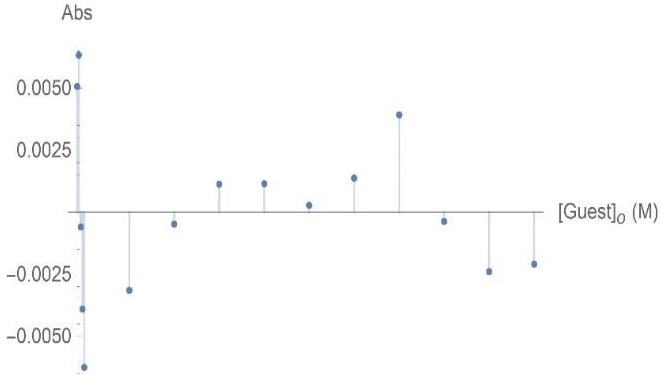

Residuals 370 nm

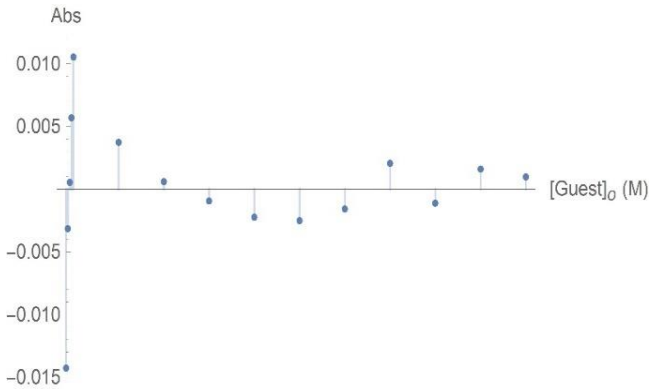

Figure S-15. Fitting curves and plots of residual magnitude obtained when fitting the UV binding data for **C$_5$-SH** with cage **1** to the 1:1 binding model.

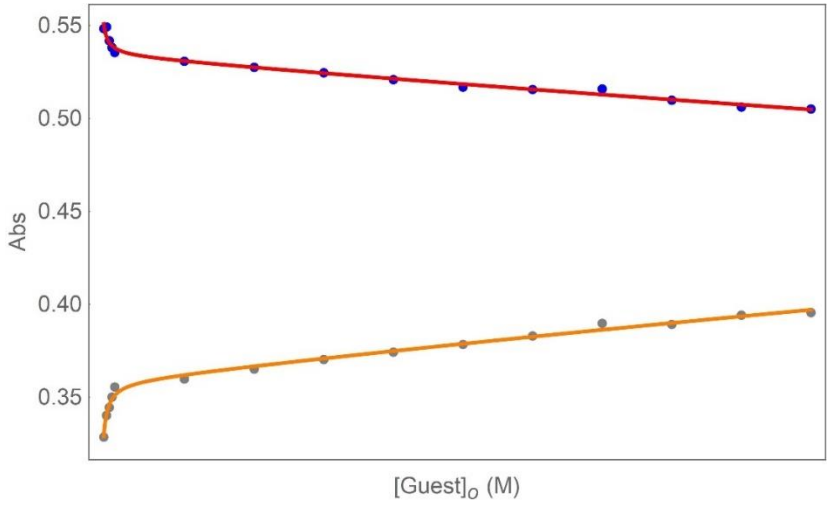

Residuals 330 nm

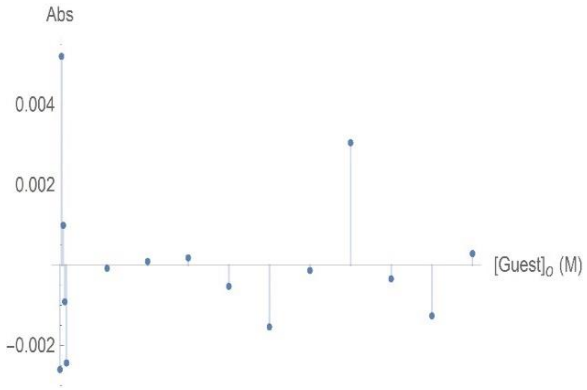

Residuals 370 nm

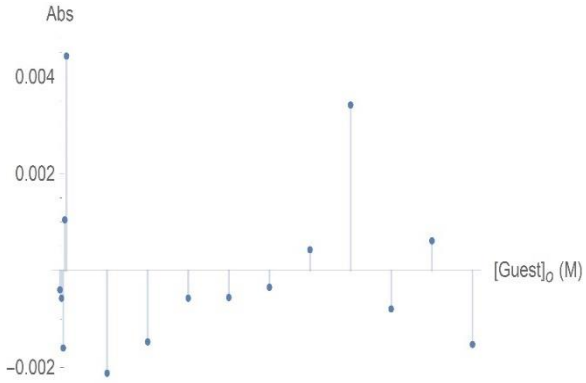

Figure S-16. Fitting curves and plots of residual magnitude obtained when fitting the UV binding data for **C$_5$-SH** with cage **1** to the 1:2 binding model.

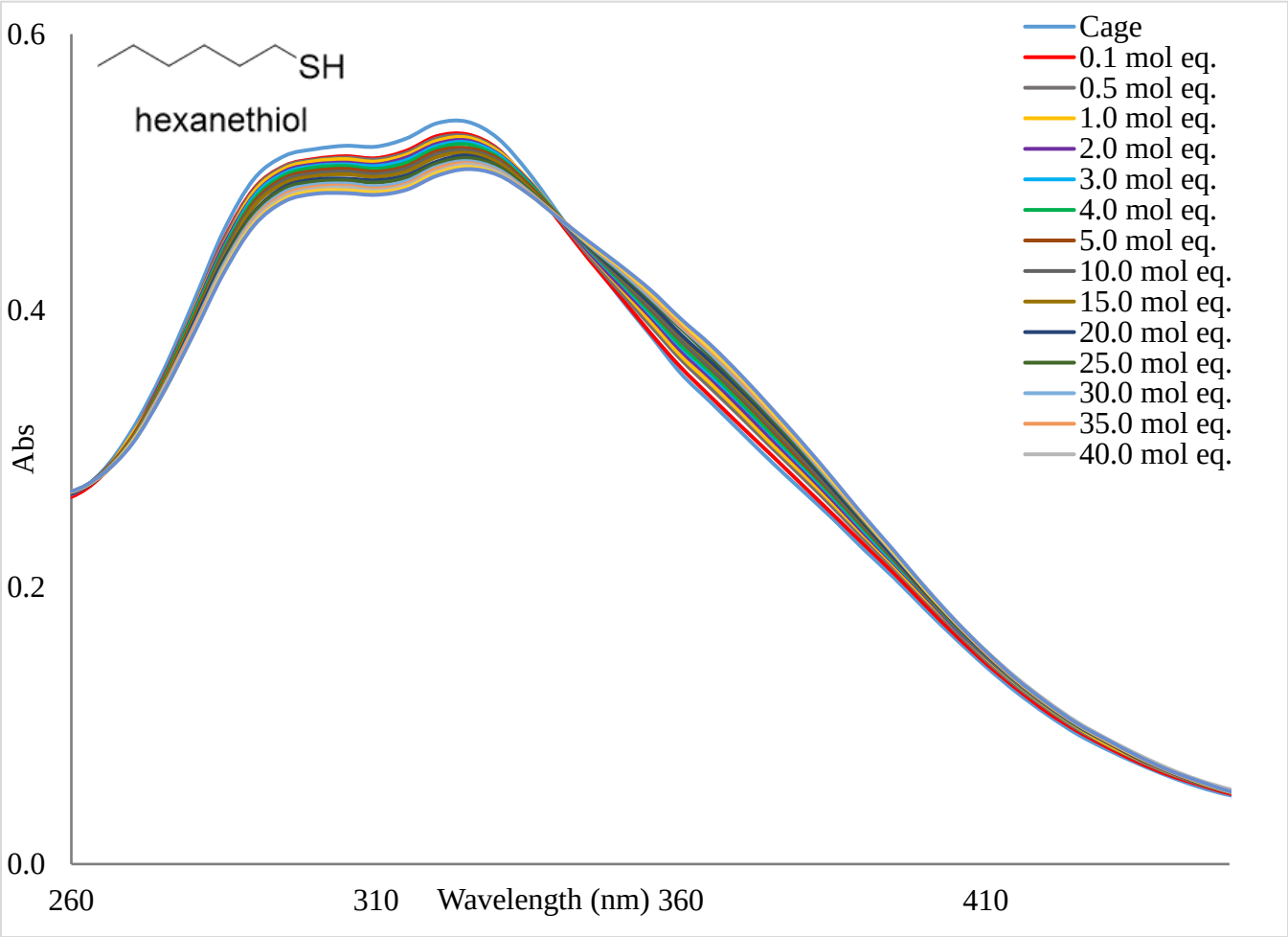

Figure S-17. UV-Vis absorption spectrum of the titration of **C_6-SH** into a 3 µM solution of cage **1** in CH_3CN. **C_6-SH** was added in 0.1-5 µL aliquots from a 9 mM stock solution in CH_3CN.

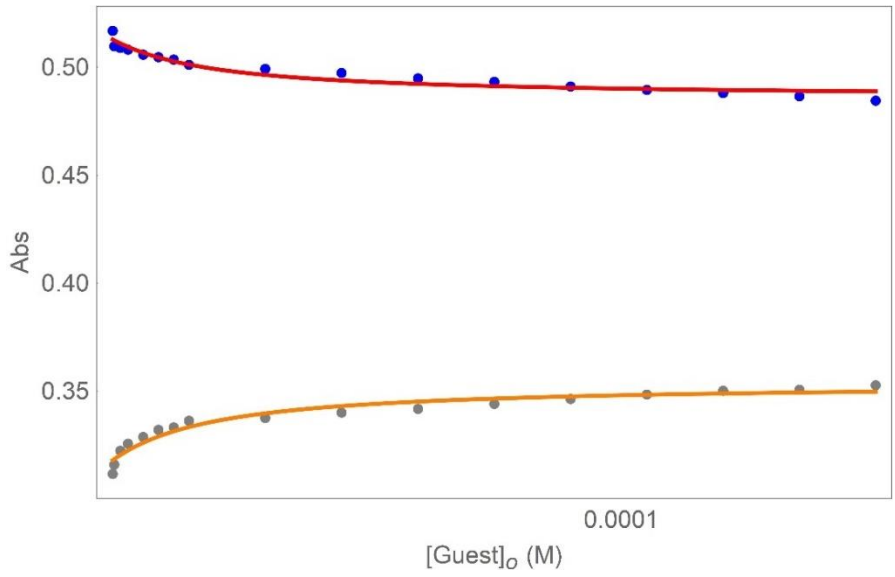

Residuals 330 nm

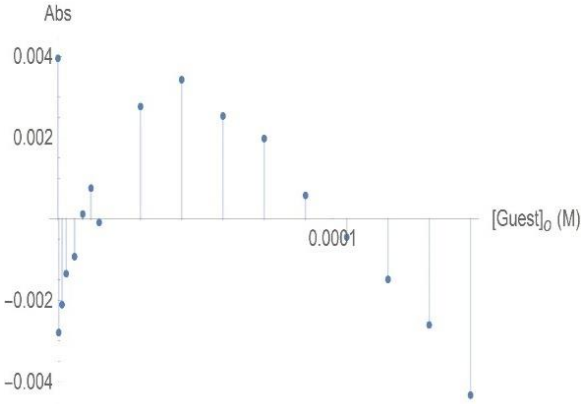

Residuals 370 nm

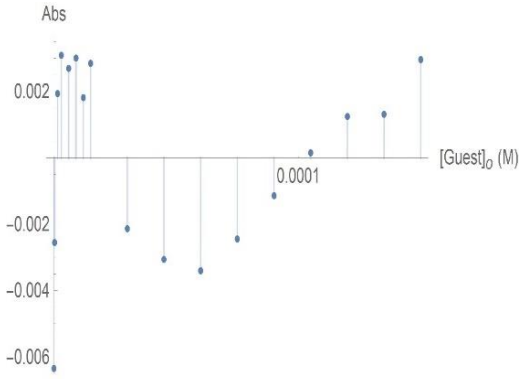

Figure S-18. Fitting curves and plots of residual magnitude obtained when fitting the UV binding data for **C$_6$-SH** with cage **1** to the 1:1 binding model.

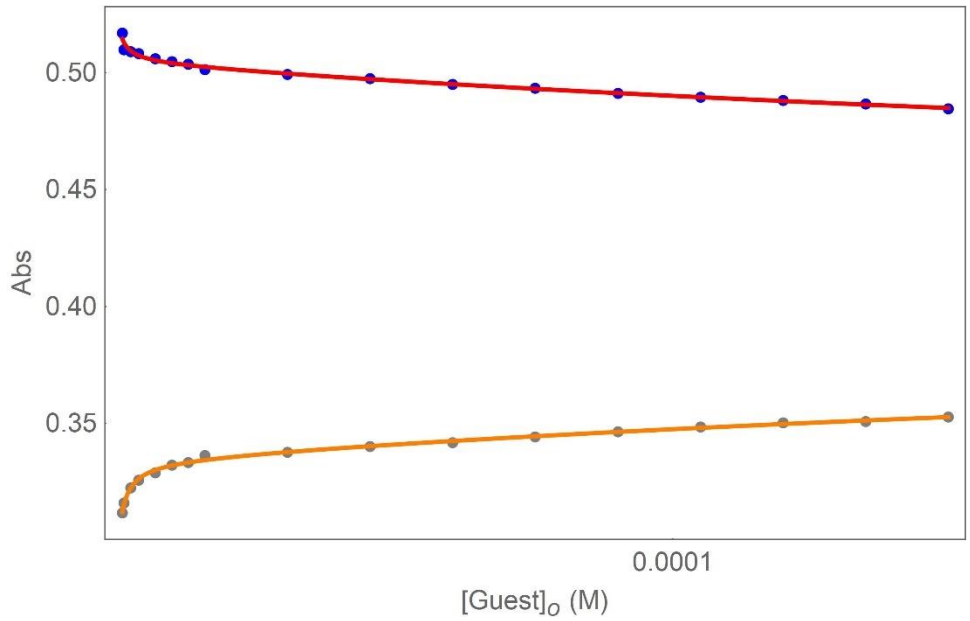

Residuals 330 nm

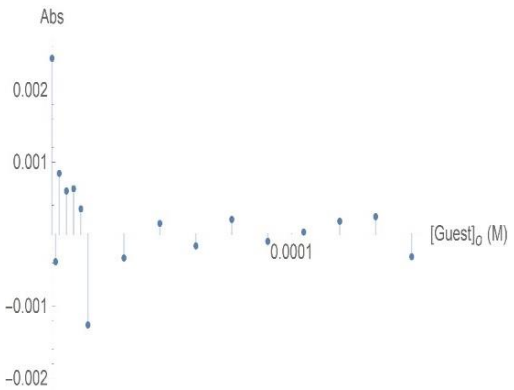

Residuals 370 nm

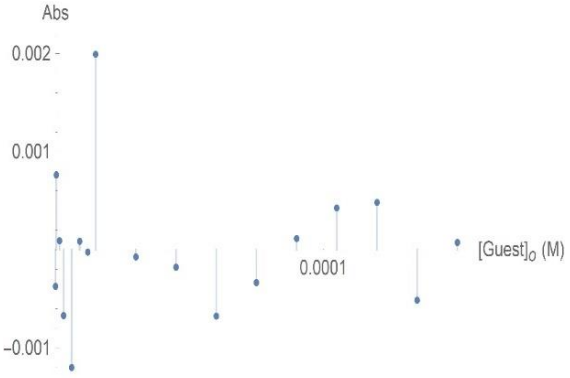

Figure S-19. Fitting curves and plots of residual magnitude obtained when fitting the UV binding data for **C$_6$-SH** with cage **1** to the 1:2 binding model.

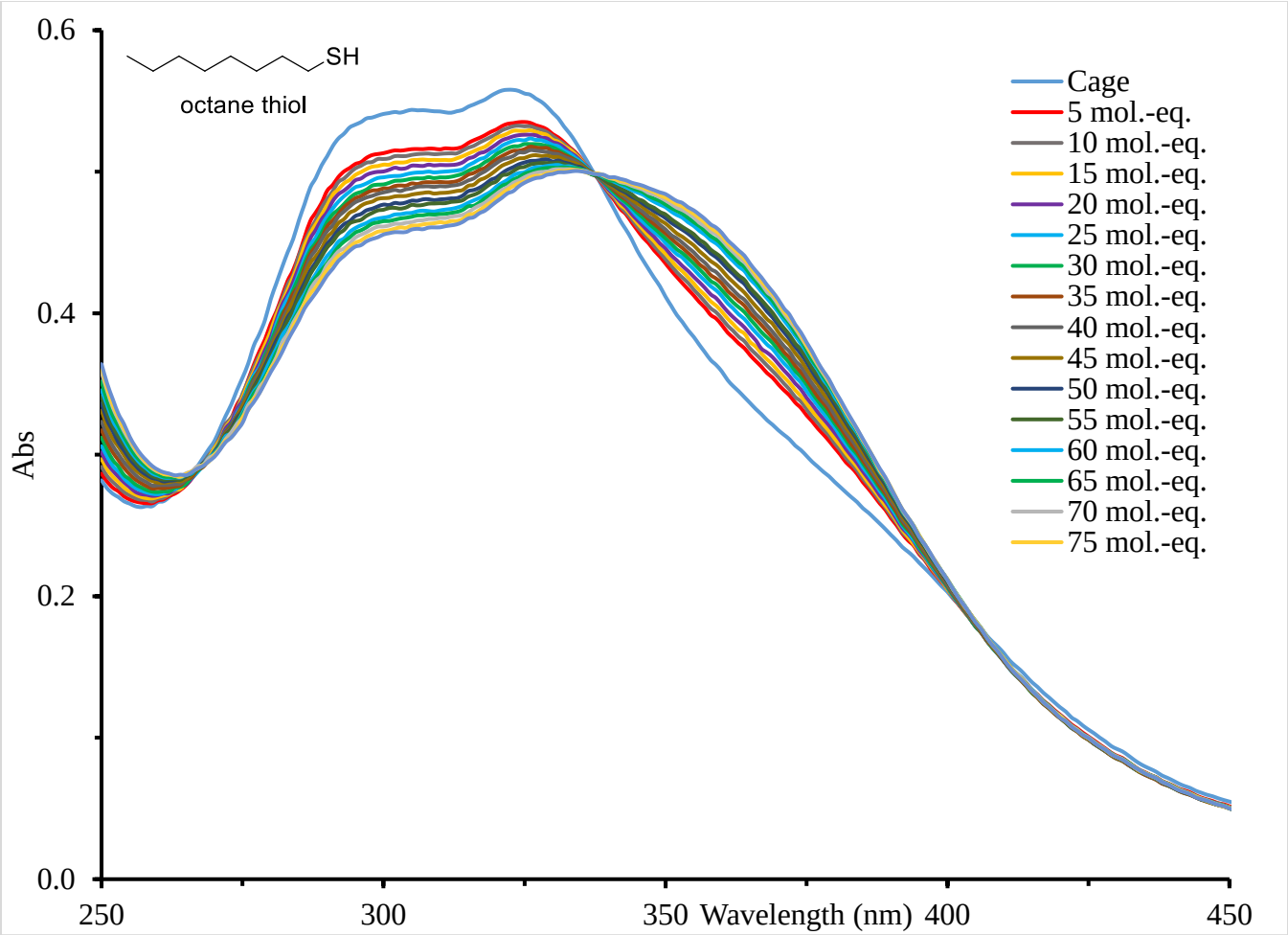

Figure S-20. UV-Vis absorption spectrum of the titration of **C_8-SH** into a 3 µM solution of cage **1** in CH_3CN. **C_8-SH** was added in 5 µL aliquots from a 9 mM stock solution in CH_3CN.

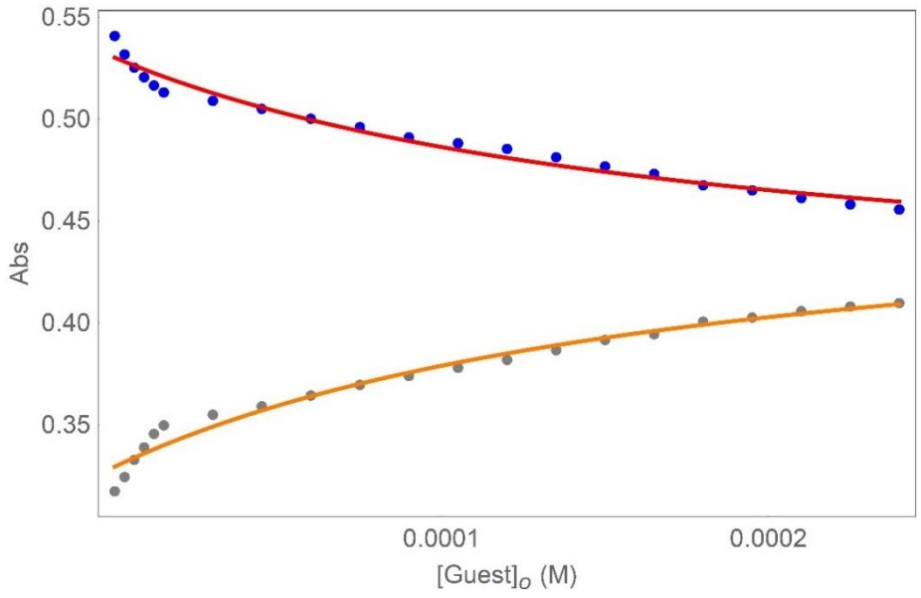

Residuals 330 nm

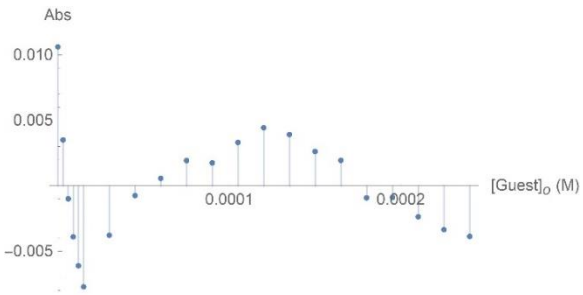

Residuals 370 nm

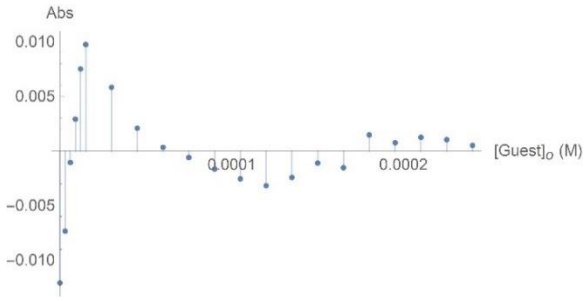

Figure S-21. Fitting curves and plots of residual magnitude obtained when fitting the UV binding data for **C_8-SH** with cage **1** to the 1:1 binding model.

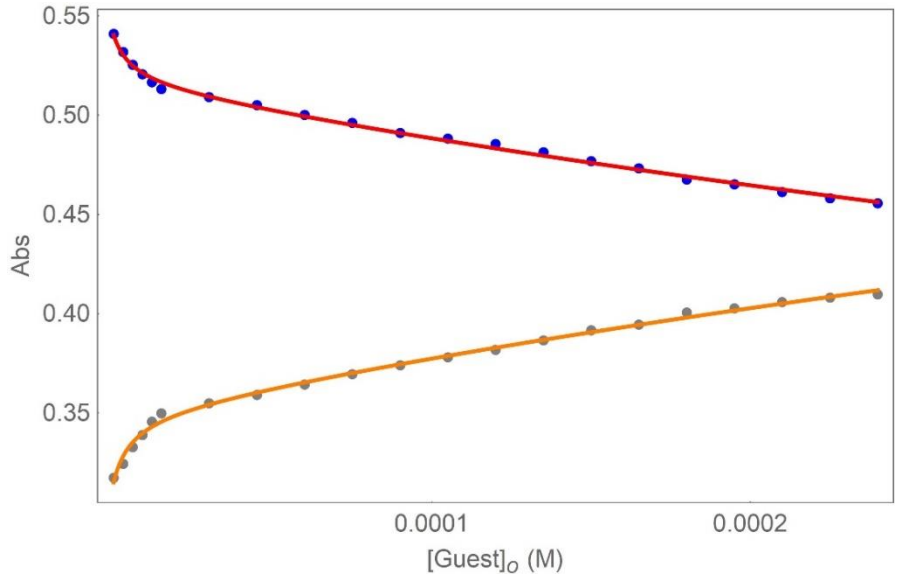

Residuals 330 nm

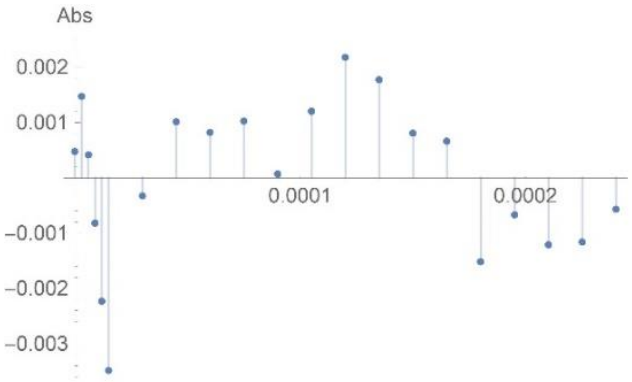

Residuals 370 nm

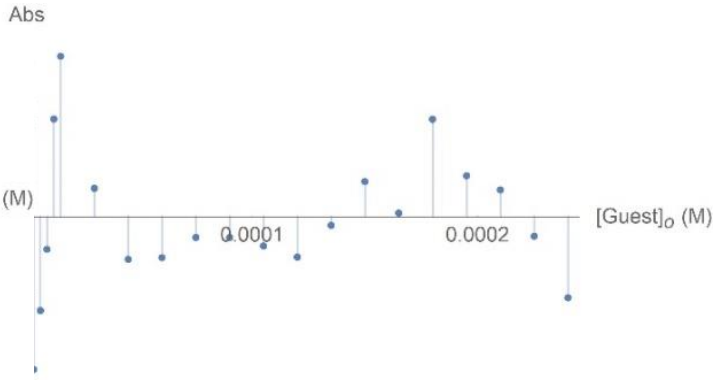

Figure S-22. Fitting curves and plots of residual magnitude obtained when fitting the UV binding data for **C_8-SH** with cage **1** to the 1:2 binding model.

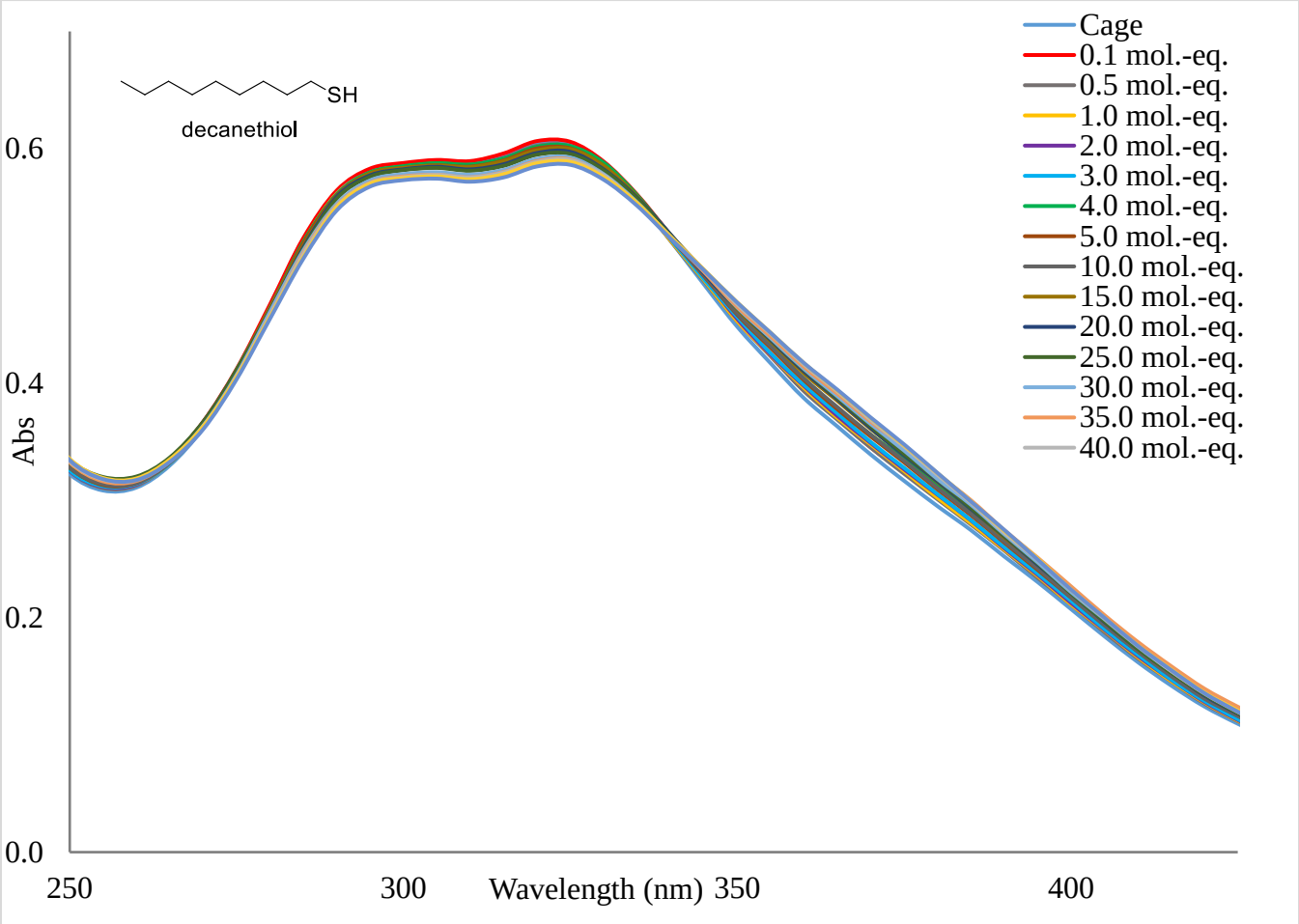

Figure S-23. UV-Vis absorption spectrum of the titration of **C_{10}-SH** into a 3 µM solution of cage **1** in CH_3CN. **C_{10}-SH** was added in 0.1-5 µL aliquots from a 9 mM stock solution in CH_3CN.

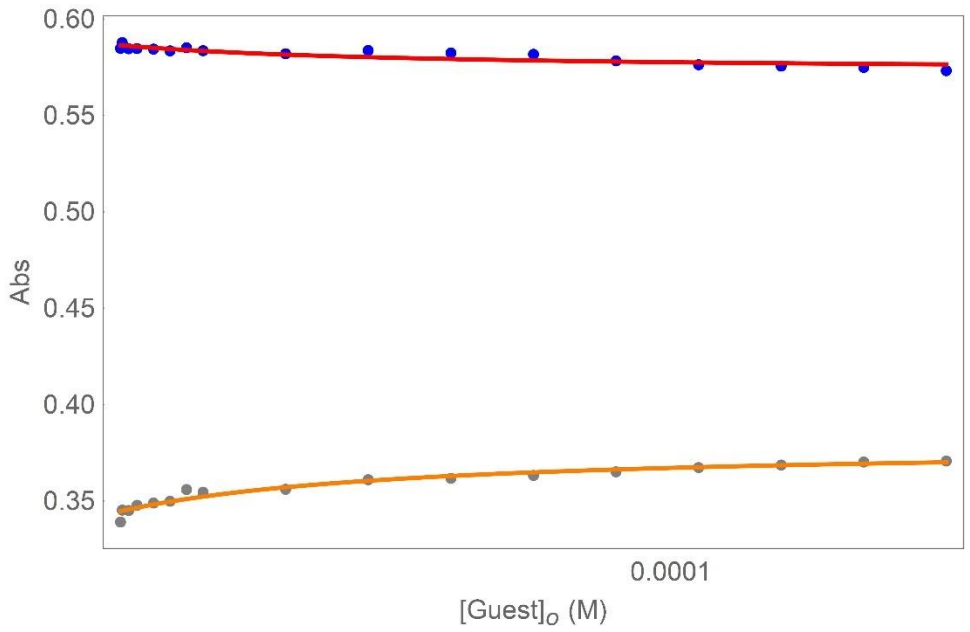

Residuals 330 nm

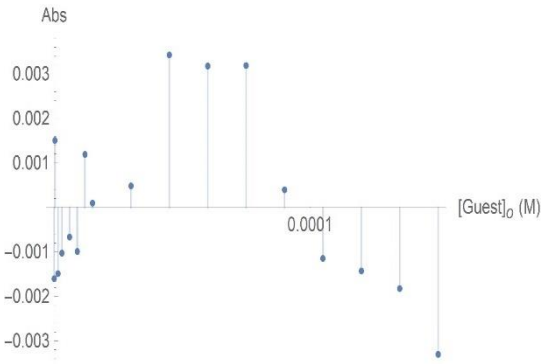

Residuals 370 nm

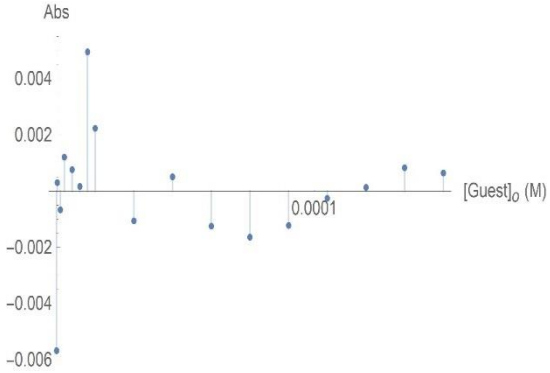

Figure S-24. Fitting curves and plots of residual magnitude obtained when fitting the UV binding data for **C$_{10}$-SH** with cage **1** to the 1:1 binding model.

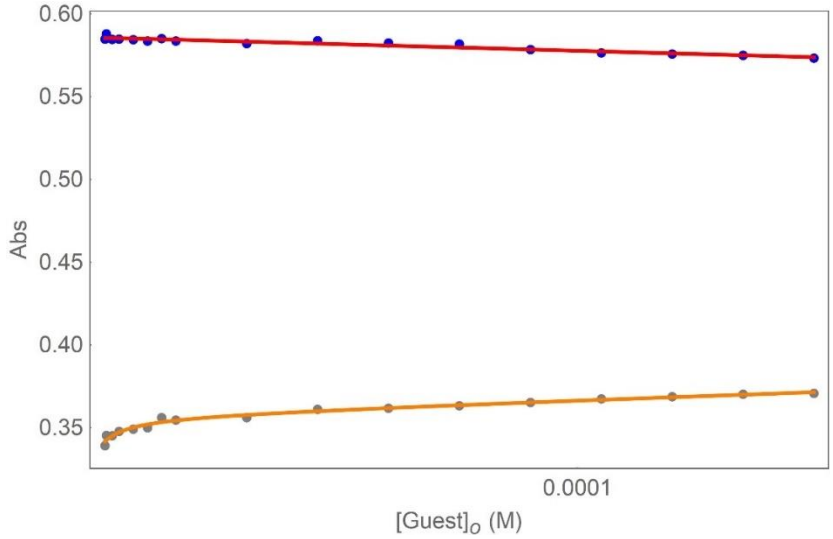

Residuals 330 nm

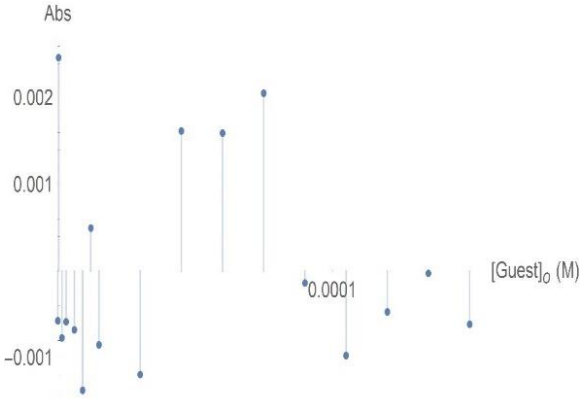

Residuals 370 nm

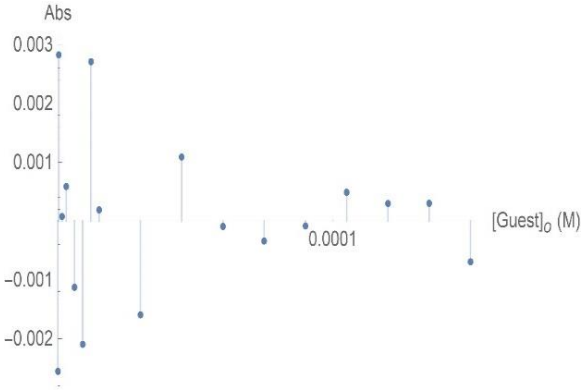

Figure S-25. Fitting curves and plots of residual magnitude obtained when fitting the UV binding data for **C$_{10}$-SH** with cage **1** to the 1:2 binding model.

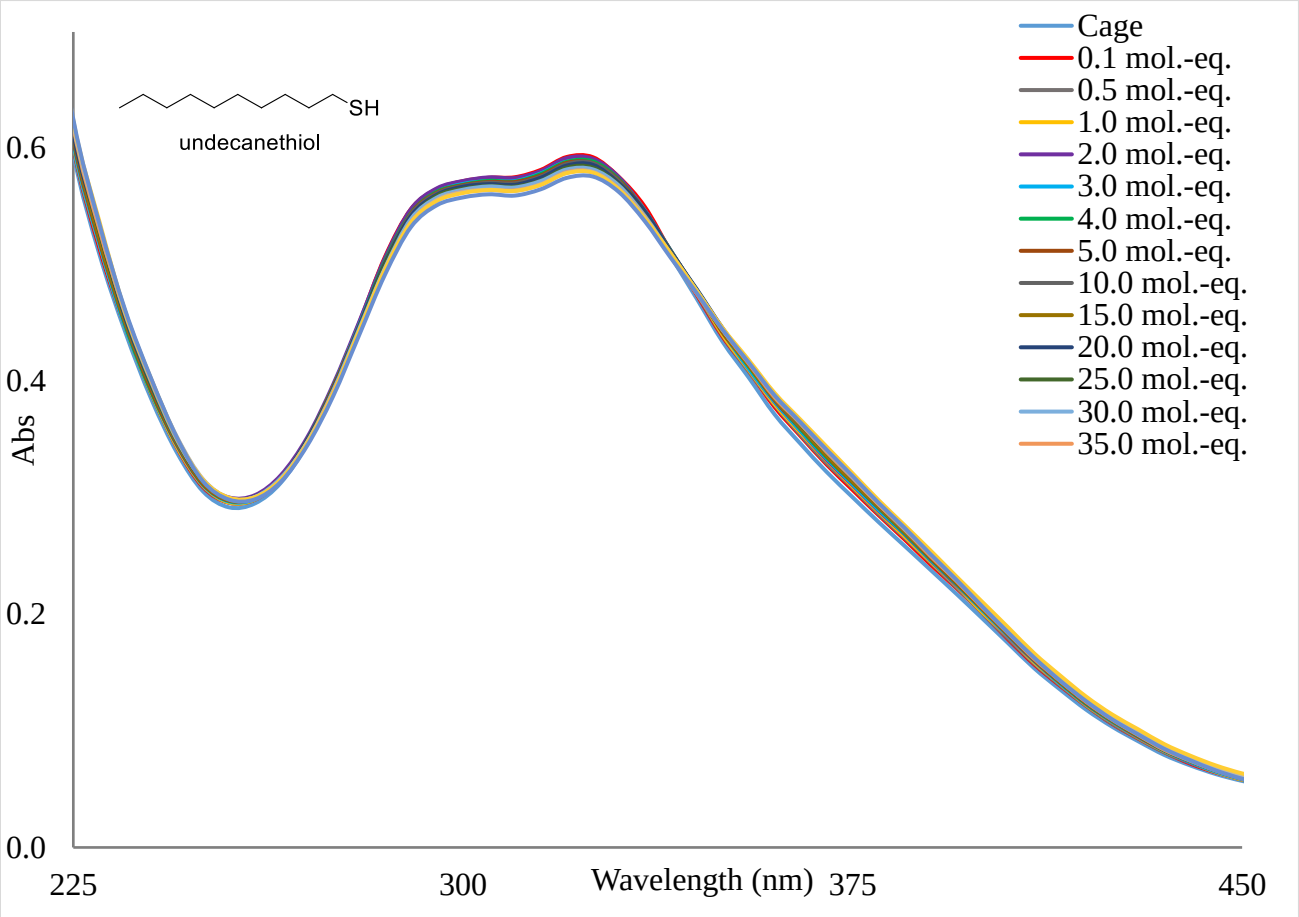

Figure S-26. UV-Vis absorption spectrum of the titration **of C_{11}-SH** into a 3 µM solution of cage **1** in CH_3CN. **C_{11}-SH** was added in 0.1-5 µL aliquots from a 9 mM stock solution in CH_3CN.

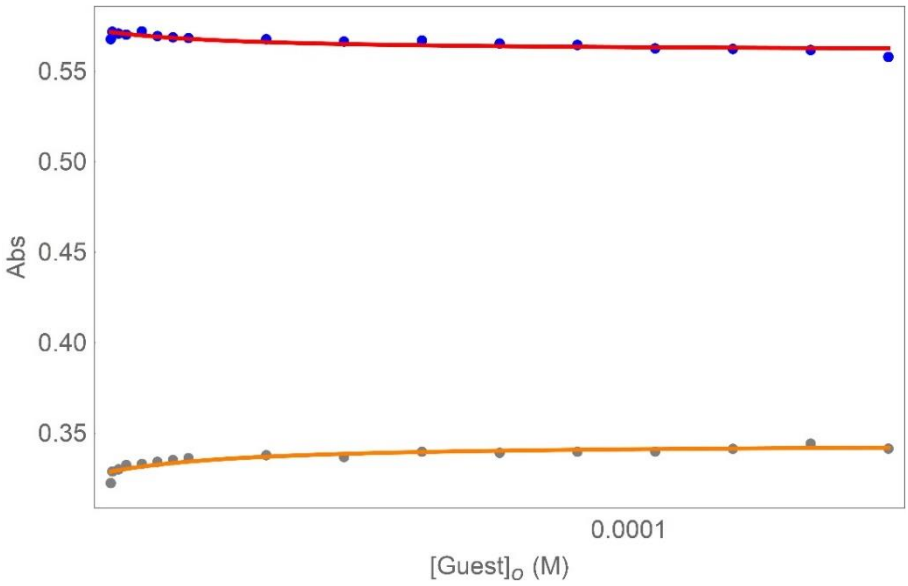

Residuals 330 nm

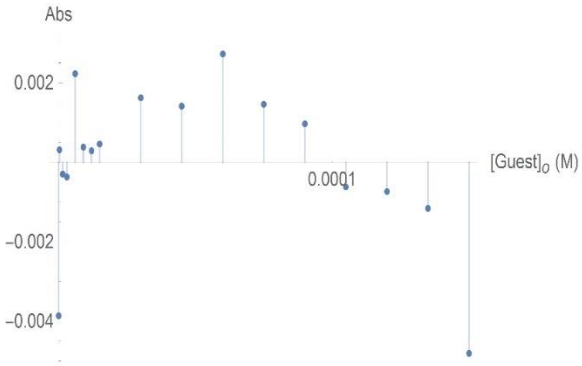

Residuals 370 nm

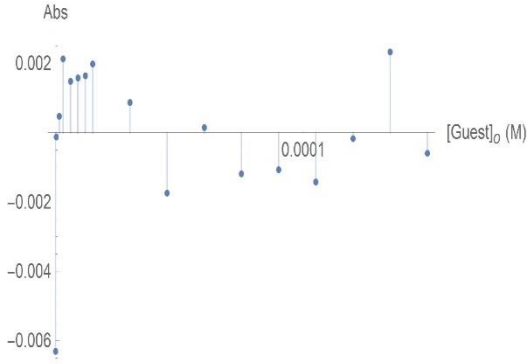

Figure S-27. Fitting curves and plots of residual magnitude obtained when fitting the UV binding data for **C_{11}-SH** with cage **1** to the 1:1 binding model.

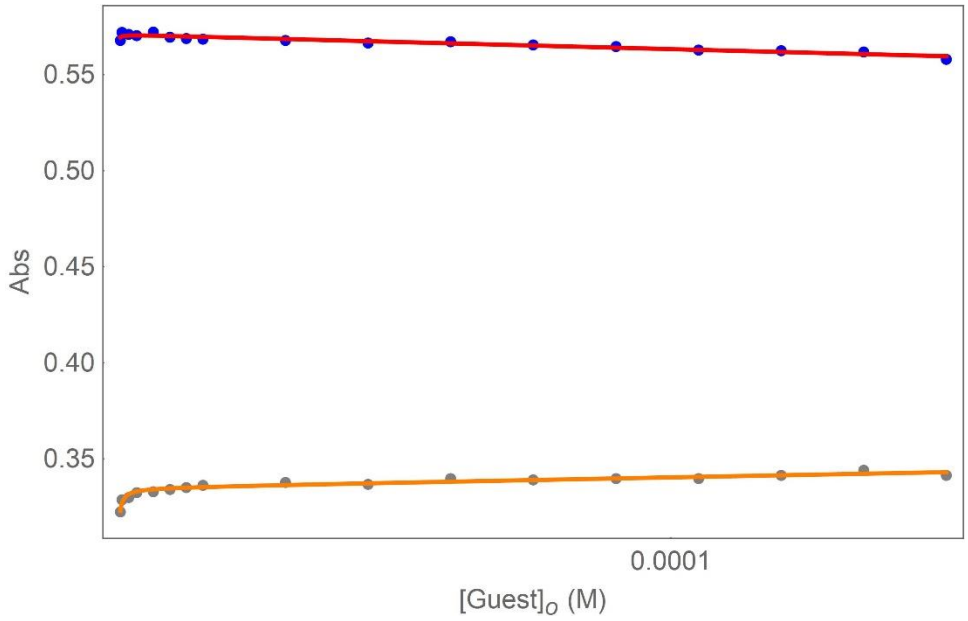

Residuals 330 nm

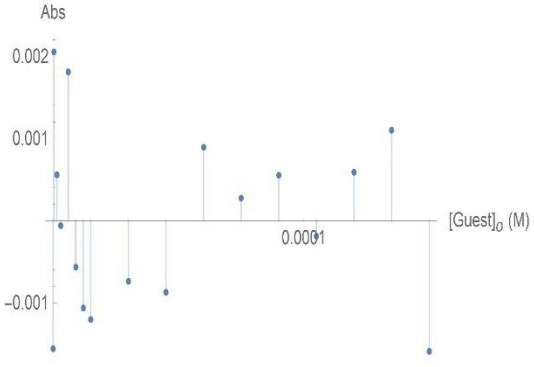

Residuals 370 nm

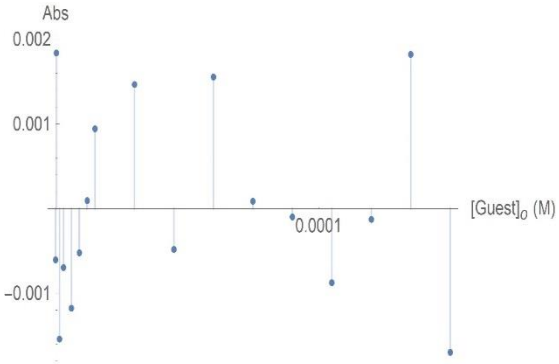

Figure S-28. Fitting curves and plots of residual magnitude obtained when fitting the UV binding data for **C_{11}-SH** with cage **1** to the 1:2 binding model.

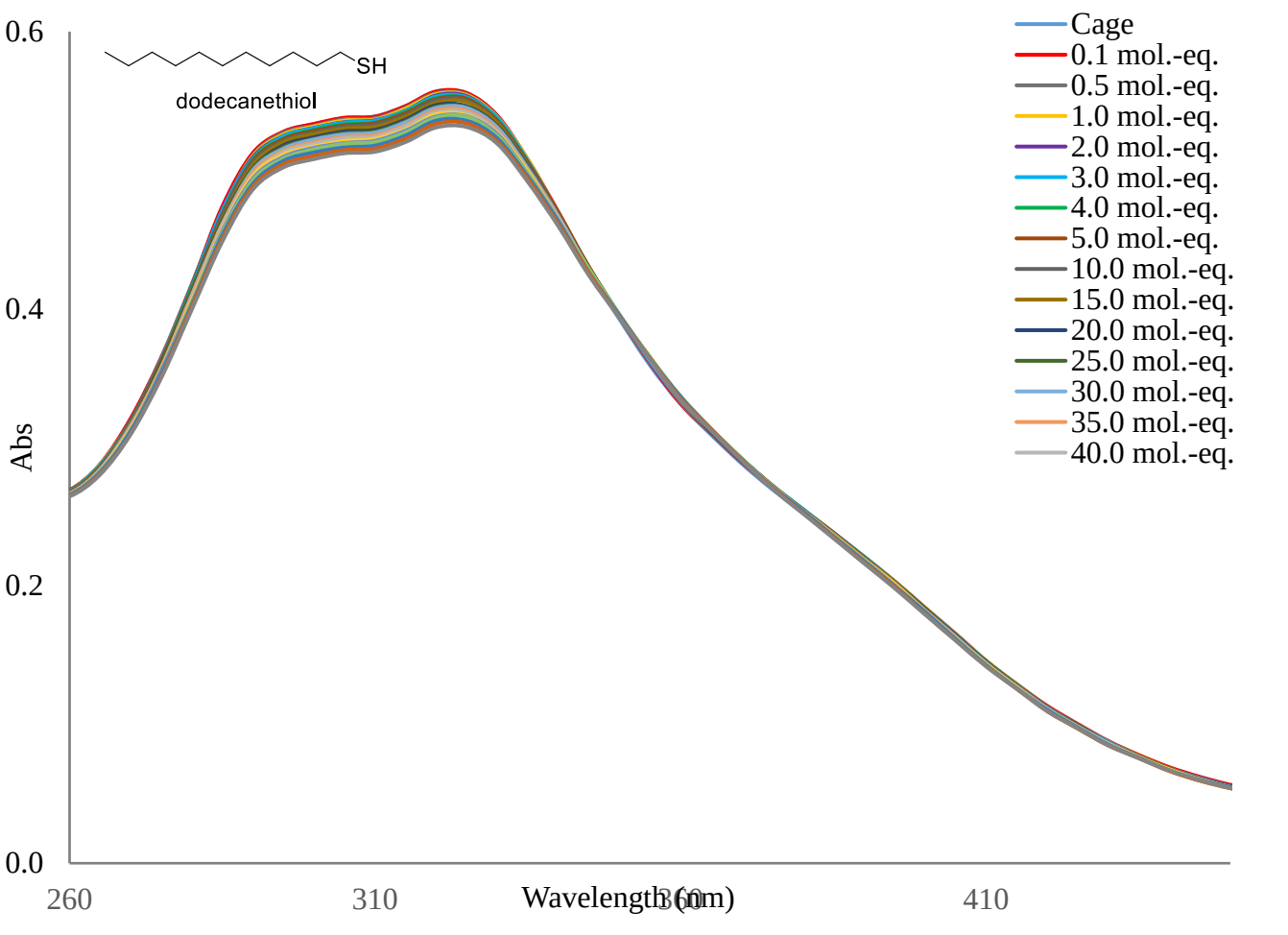

Figure S-29. UV-Vis absorption spectrum of the titration of **C_{12}-SH** into a 3 µM solution of cage **1** in CH_3CN. **C_{12}-SH** was added in 0.1-5 µL aliquots from a 9 mM stock solution in CH_3CN.

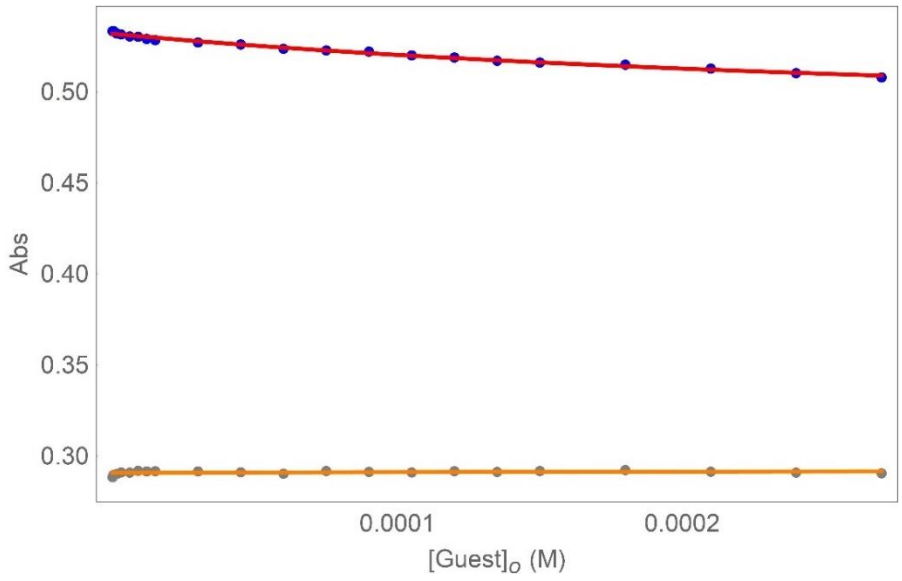

Residuals 330 nm

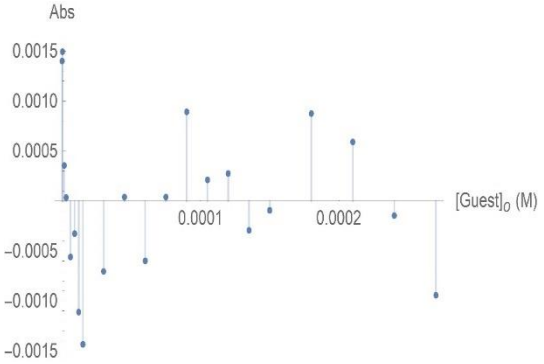

Residuals 370 nm

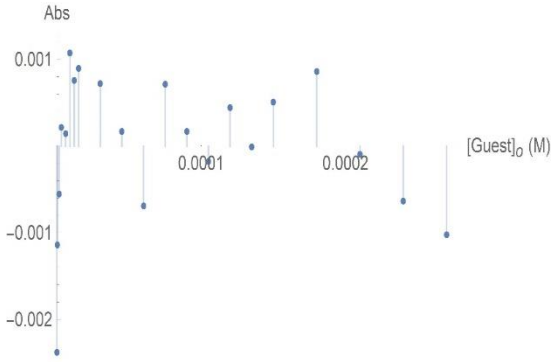

Figure S-30. Fitting curves and plots of residual magnitude obtained when fitting the UV binding data for **C$_{12}$-SH** with cage **1** to the 1:1 binding model.

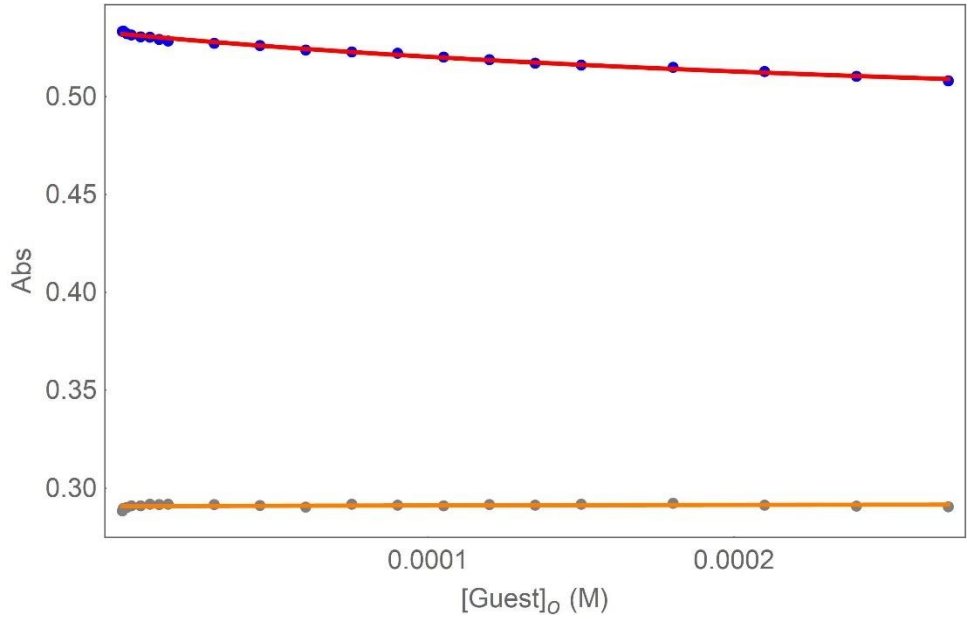

Residuals 330 nm

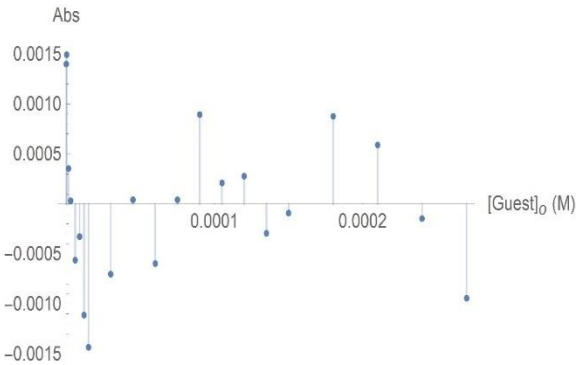

Residuals 370 nm

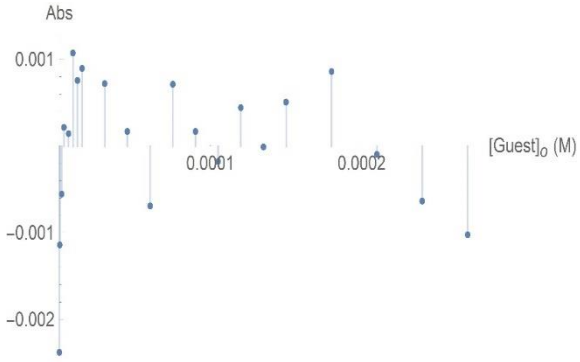

Figure S-31. Fitting curves and plots of residual magnitude obtained when fitting the UV binding data for **C$_{12}$-SH** with cage **1** to the 1:2 binding model.

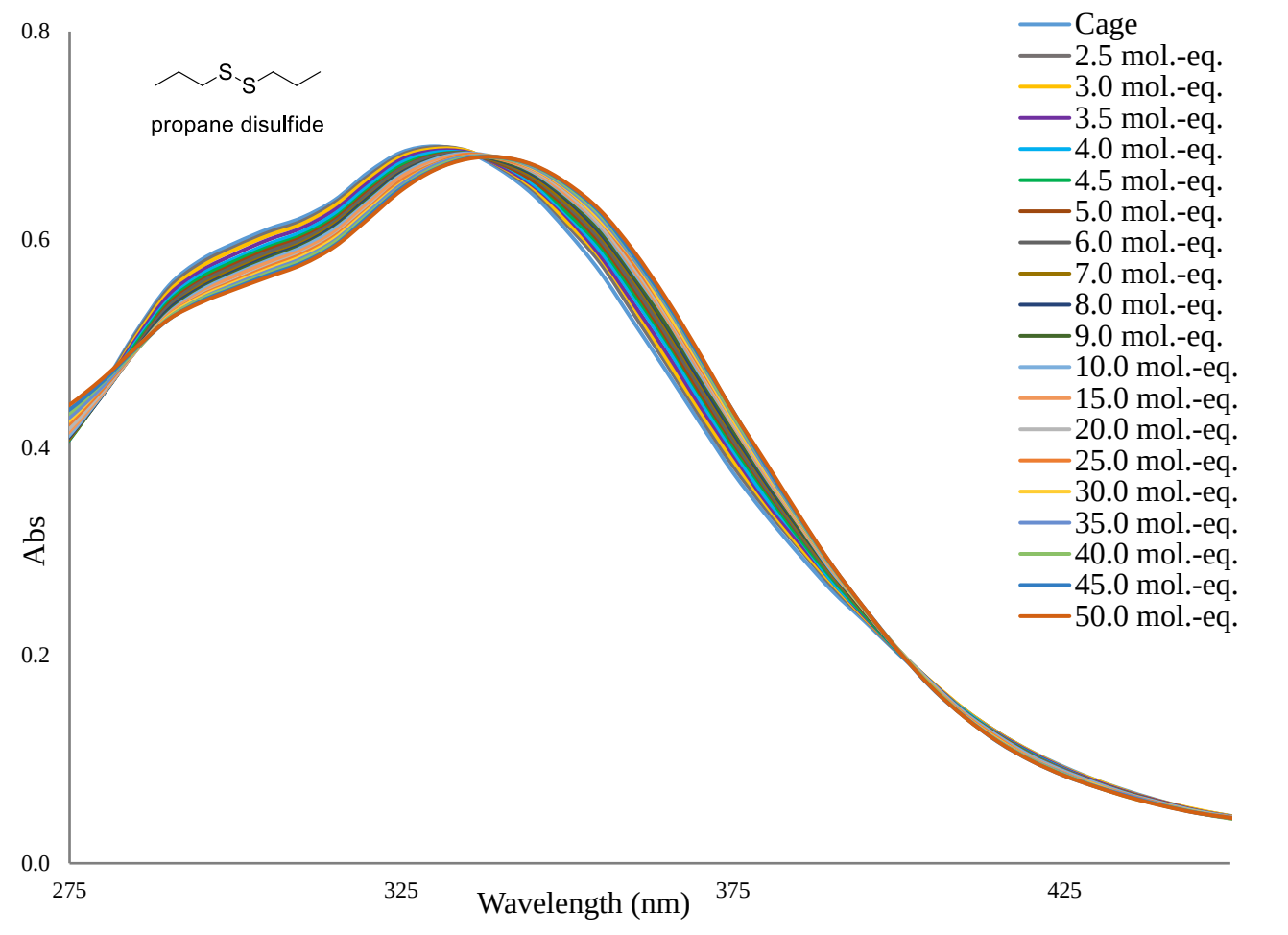

Figure S-32. UV-Vis absorption spectrum of the titration of **$(C_3\text{-}S)_2$** into a 3 µM solution of cage **1** in CH_3CN. **$(C_3\text{-}S)_2$** was added in 2.5-5 µL aliquots from a 9 mM stock solution in CH_3CN.

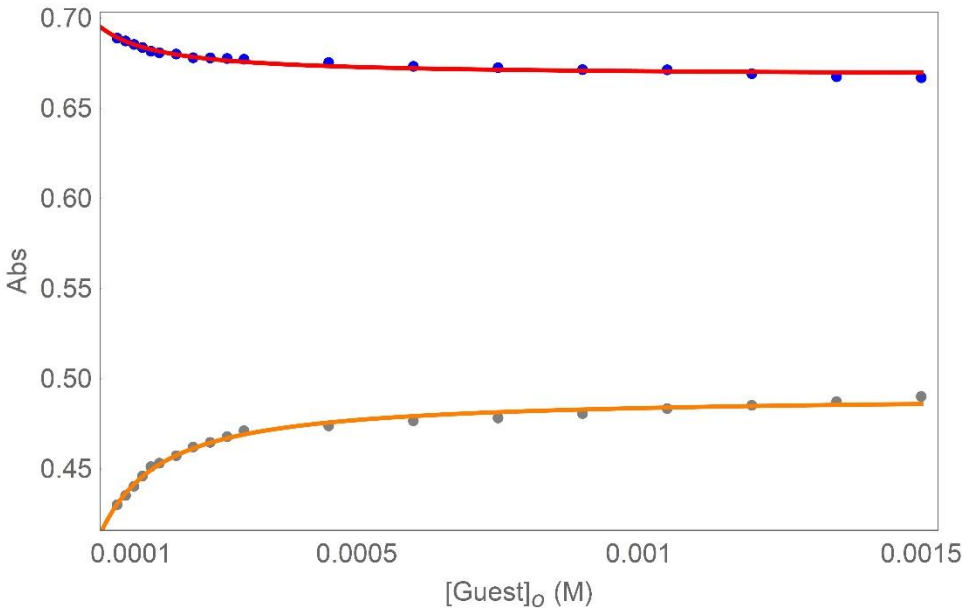

Residuals 330 nm

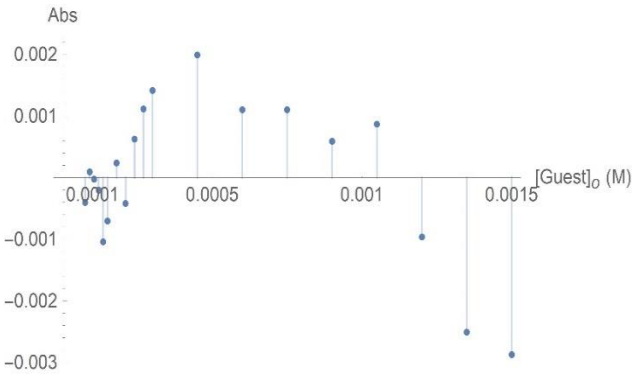

Residuals 370 nm

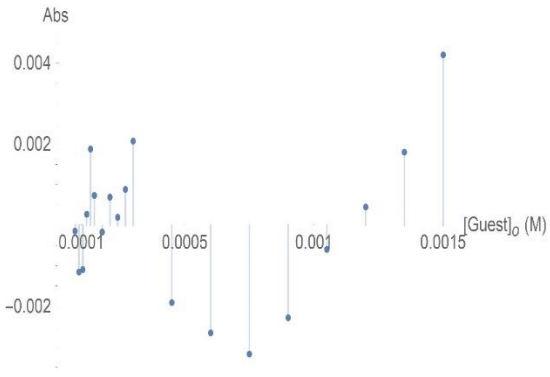

Figure S-33. Fitting curves and plots of residual magnitude obtained when fitting the UV binding data for **(C$_3$-S)$_2$** with cage **1** to the 1:1 binding model.

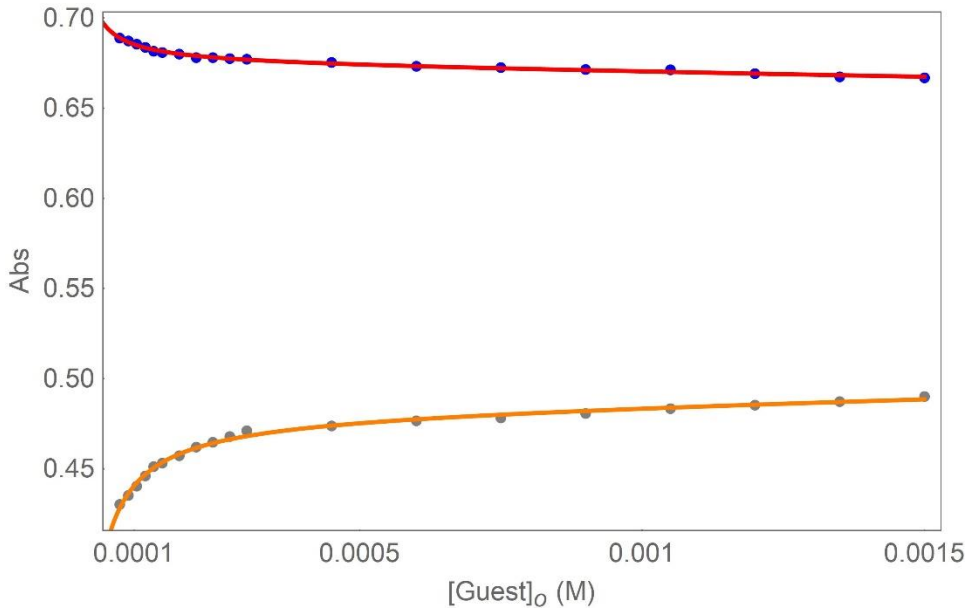

Residuals 330 nm

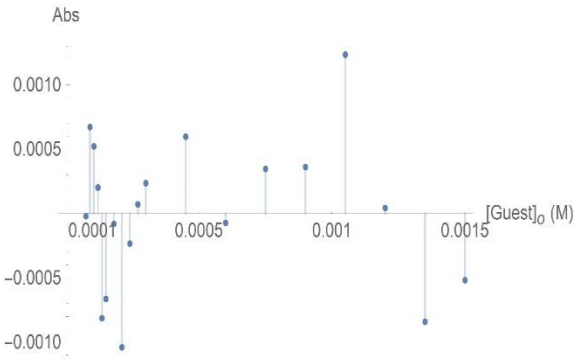

Residuals 370 nm

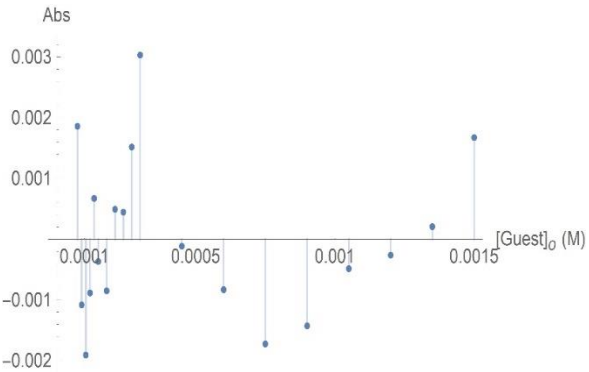

Figure S-34. Fitting curves and plots of residual magnitude obtained when fitting the UV binding data for **(C$_3$-S)$_2$** with cage **1** to the 1:2 binding model.

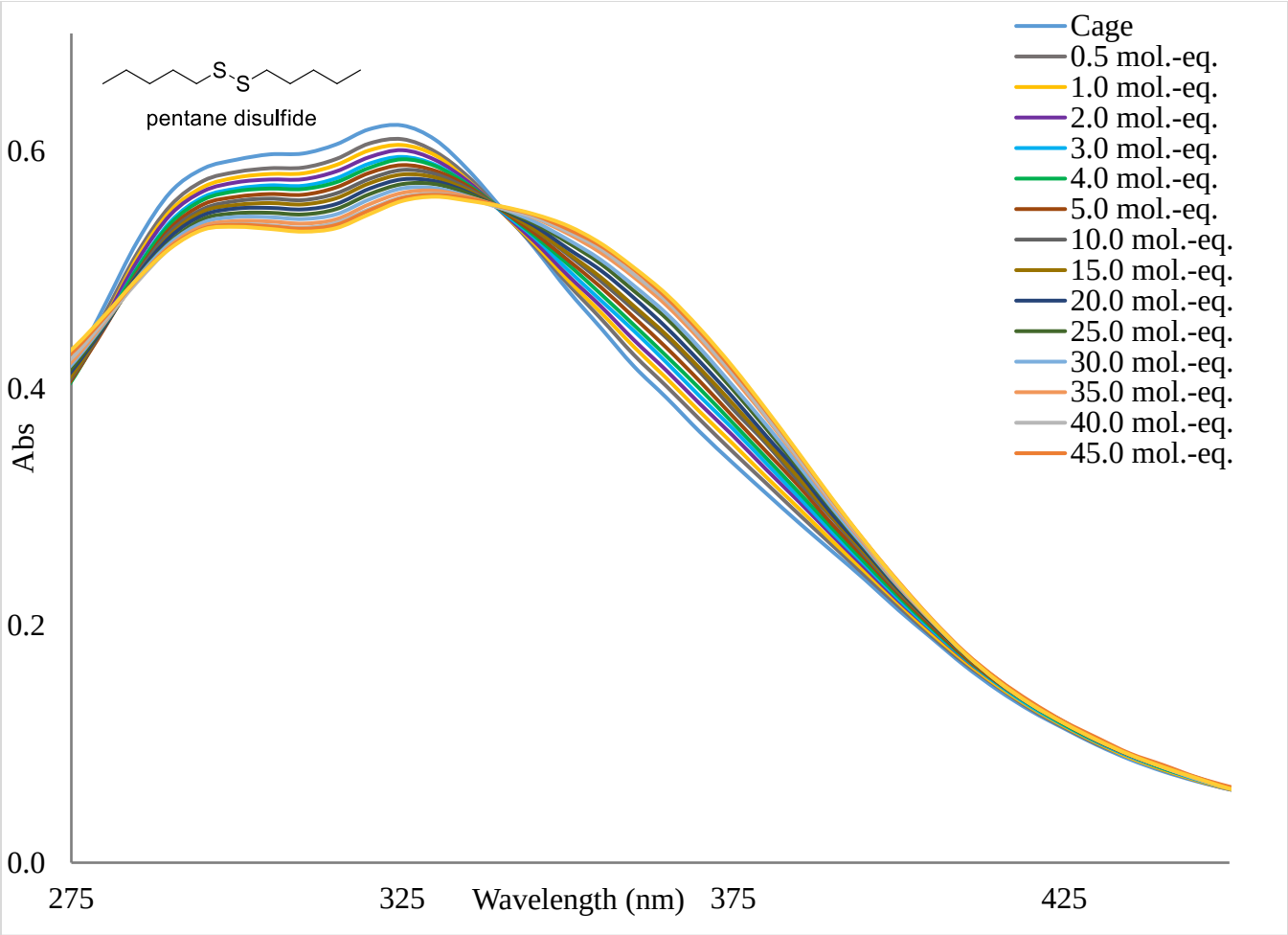

Figure S-35. UV-Vis absorption spectrum of the titration of **$(C_5\text{-}S)_2$** into a 3 µM solution of cage **1** in CH_3CN. **$(C_5\text{-}S)_2$** was added in 0.5-5 µL aliquots from a 9 mM stock solution in CH_3CN.

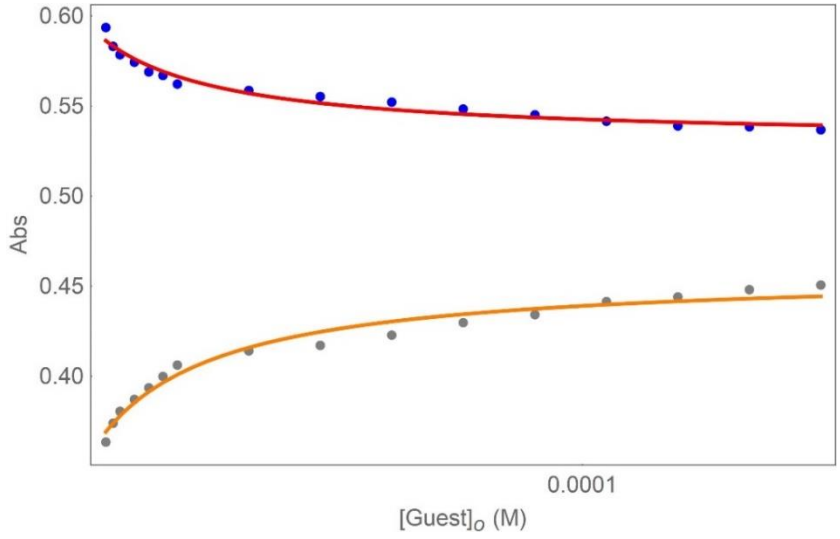

Residuals 330 nm

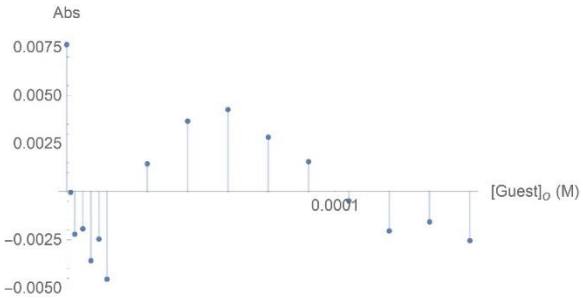

Residuals 370 nm

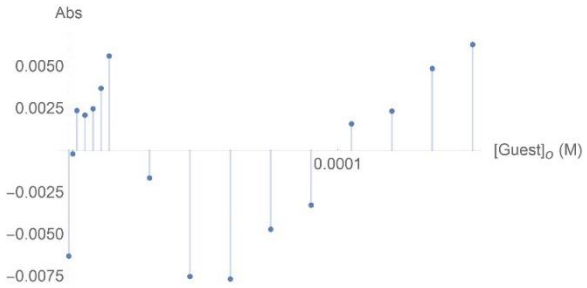

Figure S-36. Fitting curves and plots of residual magnitude obtained when fitting the UV binding data for **(C$_5$-S)$_2$** with cage **1** to the 1:1 binding model.

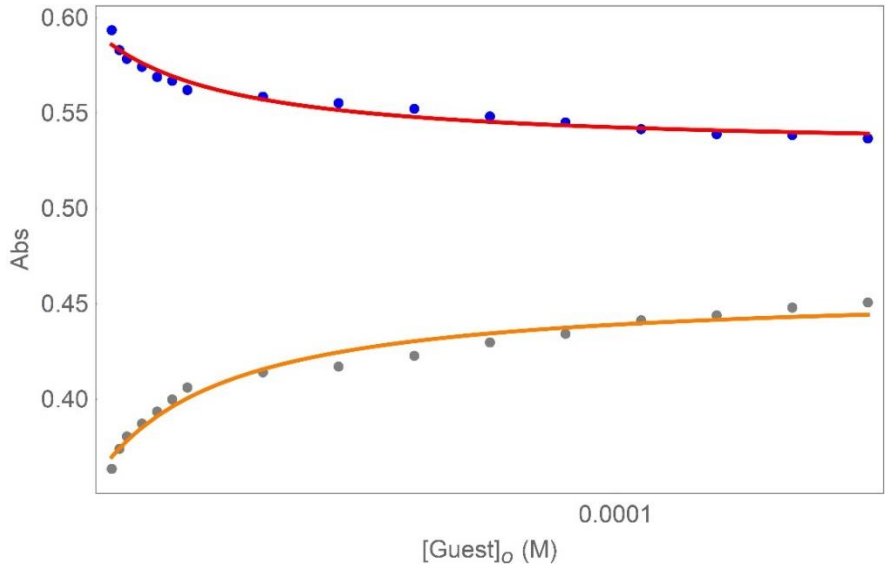

Residuals 330 nm

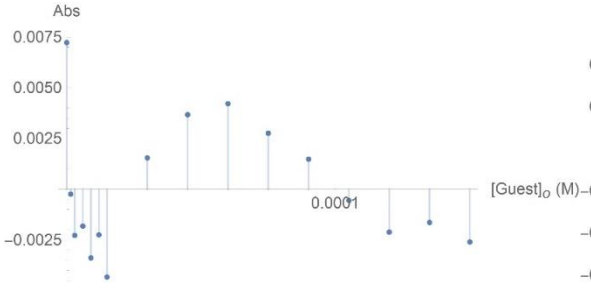

Residuals 370 nm

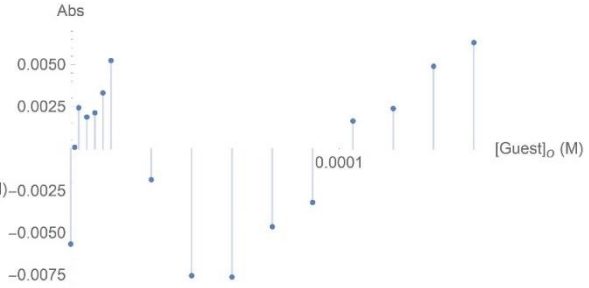

Figure S-37. Fitting curves and plots of residual magnitude obtained when fitting the UV binding data for **(C$_5$-S)$_2$** with cage **1** to the 1:2 binding model.

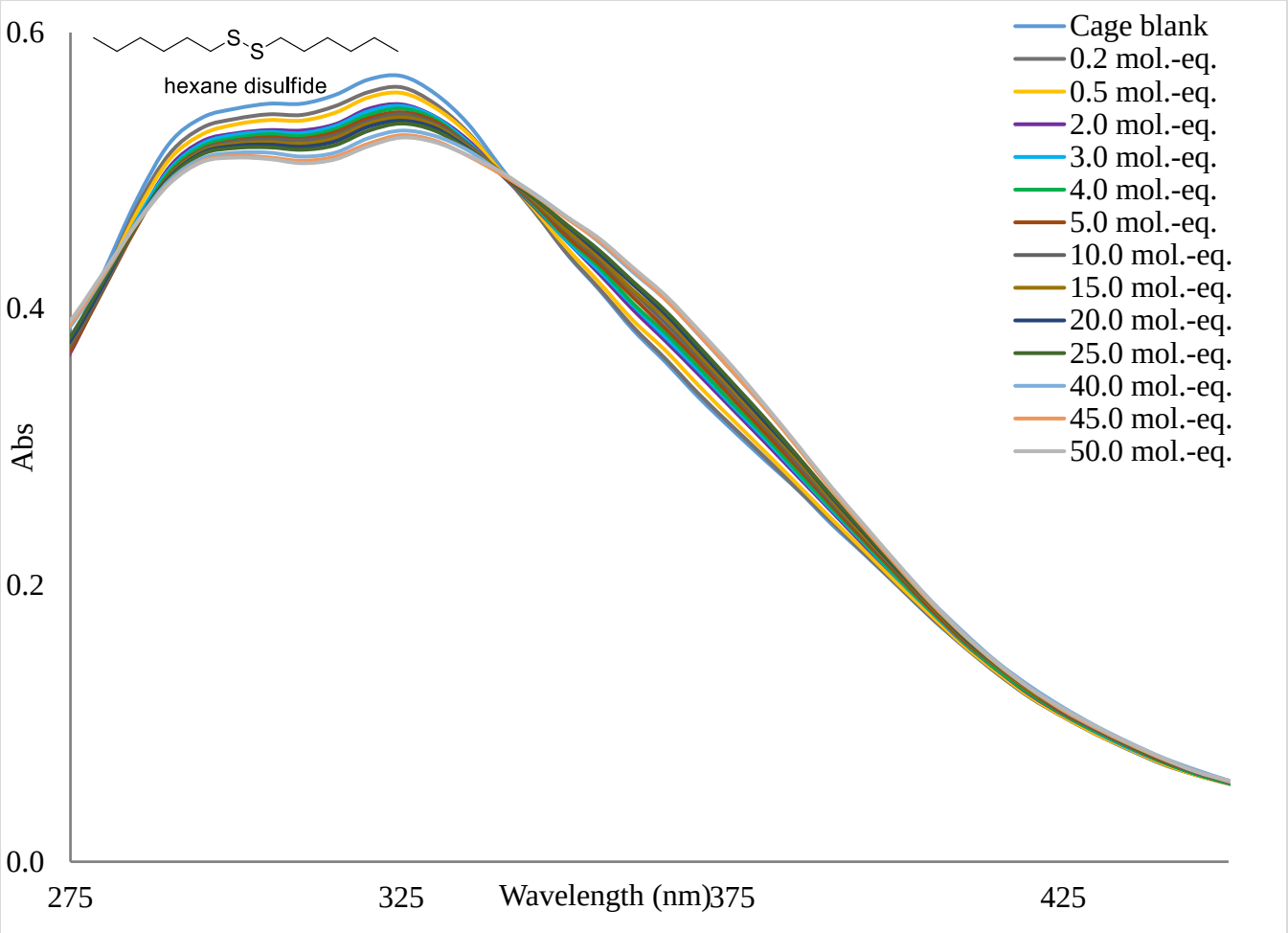

Figure S-38. UV-Vis absorption spectrum of the titration of **$(C_6\text{-}S)_2$** into a 3 µM solution of cage **1** in CH_3CN. **$(C_6\text{-}S)_2$** was added in 0.5-5 µL aliquots from a 9 mM stock solution in CH_3CN.

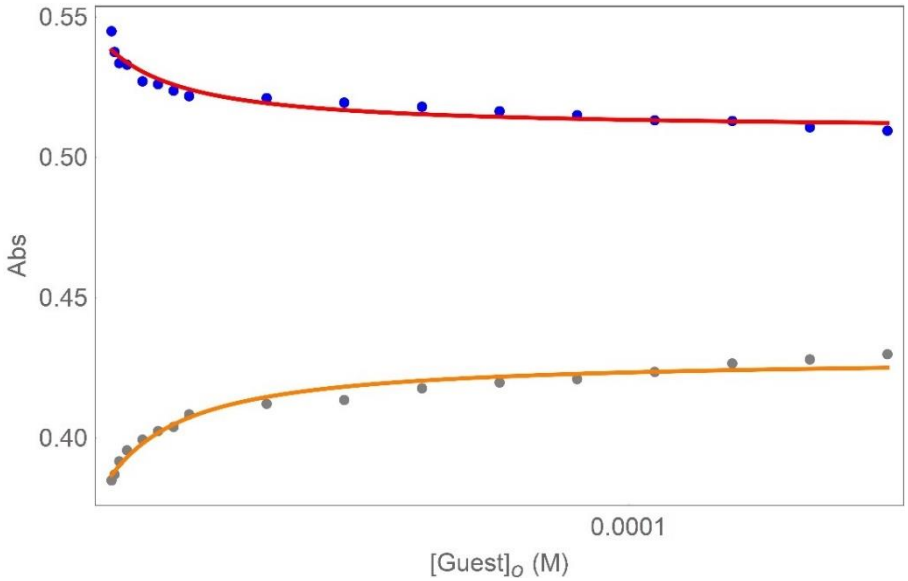

Residuals 330 nm

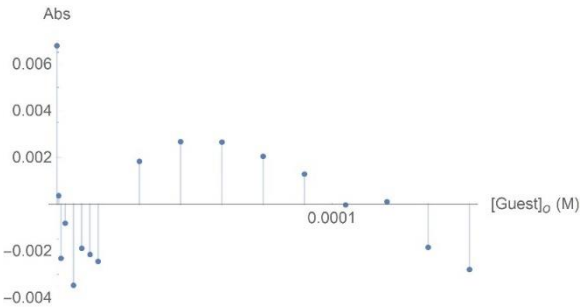

Residuals 370 nm

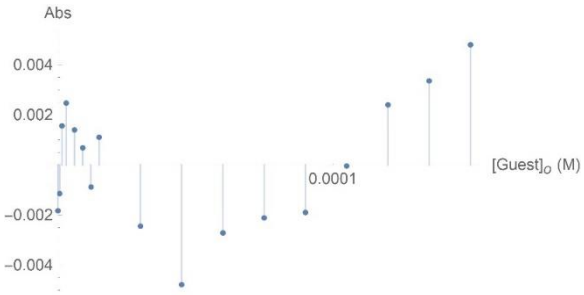

Figure S-39. Fitting curves and plots of residual magnitude obtained when fitting the UV binding data for **(C$_6$-S)$_2$** with cage **1** to the 1:1 binding model.

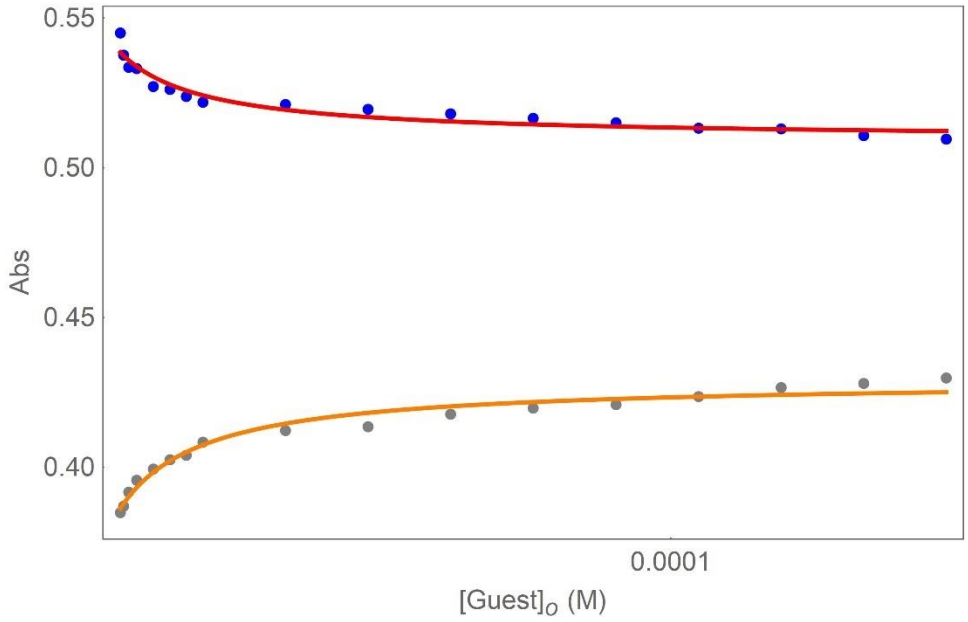

Residuals 330 nm

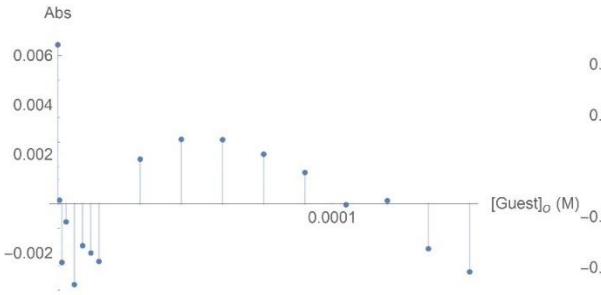

Residuals 370 nm

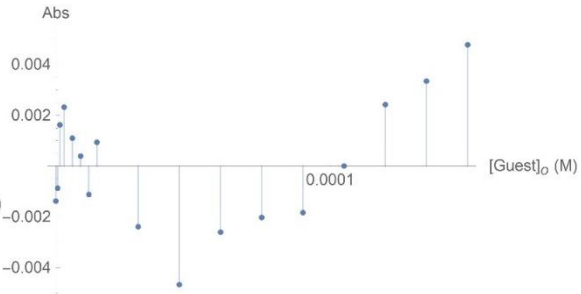

Figure S-40. Fitting curves and plots of residual magnitude obtained when fitting the UV binding data for **(C$_6$-S)$_2$** with cage **1** to the 1:2 binding model.

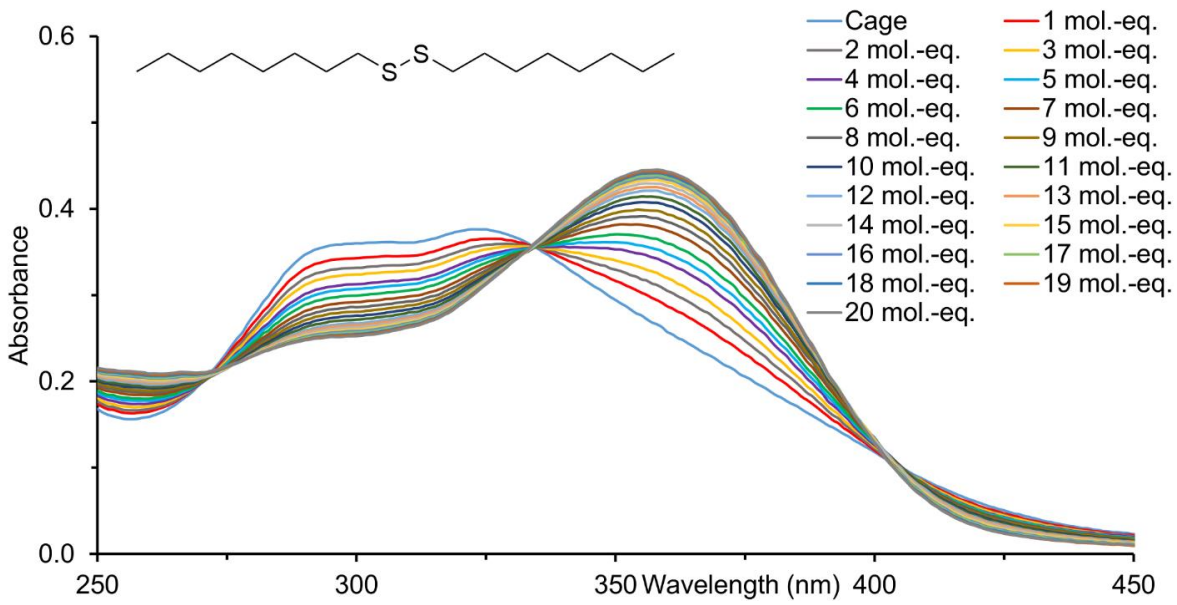

Figure S-41. UV-Vis absorption spectrum of the titration of **$(C_8\text{-}S)_2$** into a 1.5 µM solution of cage **1** in CH_3CN. **$(C_8\text{-}S)_2$** was added in 1-5 µL aliquots from a 4.5 mM stock solution in CH_3CN.

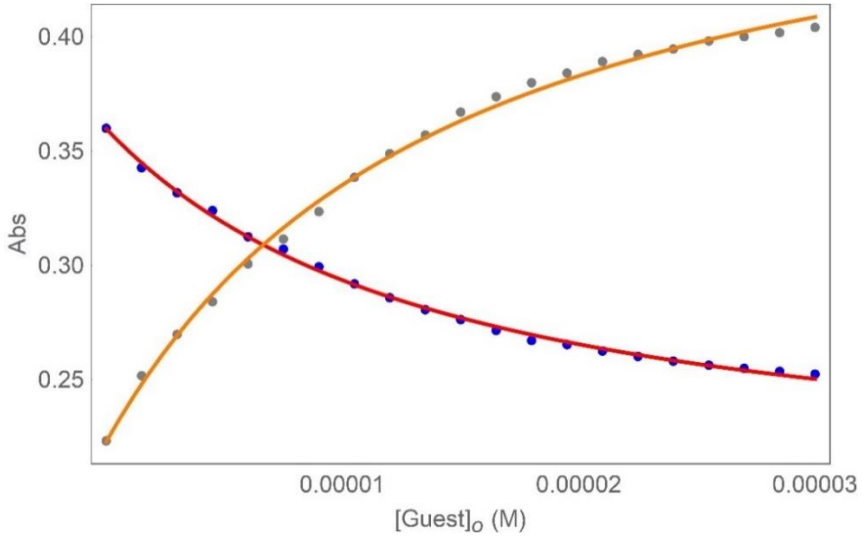

Residuals 330 nm

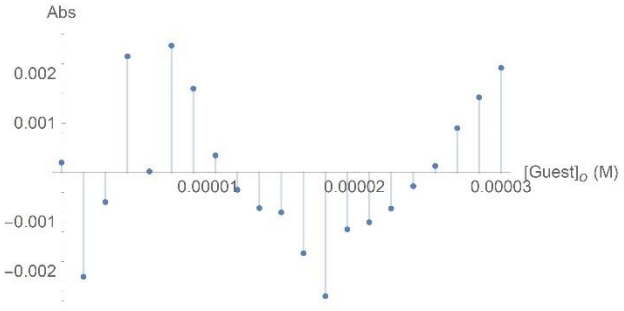

Residuals 370 nm

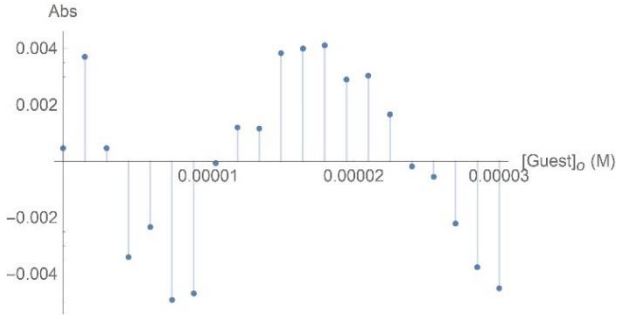

Figure S-42. Fitting curves and plots of residual magnitude obtained when fitting the UV binding data for **$(C_8\text{-}S)_2$** with cage **1** to the 1:1 binding model.

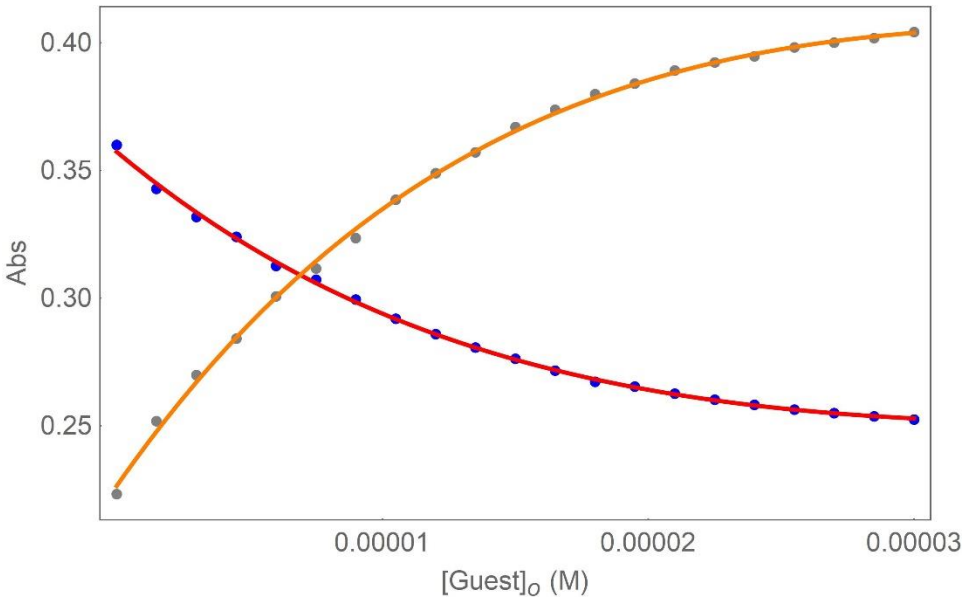

Residuals 330 nm

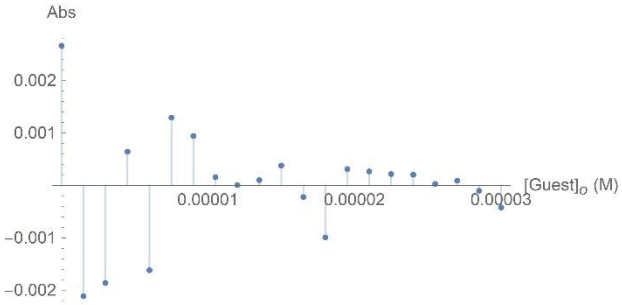

Residuals 370 nm

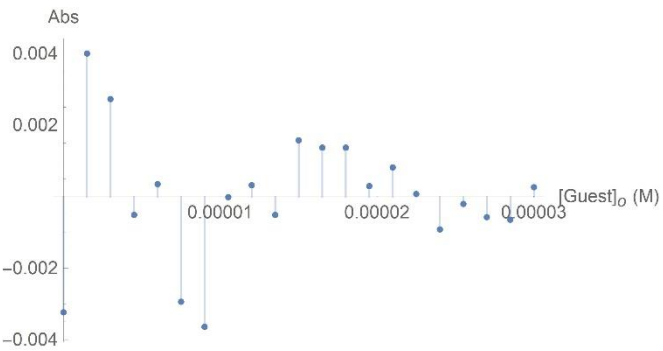

Figure S-43. Fitting curves and plots of residual magnitude obtained when fitting the UV binding data for **(C$_8$-S)$_2$** with cage **1** to the 1:2 binding model.

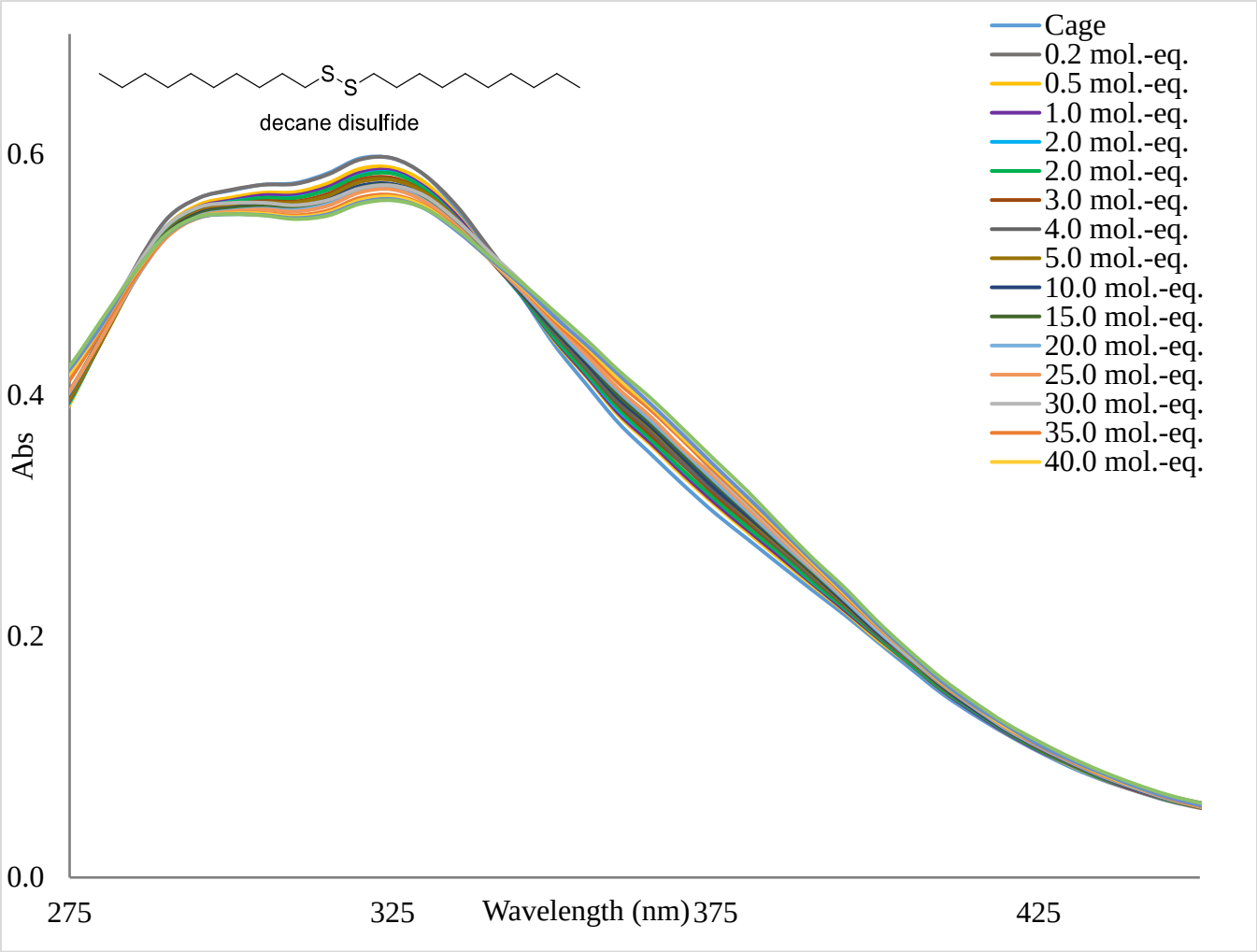

Figure S-44. UV-Vis absorption spectrum of the titration of **$(C_{10}\text{-}S)_2$** into a 3 µM solution of cage **1** in CH_3CN. **$(C_{10}\text{-}S)_2$** was added in 0.2-5 µL aliquots from a 9 mM stock solution in CH_3CN.

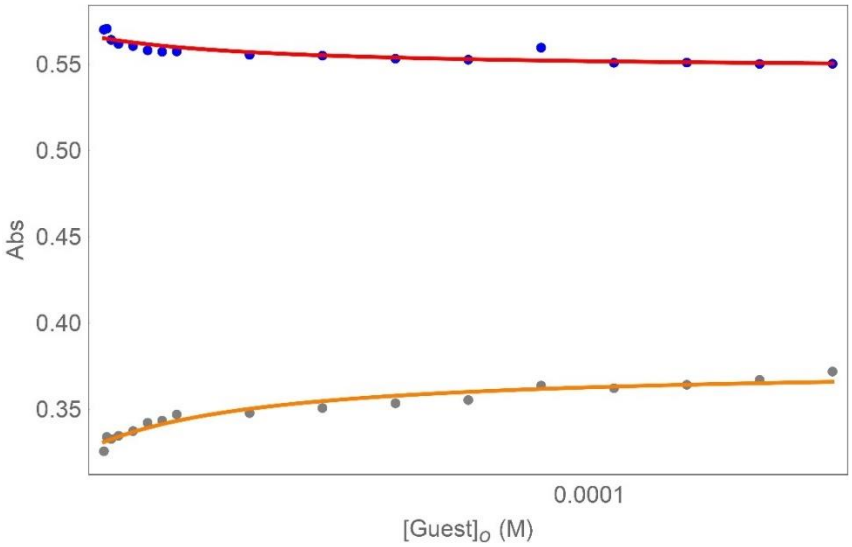

Residuals 300 nm

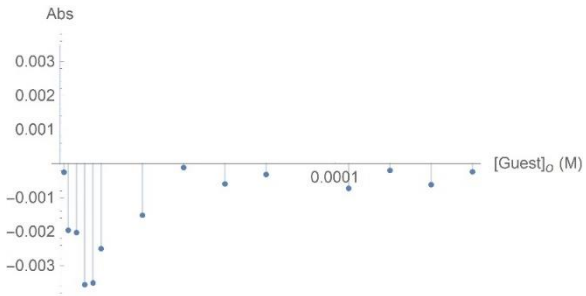

Residuals 370 nm

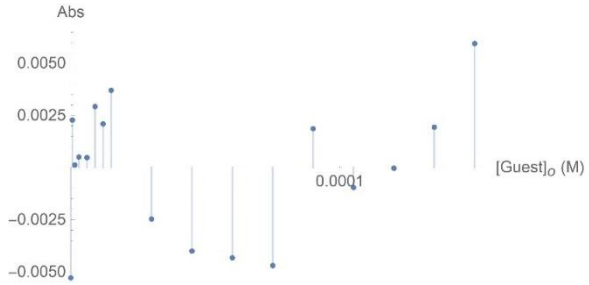

Figure S-45. Fitting curves and plots of residual magnitude obtained when fitting the UV binding data for **(C$_{10}$-S)$_2$** with cage **1** to the 1:1 binding model.

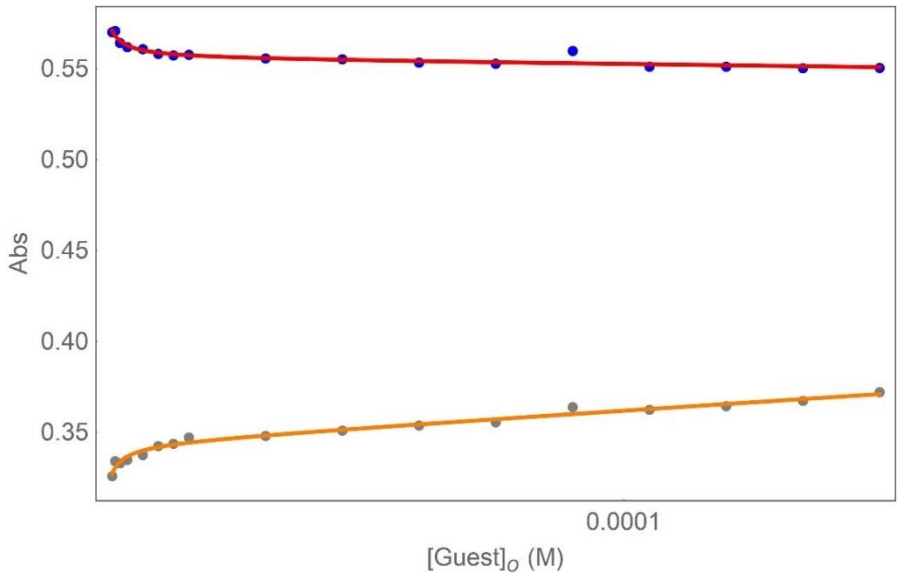

Residuals 300 nm

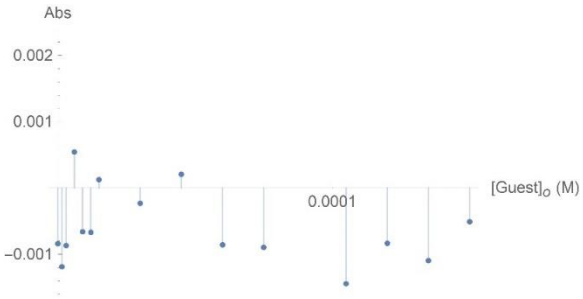

Residuals 370 nm

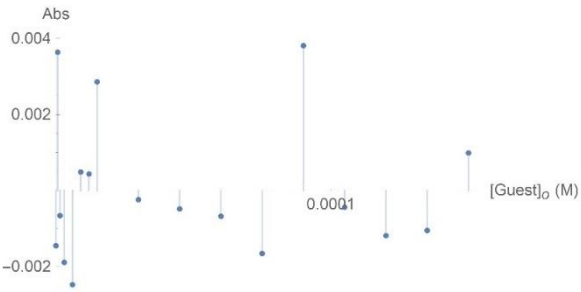

Figure S-46. Fitting curves and plots of residual magnitude obtained when fitting the UV binding data for **(C$_{10}$-S)$_2$** with cage **1** to the 1:2 binding model.

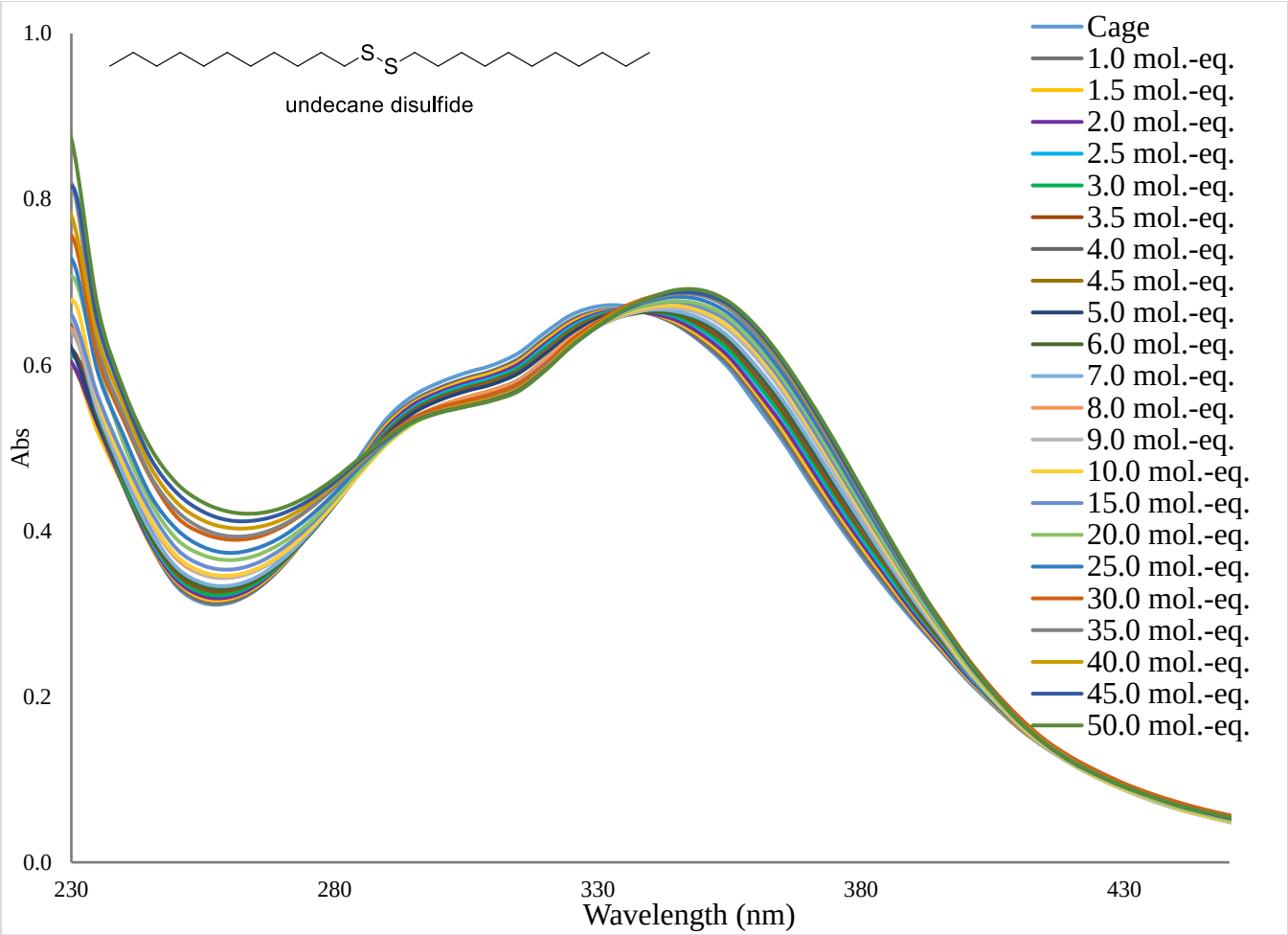

Figure S-47. UV-Vis absorption spectrum of the titration of **$(C_{10}\text{-}S)_2$** into a 3 µM solution of cage **1** in CH_3CN. **$(C_{11}\text{-}S)_2$** was added in 1-5 µL aliquots from a 9 mM stock solution in CH_3CN.

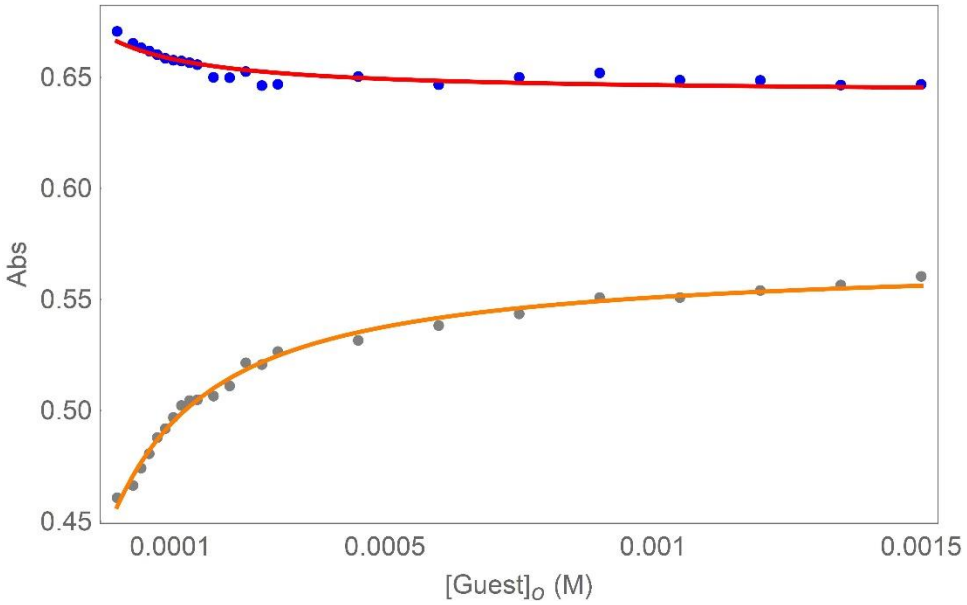

Residuals 330 nm

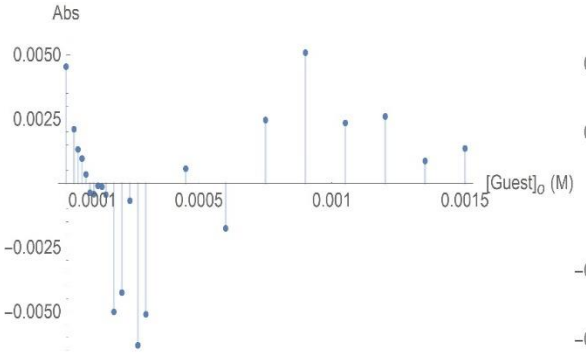

Residuals 370 nm

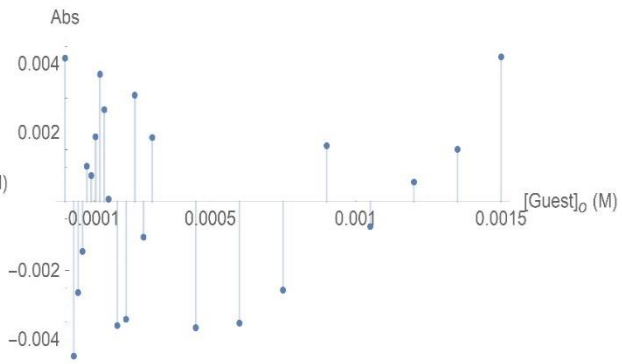

Figure S-48. Fitting curves and plots of residual magnitude obtained when fitting the UV binding data for **(C$_{11}$-S)$_2$** with cage **1** to the 1:1 binding model.

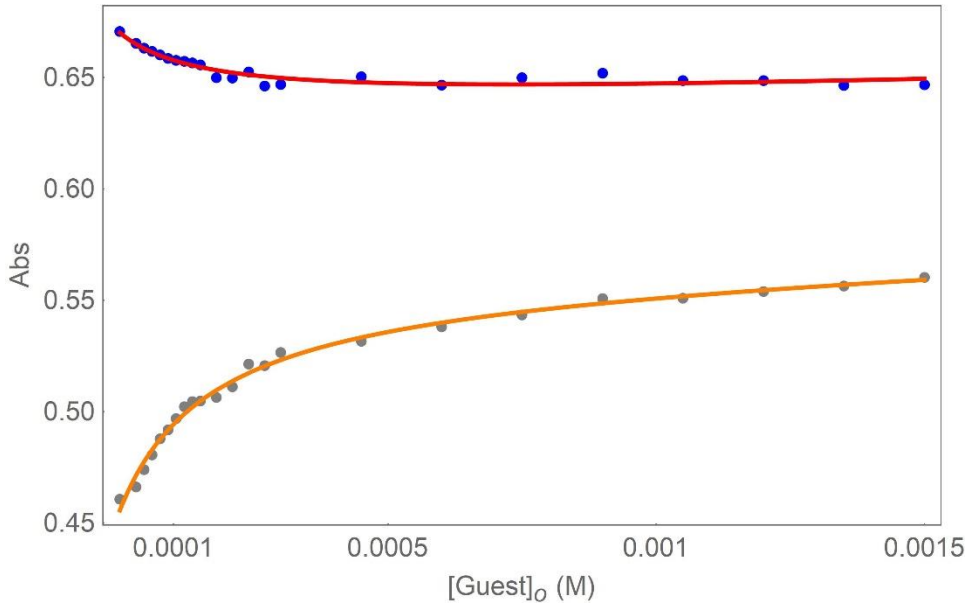

Residuals 330 nm

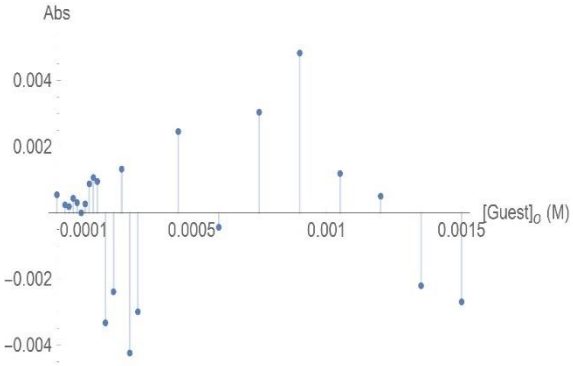

Residuals 370 nm

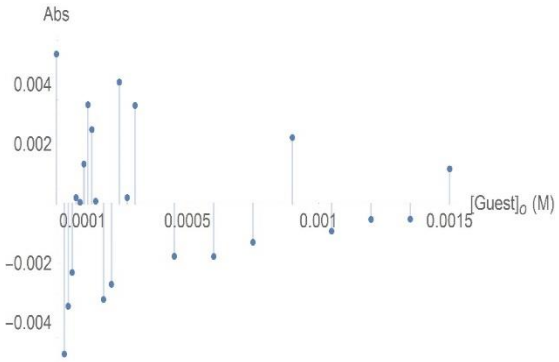

Figure S-49. Fitting curves and plots of residual magnitude obtained when fitting the UV binding data for **(C$_{11}$-S)$_2$** with cage **1** to the 1:2 binding model.

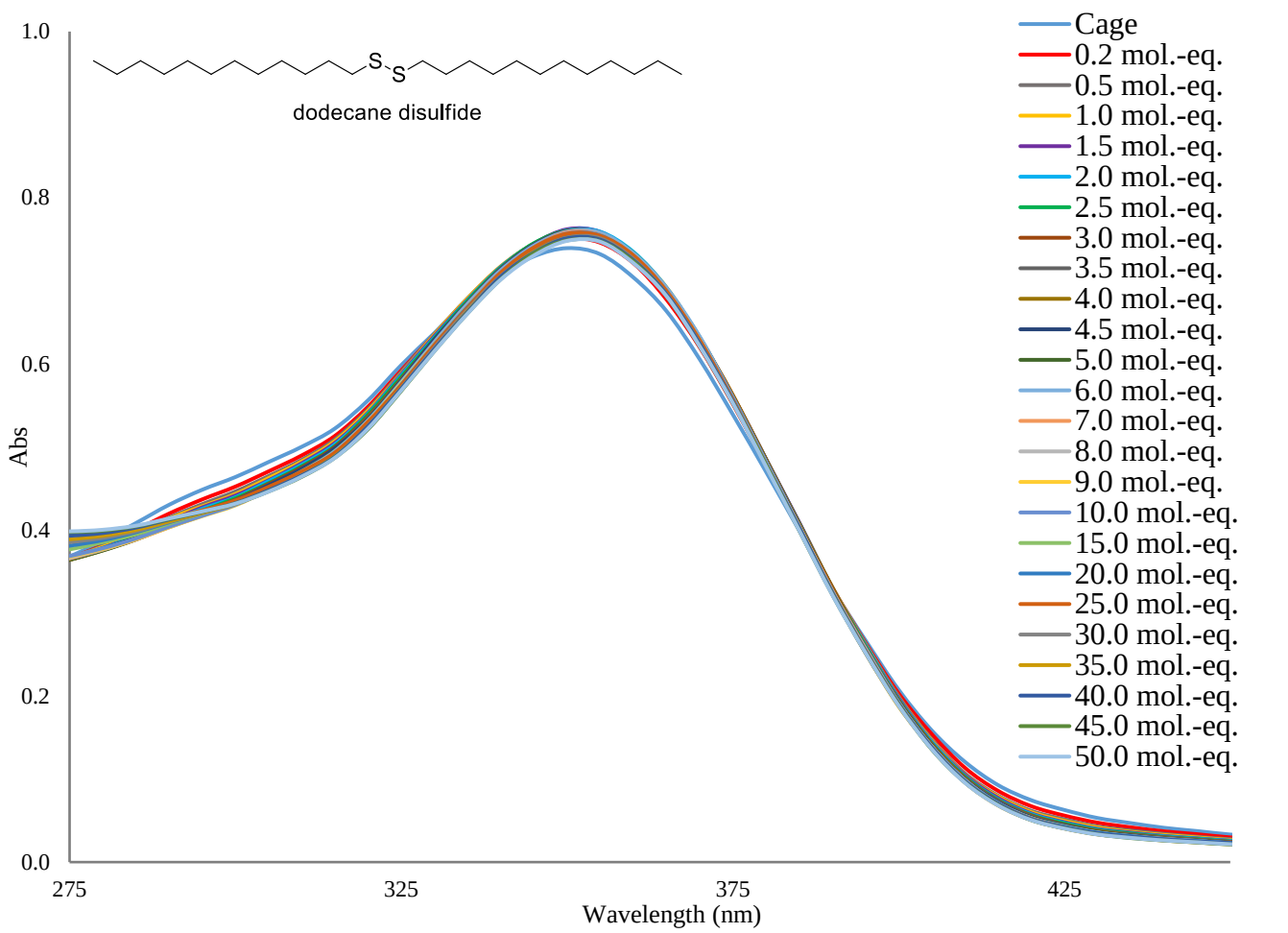

Figure S-50. UV-Vis absorption spectrum of the titration of **$(C_{10}\text{-}S)_2$** into a 3 µM solution of cage **1** in CH_3CN. **$(C_{12}\text{-}S)_2$** was added in 1-5 µL aliquots from a 9 mM stock solution in CH_3CN.

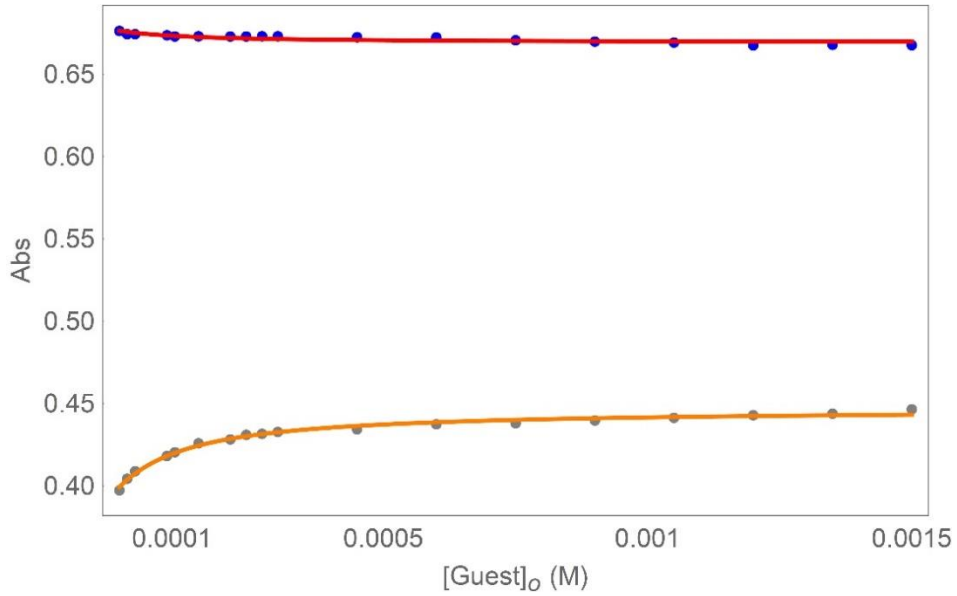

Residuals 330 nm

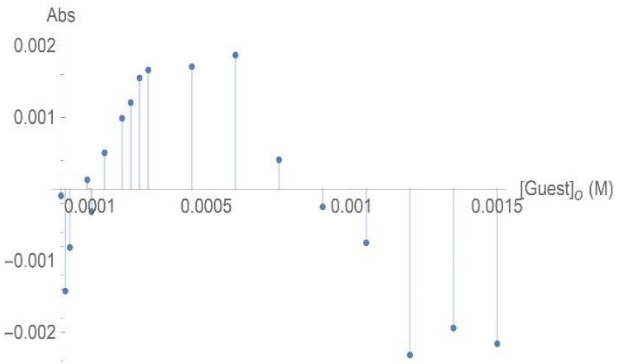

Residuals 370 nm

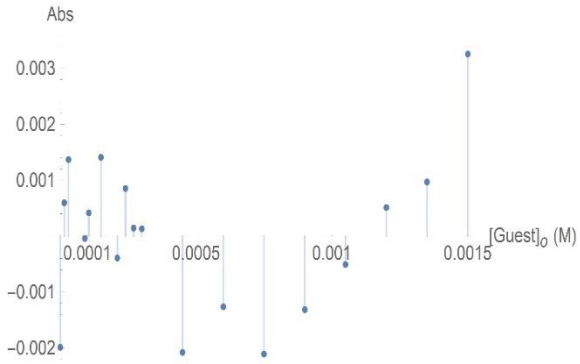

Figure S-51. Fitting curves and plots of residual magnitude obtained when fitting the UV binding data for **(C12-S)2** with cage **1** to the 1:1 binding model.

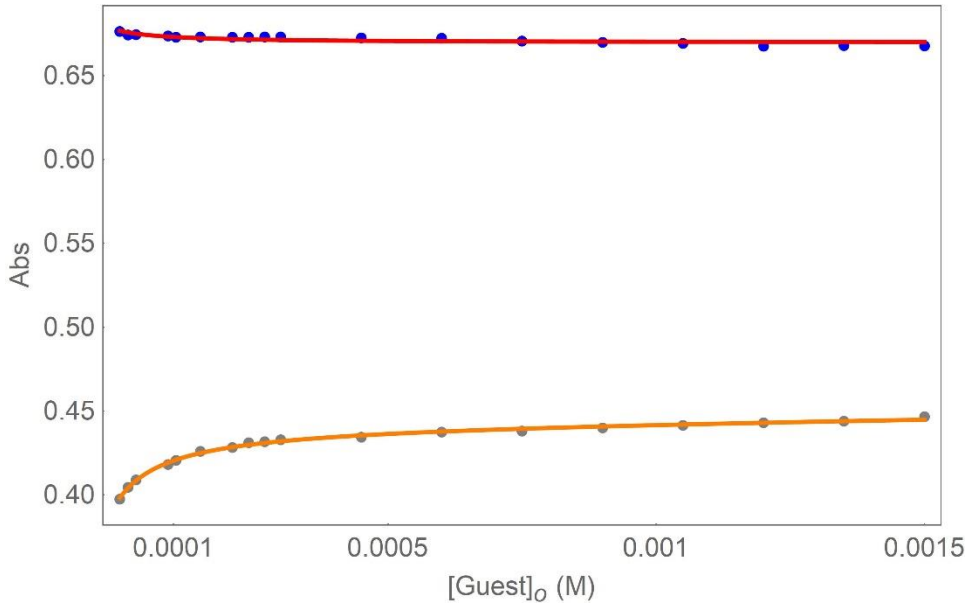

Residuals 330 nm

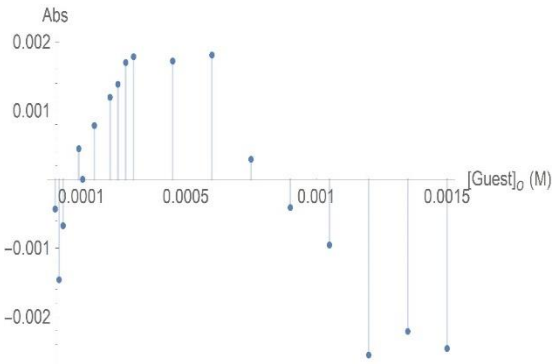

Residuals 370 nm

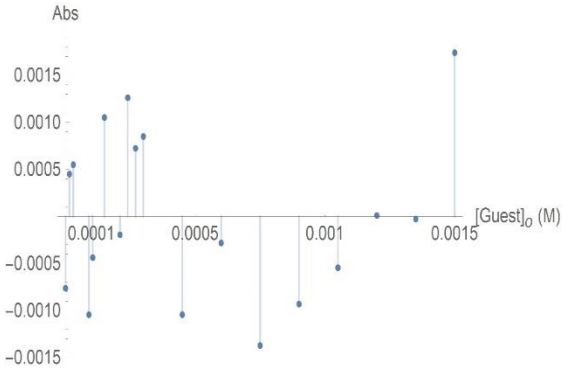

Figure S-52. Fitting curves and plots of residual magnitude obtained when fitting the UV binding data for **(C12-S)2** with cage **1** to the 1:2 binding model.

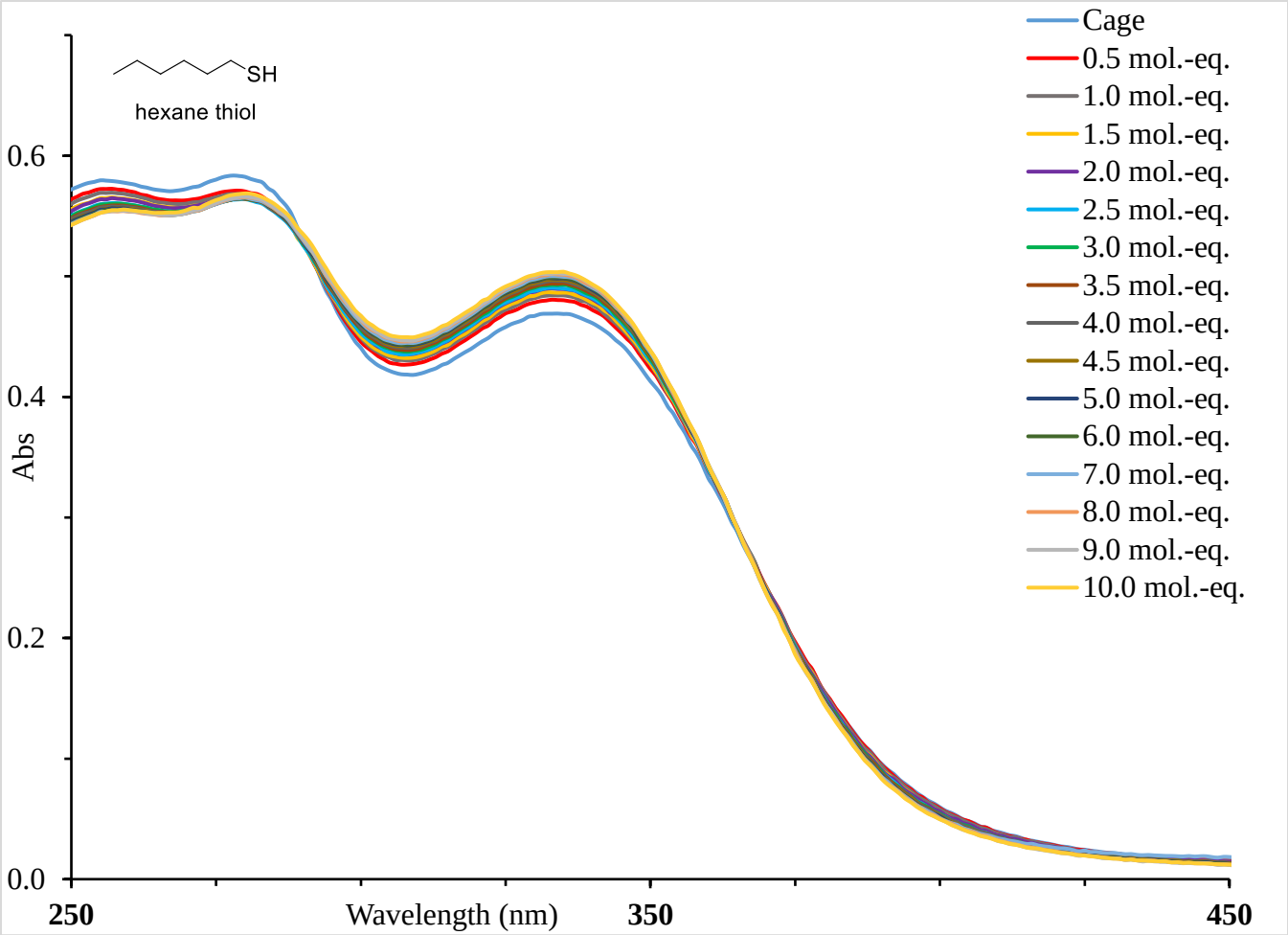

Figure S-53. UV-Vis absorption spectrum of the titrationn of **C_6-SH** into a 3 µM solution of cage **2** in CH_3CN. **C_6-SH** was added in 0.5-1 µL aliquots from a 9 mM stock solution in CH_3CN.

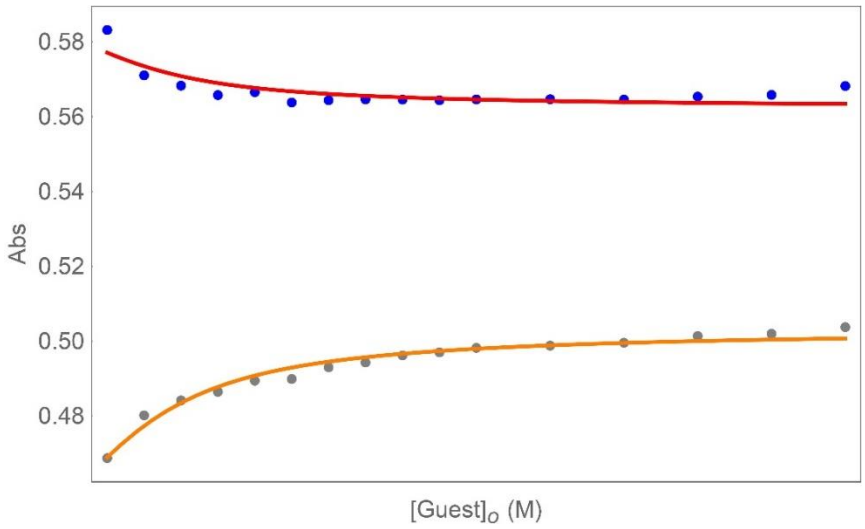

Residuals 278 nm

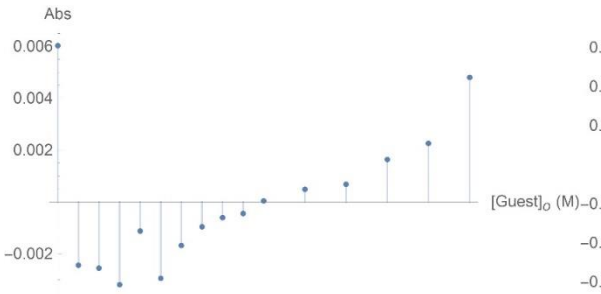

Residuals 335 nm

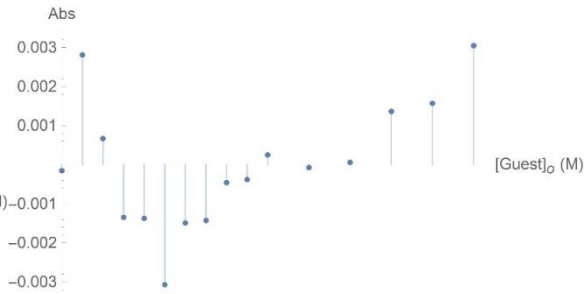

Figure S-54. Fitting curves and plots of residual magnitude obtained when fitting the UV binding data for **C$_6$-SH** with cage **2** to the 1:1 binding model.

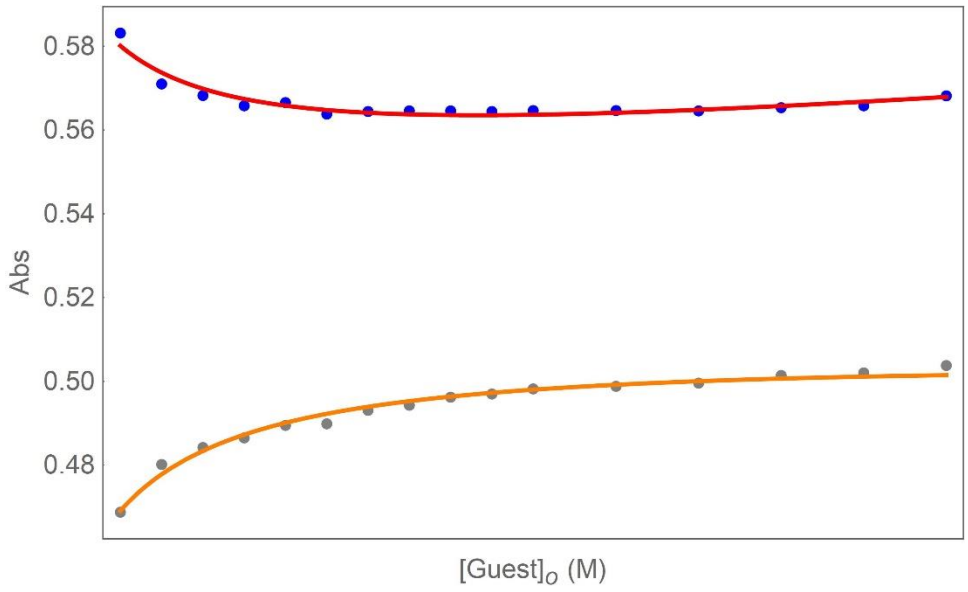

Residuals 278 nm

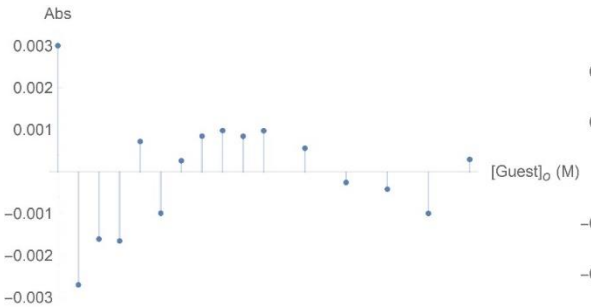

Residuals 335 nm

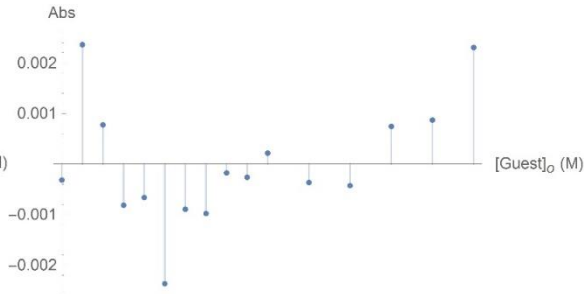

Figure S-55. Fitting curves and plots of residual magnitude obtained when fitting the UV binding data for **C$_6$-SH** with cage **2** to the 1:2 binding model.

b. Fitting Analysis and Affinity Constants

Table S-1. Calculated Binding Affinities for Guests in Host **1** or **2**, showing only results from the model showing Best Fit (p-value < 0.001, **Sig = Yes**).

	1:1 model	**1:2 Model**			**1:1 vs 1:2**
Substrate	**K_a** (x 10^3 M^{-1})	**K_1** (x 10^3 M^{-1})	**K_2** (x 10^3 M^{-1})	**4 K_2/K_1**	**p-value, Sig**
*Pentane Thiol (**1**)*		2150 ± 650	1.2 ± 3.0	**8.7×10^{-4}**	**10^{-4}, Yes**
*Hexane Thiol (**1**)*		540 ± 130	2.4 ± 1.5	**0.018**	**10^{-6}, Yes**
*Octane Thiol (**1**)*		174 ± 43	0.78 ± 0.53	**0.018**	**10^{-7}, Yes**
*Decane Thiol (**1**)*	19.7 ± 6.4				0.02, No
*Undecane Thiol (**1**)*	40.± 19				0.004, No
*Dodecane Thiol (**1**)*	2.74± 0.60				0.40, No
*Propyl Disulfide (**1**)*	16.6 ± 2.4				0.019, No
*Pentyl Disulfide (**1**)*	38.8 ± 7.1				0.43, No
*Hexyl Disulfide (**1**)*	71 ± 14				0.46, No
*Octyl Disulfide (**1**)*	76.1 ± 3.8				0.006, No
*Decyl Disulfide (**1**)*	27.9 ± 9.4				0.01, No
*Undecyl Disulfide (**1**)*	5.53 ± 0.48				0.19, No
*Dodecyl Disulfide (**1**)*	8.39 ± 0.85				0.36, No
*Hexane Thiol (**2**)*	420 ± 130				0.01, No

V. MS and Structural Data for Cage 1[1a] Illustrating Fragmentation.

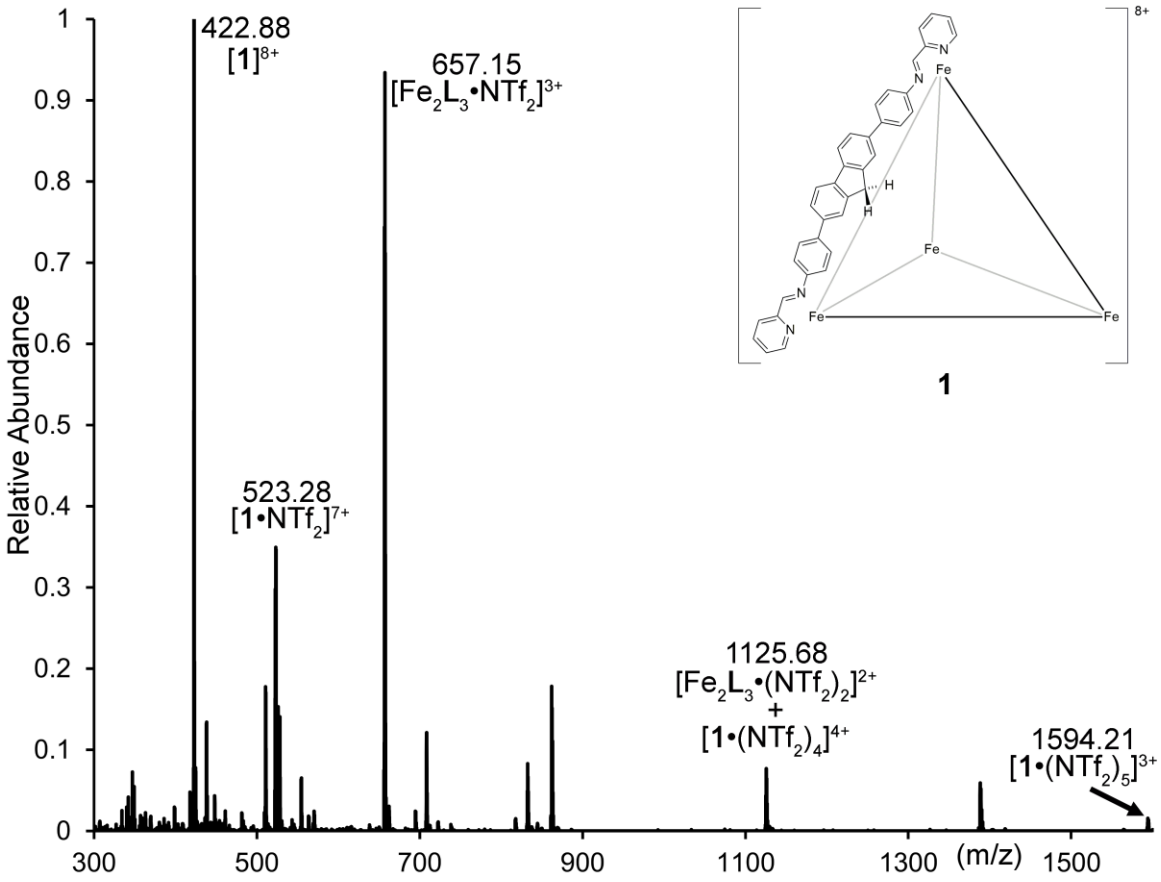

Figure S-56. Full Mass Spectrum of fluorene cage **1** (CH_3CN).[1a] The Fe_2L_3 peak at *m/z* 657 is a fragment of cage **1** under the ionization conditions, and is not seen in solution or the solid state (from 2D DOSY analysis[1a]).

Table S-2. Assigned ions for experimentally observed peaks (**L** = full iminopyridine ligand).

Ion	Charge	Observed (m/z)	Predicted (m/z)
[**1**]	8+	422.88	422.89
[**C**•Py+1H]	1+	438.21	438.20
[Fe_3**L**$_4$•NTf_2]	5+	510.73	510.72
[**1**•NTf_2]	7+	523.29	523.28
[**S-2**•NTf_2]	3+	657.15	657.16
[Fe_3**L**$_4$•2NTf_2]	4+	708.39	708.39
[Fe_2**L**$_4$•NTf_2]	3+	823.57	832.55
[Fe_2**L**$_2$•2NTf_2]	2+	862.09	862.07
[**1**•4NTf_2]	4+	1125.68	1125.68
[**S-2**•2NTf_2]	2+	1125.68	1125.68
[Fe**L**$_2$•NTf_2]	1+	1388.30	1388.28
[**1**•5NTf_2]	3+	1594.25	1594.21

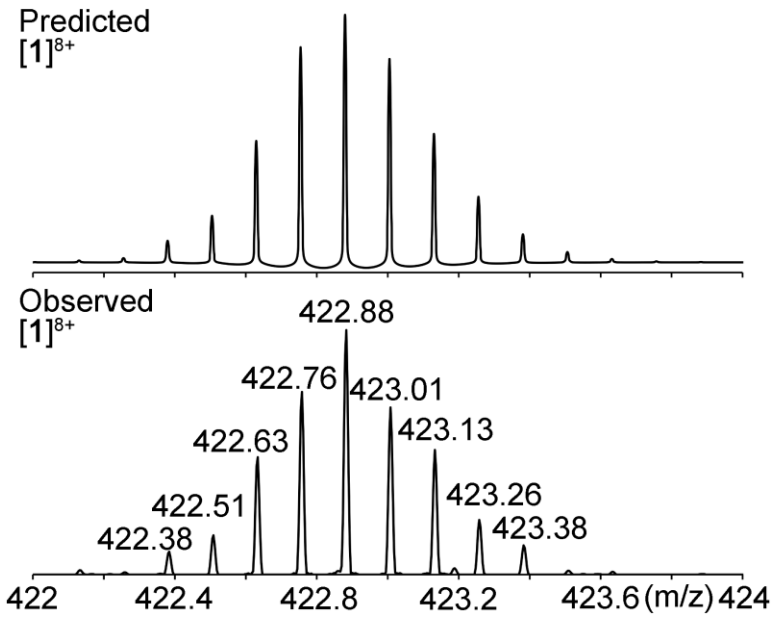

Figure S-57. Stacked comparison of predicted ion [**1**]$^{8+}$ versus experimentally observed peaks.

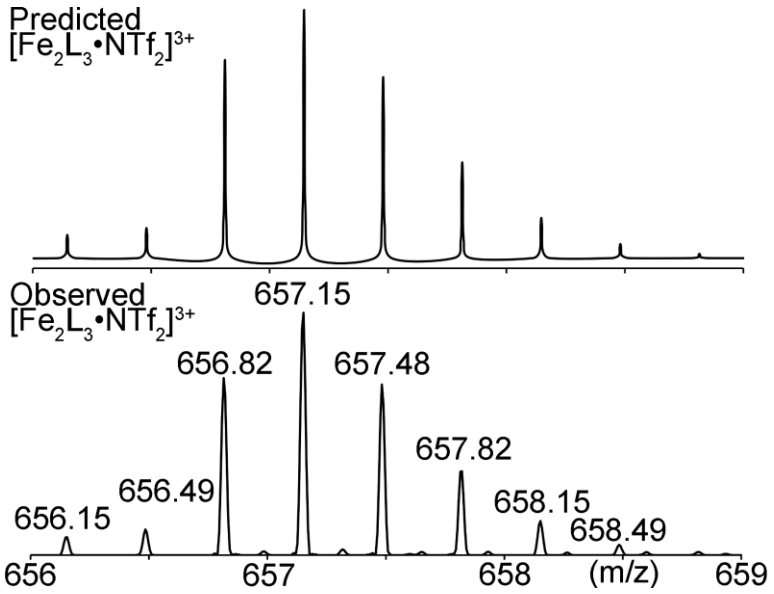

Figure S-58. Stacked comparison of predicted ion [**Fe$_2$L$_3$**•NTf$_2$]$^{3+}$ versus experimentally observed peaks.

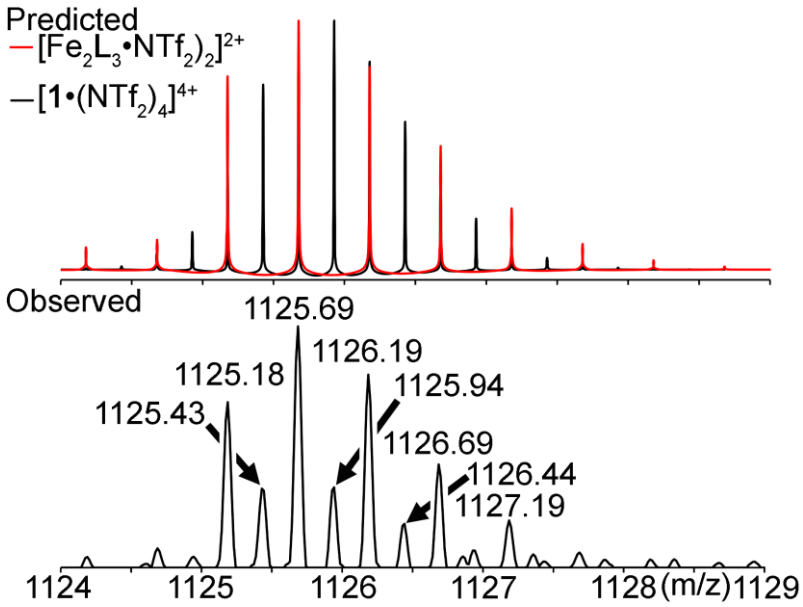

Figure S-59. Stacked comparison of predicted ions $[\mathbf{1}\bullet(NTf_2)_4]^{4+}$ and $[\mathbf{Fe_2L_3}\bullet(NTf_2)_2]^{2+}$ versus experimentally observed peaks.

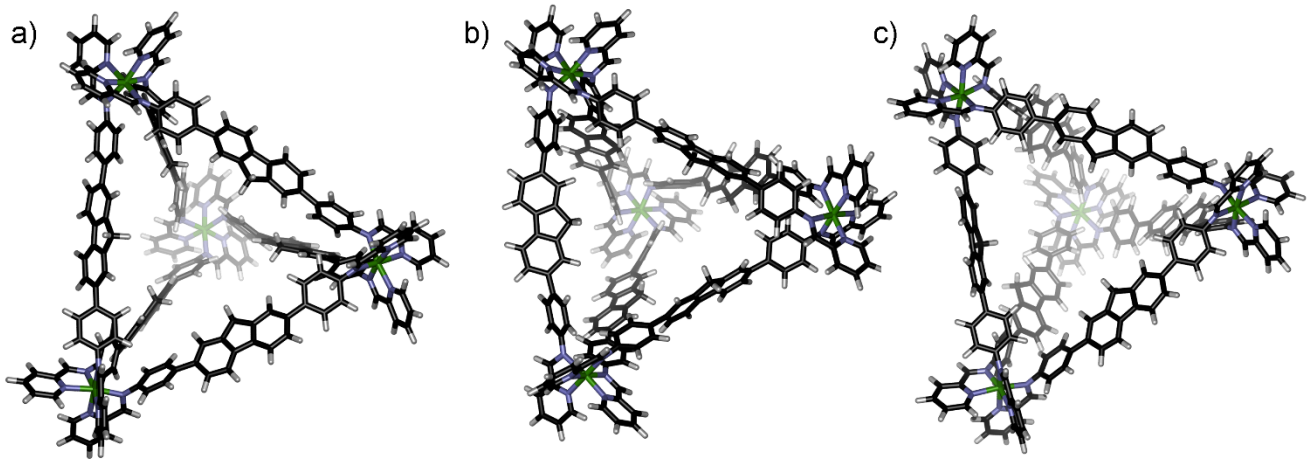

Figure S-60. Energy minimized molecular models of cage **1** isomers. a) T; b) S_4; c) C_3 (SPARTAN, AM1 forcefield).[6]

VI. References

1. a) L. R. Holloway, P. M. Bogie, Y. Lyon, C. Ngai, T. F. Miller, R. R. Julian, and R. J. Hooley, *J. Am. Chem. Soc.* 2018, **140**, 8078. b) W. Meng, J. K. Clegg, J. D. Thoburn, J. R. Nitschke, *J. Am. Chem. Soc.* 2011, **133**, 13652. c) L. R. Holloway, H. H. McGarraugh, M. C. Young, W. Sontising, G. J. O. Beran, R. J. Hooley, *Chem. Sci.* 2016, **7**, 4423.
2. D.B. Hibbert, P. Thordarson, *Chem. Commun.* 2016, **52**, 12792. b) P. Thordarson, *Chem. Soc. Rev.* 2011, **40**, 1305.
3. Mathematica. 11.2, Wolfram Research, Inc., Champaign, Illinois 2017.
4. W.H Press, S.A. Teukolsky, W.T. Vetterling, B.P. Flannery, *Numerical Recipes in C*, Cambridge University Press, Cambridge, 1992
5. C. W. Garland, J. W. Nibler, D. P. Shoemaker, *Experiments in Physical Chemistry*, McGraw-Hill Higher Education: Boston, MA, 2009.
6. M. J. S. Dewar, E. G. Zoebisch, E. F. Healy, J. J. P. Stewart, *J. Am. Chem. Soc.*, 1987, **107**, 3902; calculations performed on SPARTAN 06, Wavefunction Inc.